

Development of CO₂-Stable Oxygen-Transporting Membranes for Oxyfuel Carbon Capture Process

von der Naturwissenschaftlichen Fakultät der
Gottfried Wilhelm Leibniz Universität Hannover
zur Erlangung des Grades
Doktor der Naturwissenschaften
Dr. rer. nat.

genehmigte Dissertation

von
M.Sc. Kaveh Partovi Amarloei

geboren am 02.11.1981 in Teheran, Iran

2015

Referent: Prof. Dr. Jürgen Caro

Korreferent: Prof. Dr. Claus H. Rücher

Tag der Promotion: 10.07.2015

Preface

The following thesis presents an overview of the results I collected during three years of research as a member of the scientific staff at the Institute of Physical Chemistry and Electrochemistry at Gottfried Wilhelm Leibniz Universität Hannover under the supervision of Prof. Dr. Jürgen Caro. The financial support was granted by the Deutsche Forschungsgemeinschaft (Ca 147/18-1) and the Sino-German Centre for Research Promotion (Nos. GZ676 and GZ 911) under the guidance of Prof. Dr. J. Caro and Prof. Dr. Armin Feldhoff.

The present thesis comprises five selected research articles, in four of which I contributed as the primary author, as well as the corresponding author and co-authored one article. Contributions and valuable comments from the co-authors and reviewers for all these articles are gratefully acknowledged. I would like to thank Prof. Dr. Jürgen Caro, Dr. Fangyi Liang, Prof. Dr. Claus Rüscher, and Prof. Dr. Feldhoff for the fruitful discussions and helpful comments.

Chapter 2 investigates the effect of thermal cycling under air/CO₂ gradient on the microstructure of PSCF membrane. The article “*High-Flux Oxygen-Transporting Membrane Pr_{0.6}Sr_{0.4}Co_{0.5}Fe_{0.5}O_{3-δ}: CO₂ Stability and Microstructure*” was written by me. The material preparations and the main part of permeation measurements were completed by me. Dr. Fangyi Liang contributed to the permeation measurements and the SEM and EDXS investigations. The in-situ XRD measurements and characterization were conducted by Dipl.-Chem. Olga Ravkina. Contributions of Prof. Dr. Jürgen Caro and Dr. Fangyi Liang during preparation and revision of the manuscript is acknowledged.

Chapter 3 describes the effect of the B-site composition on the physical and chemical properties of PSCF membranes. The article presented in this chapter entitled “*Effect of the B-Site Composition on the Oxygen Permeability and the CO₂ Stability of Pr_{0.6}Sr_{0.4}Co_xFe_{1-x}O_{3-δ} (0.0 ≤ x ≤ 1.0) Membranes*” was prepared by me. I sincerely acknowledge the valuable suggestions of Prof. Dr. Caro and his support that greatly improved the manuscript. The material preparation and permeation measurements were conducted by me. Dr. F. Liang assisted with some oxygen permeation measurements. Prof. Dr. A. Feldhoff is acknowledged for the valuable comments.

Prof. Dr. C. Rüscher conducted the TGA/DTA measurements and helped with the evaluation of the data. M.Sc. B. Geppert conducted the DC-conductivity experiments. Contributions of Dipl.-Chem. O. Ravkina, M.Sc. A. Schulz, and B.Sc. A. Duong to the *in-situ* XRD measurements and data evaluation are acknowledged.

Chapter 4 introduces a dual-phase PSCF-CP membrane with high oxygen permeability. The article that appears in this chapter entitled “*A Novel CO₂-Stable Dual Phase Membrane with High Oxygen Permeability*” was written by Dr. F. Liang. I contributed to writing of the Experimental Section that appears as the Supporting Information. The material synthesis and membrane preparation was conducted by me. The permeation measurements were completed by Dr. F. Liang and me.

Two articles are presented in Chapter 5. The first article “*Novel CO₂-Tolerant Al-Containing Membranes for High-Temperature Oxygen Separation*” was written by me with valuable contributions by Prof. Dr. J. Caro. M.Sc. M. Bittner conducted the DC-conductivity measurements. Frank Steinbach helped with the SEM, BSEM, and EDXS analysis.

The second article in this chapter entitled “*Enhanced Oxygen Permeability of Novel Cu-Containing CO₂-Tolerant Dual-Phase Membranes*” was written by me with Prof. Dr. J. Caro’s contribution to improvement of the manuscript. Prof. Dr. Rüscher conducted the TGA/DTA measurements. F. Steinbach is acknowledged for his contribution to the preparation of BSEM images.

Acknowledgment

This thesis was completed with help, support and dedication of many people to whom I am greatly indebted.

First and foremost, I would like to express my grateful appreciation to my supervisor Prof. Dr. Jürgen Caro for his support, advice, guidance, valuable comments and giving me the opportunity to work and research in his group. I also thank him for his excellent mentoring and for providing a free and open research atmosphere. I was greatly benefitted by his many years of experience in scientific research. His valuable contribution to preparation of the manuscripts is appreciated.

Furthermore, I would like to thank Prof. Dr. Claus Rüscher for his valuable contribution to this work and for accepting to conduct the second expertise.

Prof. Dr. Armin Feldhoff is thanked for his helpful suggestions and for the fruitful discussions. Dr. Fangyi Liang is gratefully acknowledged for his special engagement and contribution to this work. Dr. Yanying Wei, Dr. Huixia Luo, Dr. Zhengwen Cao, Jian Xue, and Fang Wei are thanked for sharing their knowledge and valuable discussions. Olga Ravkina and Alexander Schulz are appreciated for their help with the XRD measurements. Benjamin Geppert and Michael Bittner are thanked for conducting the DC-conductivity measurements.

Furthermore, I would like to express my appreciation to all the former and the current members of the Institute of Physical Chemistry and Electrochemistry I had the pleasure to work with, especially Dr. Alexander Kuhn, Dr. Nanyi Wang, Lisa Diestel, Alexander Mundstock, Sebastian Friebe, Dr. Andre Düvel, Dr. Tobias Klande, Dr. Olga Wittich, Dr. Oliver Merka, Dr. Yi Liu.

I would like to thank Yvonne Gabbey-Uebe and Kerstin Janze for their great administrative support. Frank Steinbach is sincerely acknowledged for the technical support. I also would like to express my gratitude to Wilfried Becker, Markus Köhler, Peter Mühr, Wolfgang Rogge, and Jan Kuckuck from the mechanical and electrical workshops.

Very special thanks to my family and friends. To my mother, Fereshteh, for being such a great friend throughout my life and for her endless support. To my Father, Kambuzia, for his kind support. To my brother, Kasra, for the great times. Very special thanks to my dear Shaghayegh for her patience, understanding, caring and love. And thanks to all my great friends for everything.

Abstract

Human-induced global climate change is one of the most critical challenges of this century. CO₂ emissions from human activities are accounted for one of the main contributors to the atmospheric greenhouse gas concentrations. A large part of CO₂ emissions originates from the energy production sector and fossil fuel-combusting power plants in particular. According to the global energy reports, despite rapid development of renewable and sustainable clean energy sources, power generation will remain dependent on carbon-intensive fossil fuels due to increasing energy demand in the upcoming decades. Carbon Capture and Storage (CCS) technology have gained considerable attention as a viable industrial means to reduce atmospheric CO₂, targeting the main point sources of CO₂ emissions. The oxyfuel concept, based on fuel combustion in a nitrogen-free O₂/CO₂-containing atmosphere, is considered a promising process for CCS. However, the energy-intensive air separation unit required for oxyfuel process is a major drawback for application of this technology. Replacing the conventional air separation unit with oxygen-transporting membranes is a possible alternative to compensate the energy penalty. This thesis presents five original research articles focusing on the development of CO₂-stable oxygen-transporting membranes for applications as air separation modules in power plants with oxyfuel carbon capture. In this regard, CO₂ stability and oxygen permeation properties of single-phase perovskite membranes, as well as dual-phase composite membranes have been thoroughly investigated.

In Chapter 2 the effect of thermal cycling under CO₂ atmosphere on the microstructure and oxygen permeation performance of a high-flux Pr_{0.6}Sr_{0.4}Co_{0.5}Fe_{0.5}O_{3-δ} perovskite-type membrane is investigated. The CO₂ stability and the phase transitions of the material were investigated using *in-situ* X-ray diffraction (XRD) and long-term oxygen permeation measurements. The effect of CO₂ exposure on the membrane's microstructure was studied by scanning electron microscopy (SEM) and XRD.

The effect of Co/Fe ratios at the *B*-site of the perovskite Pr_{0.6}Sr_{0.4}Co_{*x*}Fe_{1-*x*}O_{3-δ}, on its physical and chemical properties is thoroughly investigated in Chapter 3. Increasing the Co content results in higher electrical conductivity and oxygen permeability,

which could also be confirmed by thermoanalysis. However, CO₂ stability of the membrane decreases with increasing Co content, due to higher surface basicity. Structural properties were characterized using Rietveld Refinement methods. The selected membrane with 20% Co also showed good stability under reducing conditions, when applied as a membrane reactor for partial oxidation of methane to syngas.

In Chapter 4, oxygen permeation performance and CO₂ tolerance of a Co-containing dual-phase membrane with the composition Pr_{0.6}Sr_{0.4}Co_{0.5}Fe_{0.5}O_{3-δ}-Ce_{0.9}Pr_{0.1}O_{2-δ} are studied. This material is based on the perovskite oxide developed in Chapter 3. The phase structure and surface morphology of the membrane were investigated by *in-situ* XRD, SEM, and energy-dispersive X-ray spectroscopy (EDXS). The membrane showed very good oxygen permeation fluxes and high CO₂ stability above 800 °C.

In Chapter 5, newly developed Co-free dual-phase compositions with different doping strategies are studied. In the composition Nd_{1-x}Sr_xAl_{0.2}Fe_{0.8}O_{3-δ}-Ce_{1-y}Nd_yO_{2-δ}, partial substitution of Fe for Al resulted in enhanced oxygen permeation performance at the cost of lower electrical conductivity. XRD results also revealed a phase transformation from orthorhombic symmetry to cubic perovskite by Al-doping. The membrane demonstrated very good CO₂ stability in long-term oxygen permeation measurements. Furthermore, Cu-containing dual-phase membranes with the composition Sm_{1-x}Sr_xCu_{0.2}Fe_{0.8}O_{3-δ}-Ce_{0.8}Sm_{0.2}O_{2-δ} were developed, which showed better oxygen permeation qualities compared to Al-doped composites. XRD, SEM, back-scattered SEM (BSEM) and EDXS investigations revealed a segregated CuO phase, for low Sr content. The CuO phase was formed due to the unit cell volume of the perovskite being too small to accommodate a part of Cu cations. Increasing the Sr content resulted in elimination of the additional phase. The membranes showed stable oxygen permeation fluxes for more than 200 h under CO₂ sweeping.

Keywords: mixed ionic-electronic conductors, oxygen-transporting membranes, CO₂ stability, perovskites, dual-phase membranes

Zusammenfassung

Der anthropogene Klimawandel zählt zu den größten Herausforderungen dieses Jahrhunderts. Der CO₂-Ausstoß durch menschliche Aktivitäten wird als eine der Hauptursachen der hohen atmosphärischen Treibhausgaskonzentrationen angesehen. Ein großer Teil des CO₂-Ausstoßes stammt aus der Energiebereitstellung auf Basis der fossilen Energieträger Kohle, Öl oder Gas. Es wird eingeschätzt, dass - trotz der gewaltigen Fortschritte bei der Entwicklung nachhaltiger sauberer regenerativer Energiequellen - die Energiebereitstellung aufgrund steigenden Energiebedarfs in den nächsten Jahrzehnten weiter von fossilen Brennstoffen abhängig bleiben wird. Die CO₂-Abscheidung und Speicherung (Carbon Capture & Storage) fossil befeuerter Kraftwerke als CO₂-Hauptemissionsquellen hat hohe Aufmerksamkeit als eine industriell realisierbare Technologie für die Reduzierung des atmosphärischen CO₂ gewonnen. Das Oxyfuel-Konzept, basierend auf der Verbrennung der Brennstoffe in einer nahezu Stickstoff-freien Sauerstoff-/Kohlendioxid-Atmosphäre, wird als ein attraktives Verfahren für CCS angesehen. Die energieintensive Sauerstoffproduktionseinheit nach dem Linde-Prinzip ist jedoch ein großer Nachteil für die Anwendung des Oxyfuel-Verfahrens. Das Ersetzen der herkömmlichen Lufttrenneinheit durch einen Permeator mit Sauerstofftransportmembranen ist eine mögliche Alternative, den Energieeinsatz der Sauerstoffproduktion gering zu halten.

Diese Doktorarbeit stellt fünf originale Forschungsartikel vor mit dem Schwerpunkt der Entwicklung CO₂-stabiler Sauerstofftransportmembranen für eine Anwendung als Sauerstofftrenneinheit in Kraftwerken nach dem Oxyfuel-Verfahren. Daher wurden intensiv die CO₂-Stabilität und die Sauerstofftransporteigenschaften von Perowskitmembranen als auch zweiphasigen Kompositmembranen untersucht.

In Kapitel 2 wurde der Effekt von thermischen Zyklen unter CO₂-Atmosphäre auf die Mikrostruktur und den Sauerstofffluss einer Perowskitmembran mit der Zusammensetzung Pr_{0,6}Sr_{0,4}Co_{0,5}Fe_{0,5}O_{3-δ} untersucht. Die CO₂-Stabilität und die Phasenumwandlungen wurden mittels *in-situ* Röntgenbeugung (XRD) und Langzeitpermeationsmessungen untersucht. Der Einfluss von CO₂ auf die Mikrostruktur der Membran wurde mittels Rasterelektronenmikroskopie (REM) und XRD untersucht.

Der Effekt von unterschiedlichen Co/Fe-Verhältnissen am *B*-Gitterplatz auf die physikalischen und chemischen Eigenschaften des Perowskites $\text{Pr}_{0.6}\text{Sr}_{0.4}\text{Co}_x\text{Fe}_{1-x}\text{O}_{3-\delta}$ wurde in Kapitel 3 untersucht. Eine Erhöhung des Co-Anteils ergab eine höhere elektrische Leitfähigkeit und erhöhte Sauerstoffflüsse. Diese Ergebnisse wurden auch durch die Thermoanalyse bestätigt. Die CO_2 -Stabilität der Membran nimmt hingegen mit zunehmendem Co-Anteil aufgrund erhöhter Basizität an der Oberfläche ab. Die strukturellen Eigenschaften wurden mittels der Rietveld-Verfeinerungsmethode charakterisiert. Die ausgewählte Membran mit 20% Co wurde als Membranreaktor für die katalytische partielle Oxidation von Methan zum Syngas eingesetzt und zeigte gute Stabilität unter reduzierender Atmosphäre.

In Kapitel 4 wurden der Sauerstofffluss und die CO_2 -Toleranz einer Co-haltigen zweiphasigen Membran mit der Zusammensetzung $\text{Pr}_{0.6}\text{Sr}_{0.4}\text{Co}_{0.5}\text{Fe}_{0.5}\text{O}_{3-\delta}$ - $\text{Ce}_{0.9}\text{Pr}_{0.1}\text{O}_{2-\delta}$, basierend auf dem in Kapitel 3 entwickelten Perowskit, untersucht. Die Phasenstruktur und Oberflächenmorphologie der Membran wurden mittels *in-situ* XRD, REM, und energiedispersiver Röntgenspektroskopie (EDXS) untersucht. Die Membran besitzt sehr gute Sauerstoffflüsse und hohe CO_2 -Stabilität über 800 °C.

In Kapitel 5 wurden neu entwickelte Co-freie zweiphasige Verbindungen mit unterschiedlichen Dotierungskonzepten untersucht. Bei der Verbindung $\text{Nd}_{1-x}\text{Sr}_x\text{Al}_{0.2}\text{Fe}_{0.8}\text{O}_{3-\delta}$ - $\text{Ce}_{1-y}\text{Nd}_y\text{O}_{2-\delta}$ trug die Al-Dotierung zu verbesserten Sauerstoff-Transporteigenschaften auf Kosten einer geringeren elektrischen Leitfähigkeit bei. Des Weiteren deuteten die XRD-Ergebnisse auf eine Strukturänderung von der orthorhombischen Symmetrie zur kubischen Struktur durch Al-Dotierung hin. Die Membran zeigte sehr gute CO_2 -Stabilität bei den Langzeitpermeationsmessungen. Des Weiteren wurden Cu-haltige zweiphasige Membranen mit der Zusammensetzung $\text{Sm}_{1-x}\text{Sr}_x\text{Cu}_{0.2}\text{Fe}_{0.8}\text{O}_{3-\delta}$ - $\text{Ce}_{0.8}\text{Sm}_{0.2}\text{O}_{2-\delta}$ entwickelt, die deutlich bessere Transporteigenschaften im Vergleich mit den Al-haltigen Verbindungen zeigten. XRD, REM, und EDXS-Charakterisierungen deuteten auf die Entstehung einer segregierten Kupferoxidphase bei einem geringeren Sr-Anteil aufgrund des kleinen Gittervolumens des Perowskites hin. Durch Erhöhung des Sr-Gehaltes konnte die Entstehung der CuO-Nebenphase vermieden werden. Die Membran zeigte stabile Sauerstoffflüsse über 200 h unter reiner CO_2 -Spülung.

Stichwörter: gemischte Leiter, sauerstofftransportierende Membrane, CO_2 -Stabilität, Perowskite, zweiphasige Membrane

Contents

| | |
|---|------|
| Preface | i |
| Acknowledgment | iii |
| Abstract | iv |
| Zusammenfassung | vi |
| Contents | viii |
| Chapter 1 | 1 |
| Introduction | 1 |
| 1.1. Carbon Capture and Storage (CCS) | 1 |
| 1.1.1. Post-Combustion CO ₂ Capture | 1 |
| 1.1.2. Pre-Combustion CO ₂ Capture | 2 |
| 1.1.3. Oxyfuel CO ₂ Capture | 3 |
| 1.1.4. Integration of OTMs in Oxyfuel Power Plants | 4 |
| 1.2. MIECs for Oxygen Separation | 5 |
| 1.2.1. Structural Properties of MIECs | 6 |
| 1.2.2. Oxygen Transport through MIECs | 8 |
| 1.3. MIECs for Oxyfuel Carbon Capture | 12 |
| 1.3.1. Perovskite-Type Oxides | 12 |
| 1.3.2. Dual-Phase Compositions | 17 |
| 1.4. Oxygen-Transporting Membranes (OTMs) | 19 |
| 1.4.1. Preparation of OTMs | 19 |
| 1.4.2. Oxygen Permeation Measurements | 20 |
| 1.5. Bibliography | 22 |
| Chapter 2 | 32 |
| Effect of Thermocycling on the Microstructure and Permeation Properties of a Single-Phase Perovskite Membrane | 32 |
| 2.1. Summary | 32 |
| 2.2. High-Flux Oxygen-Transporting Membrane Pr _{0.6} Sr _{0.4} Co _{0.5} Fe _{0.5} O _{3-δ} : CO ₂ Stability and Microstructure | 33 |
| Chapter 3 | 43 |
| Effect of the <i>B</i> -Site Co/Fe Ratio on the Permeation Properties and CO ₂ Susceptibility of PSCF Membrane | 43 |
| 3.1. Summary | 43 |
| 3.2. Effect of the <i>B</i> -Site Composition on the Oxygen Permeability and the CO ₂ Stability of Pr _{0.6} Sr _{0.4} Co _{<i>x</i>} Fe _{1-<i>x</i>} O _{3-δ} (0.0 ≤ <i>x</i> ≤ 1.0) Membranes | 44 |
| Chapter 4 | 54 |

| | |
|---|-----|
| Cobalt-Containing Dual-Phase Membranes..... | 54 |
| 4.1. Summary | 54 |
| 4.2. A Novel CO ₂ -Stable Dual Phase Membrane with High Oxygen Permeability | 55 |
| Supporting Information for | 60 |
| A Novel CO ₂ -Stable Dual Phase Membrane with High Oxygen Permeability | 60 |
| Chapter 5..... | 71 |
| High-Flux Co-Free Dual-Phase Membranes for Oxyfuel Concept | 71 |
| 5.1. Summary | 71 |
| 5.2. Novel CO ₂ -Tolerant Al-Containing Membranes for High-Temperature Oxygen Separation | 73 |
| 5.3. Enhanced Oxygen Permeability of Novel Cu-Containing CO ₂ -Tolerant Dual-Phase Membranes..... | 82 |
| Appendix..... | 102 |
| Publications Included in the Thesis | 102 |
| Publication Not Included in the Thesis..... | 102 |
| Curriculum Vitae..... | 103 |
| Erklärung zu dieser Dissertation..... | 104 |

Chapter 1

Introduction

1.1. Carbon Capture and Storage (CCS)

The anthropogenic CO₂ emissions, largely caused by the combustion of fossil fuels, are known to be the main contributor to the global climate change. Moreover, the current projections for the international energy consumption and production predict an increasing demand for energy with a continuously growing trend of fossil fuel-based power generation in the upcoming decades.^[1,2] Alone in 2012, electricity and heat production with 13.3 Gt of CO₂ emission accounted for 42% of the global CO₂ emissions of 31.7 Gt, which shows an increase of 1.8% compared to the previous year.^[3] Therefore, immediate reduction of atmospheric greenhouse gases particularly CO₂ is of crucial importance in order to mitigate the climate change and to prevent its disastrous aftermaths. While alternative zero-emission energy sources, such as solar energy, wind power, and hydropower are under development, parallel technologies are essential to cut the CO₂ emissions from the existing carbon-intensive energy system. Carbon capture and storage (abbreviated as CCS) is a promising technology for CO₂ disposal, targeting fossil fuel-burning power plants as the main point sources of CO₂ emissions. The captured CO₂ is subsequently compressed, transported and stored in geological repositories, such as depleted gas and oil reservoirs.^[4,5] Three main process routes for CCS are currently under investigation: Post-combustion, pre-combustion, and oxyfuel combustion, which are briefly introduced in the following chapters.

1.1.1. Post-Combustion CO₂ Capture

The post-combustion capture route is based on CO₂ separation from the flue gas after the combustion process,^[6] as schematically depicted in Figure 1.1. In the post-combustion concept, CO₂ is chemically absorbed using mainly amine-based solvents

and thermally removed from the solvent in a regeneration stage using recovery columns. Presently, monoethanolamine (abbreviated as MEA) is widely used for the chemical washing process of CO₂, which poses additional challenges in terms of stability and efficiency.^[7,8] SO₂ and NO_x present in the flue gas can react with the amine-based solvents and result in degradation of the solvent. In order to prevent this, the concentration of the reactive gases is required to be kept at a low level, *e.g.* below 10 ppm for SO₂.^[9] Accordingly, preventing measures such as gas-cleaning stages and extra solvent regeneration processes are essential prior to the recirculation of the solvent into the system. In addition, large-scale equipment and considerable volumes of solvents are needed, especially due to the dilution of CO₂ with N₂ from the combustion gas mixture. Although the post-combustion concept has the distinct advantage of being adoptable to the presently available power plants without substantial modification of their existing power cycles, its cost and energy-efficiency still need to be improved. High energy demands for the solvent regeneration and the environmental impact associated with the solvent disposal and regeneration byproducts are considered to be the main disadvantages of the post-combustion capture.^[5,8,10]

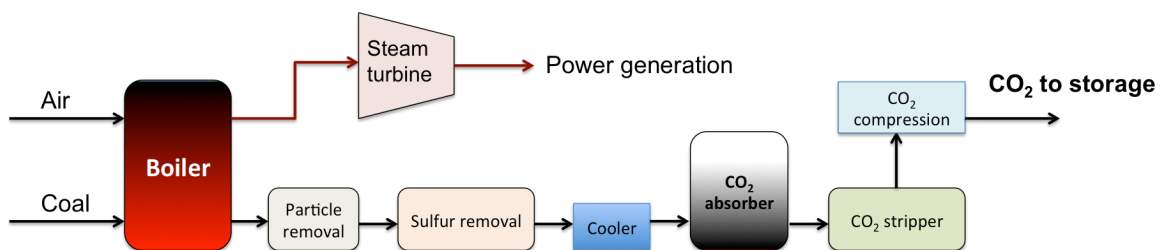


Figure 1.1. Schematic diagram of a power plant with post-combustion carbon capture.

1.1.2. Pre-Combustion CO₂ Capture

In a pre-combustion route, the fuel gas is chemically decarbonized prior to the combustion stage. Therefore pre-combustion route is commonly applied to coal-fired power plants with Integrated Gasification Combined Cycle (IGCC) technology, as shown in Figure 1.2. In a gasification stage, the primary fuel is partially oxidized to produce syngas (CO + H₂). Subsequently, steam is supplied to the gas mixture in

order to oxidize CO to CO₂ in a catalytic water-gas shift process, as described in Equation 1.1:



CO₂ is then removed from the mixture using solvent-based methods and pressure swing adsorption, to obtain a hydrogen-rich fuel.^[8] The advantages of the pre-combustion capture include high efficiency and product flexibility, *e.g.* syngas can be converted to value-added products such as methanol and hydrogen can be used as fuel for zero-emission power or heat generation. However, disadvantages include high construction and maintenance costs and low reliability due to increased complexity of IGCC systems with carbon capture.^[5,8]

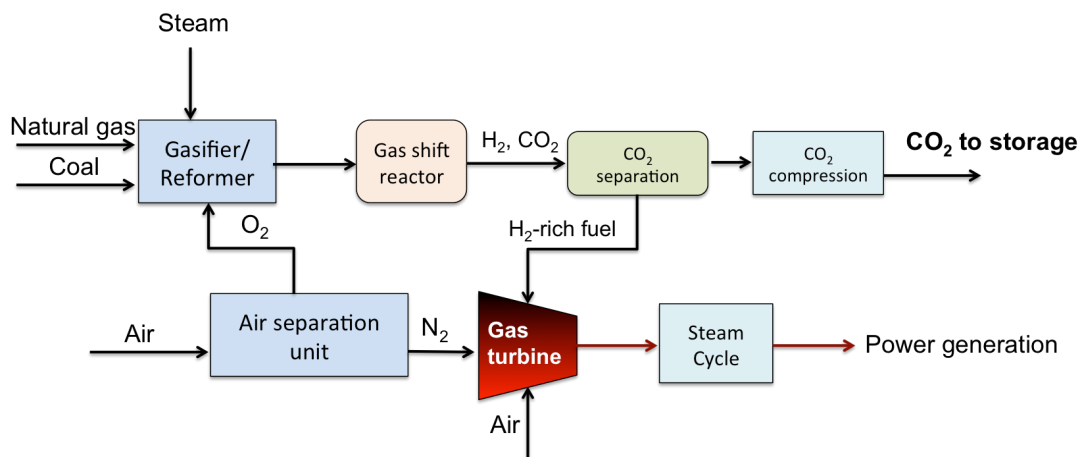


Figure 1.2. Schematic diagram of a power plant with pre-combustion carbon capture.

1.1.3. Oxyfuel CO₂ Capture

The oxyfuel concept is based on the denitrification of the combustion gas by utilization of high-purity oxygen (>95% purity) instead of air for the fuel combustion, resulting in a flue gas mainly consisting of CO₂ and steam. Since fuel combustion in pure oxygen results in excessively high temperatures, a stream of CO₂ from the flue gas is redirected to the boiler, in order to limit the flame temperature by dilution of the combustion gas mixture,^[8,11] as schematically depicted in Figure 1.3. The removal of nitrogen from the combustion gas mixture not only remarkably reduces the total volume of the flue gas for CO₂ capture by about 80%, it also yields high

concentrations of CO₂ and water steam in the flue gas, thus facilitating the separation process performed by condensing heat exchangers. A further advantage of the oxyfuel combustion route is its significantly lower NO_x emissions.^[12,13] There are several technical issues to be tackled in the oxyfuel concept, including recirculation of a large volume fraction of the flue gas (about 60%) back into the combustion chamber and elimination of impurities such as NO_x and SO_x originating from the fuel or from leakage in the power cycle components. However, the conventional cryogenic air separation unit (ASU) for high purity oxygen production requires a considerable energy input and is accounted for a major efficiency loss in oxyfuel power plants. Substitution of the cryogenic distillation for less energy-intensive alternatives, such as oxygen-transporting membranes (OTMs), is considered to be a promising approach to reduce the energy penalty caused by the conventional ASU.^[8,12,14] The following section discusses some technological and scientific aspects of the application of OTM technologies in oxyfuel power plants.

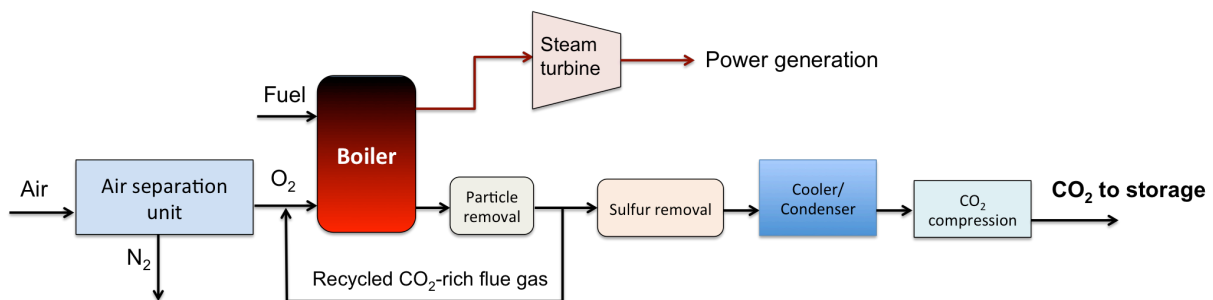


Figure 1.3. Schematic diagram of a power plant with oxyfuel carbon capture.

1.1.4. Integration of OTMs in Oxyfuel Power Plants

Utilization of oxygen-transporting membranes (OTMs) based on mixed ionic-electronic conducting oxides (MIECs) with typical operating temperatures between 800 and 1000 °C for oxygen separation in oxyfuel processes is expected to reduce the energy penalty from the cryogenic ASU. Dense ceramic OTMs can be integrated in oxyfuel power plants using a three-end or a four-end concept.

In the three-end operation mode, three gas streams are involved in the separation unit. Preheated air is used as the feed gas, while vacuum is applied on the permeate

side and the oxygen-depleted stream of air is retained from the membrane module. Another method of achieving high oxygen partial pressure gradient across the membrane module is application of high-pressure feed. Since the membrane is not exposed to CO_2 , the thermochemical stability against CO_2 is not the main concern. However, phase stability and decomposition behavior of the conventional perovskite-type $(\text{Ba,Sr})(\text{Co,Fe})\text{O}_3$ membranes, as well as the energy penalty from the vacuum pump are considered to be the main challenges for the energy-efficient three-end operation mode.^[15,16]

In the four-end operation concept, a stream of CO_2 redirected from the flue gas, is applied as the sweep gas for oxygen transport to the combustion chamber, while increasing the oxygen partial pressure gradient across the membrane.^[17, 18] Furthermore, since the membrane module is located within the recirculation system, the high-temperature requirement for the operation of MIEC membrane is efficiently provided, thus reducing the overall energy demand for the oxygen production. However, since the four-end membrane module is directly exposed to the flue gas, high thermochemical resistivity against corrosive gas components such as CO_2 and SO_x , while maintaining high fluxes of permeated oxygen is the major prerequisite for the proper MIEC material selection.

As will be discussed in the following chapters, the most promising MIECs in terms of oxygen permeation performance contain alkaline-earth elements, mainly Ba and Sr, which strongly compromises the CO_2 -stability of the membrane material. The degradation of the membrane permeation performance occurs due to the formation of an oxygen-impermeable alkaline-earth carbonate layer on the surface layer of the membrane under atmospheres containing high concentrations of CO_2 .^[19,20] The development of high-flux OTMs with suitable CO_2 -stability is the main focus of the present thesis.

1.2. MIECs for Oxygen Separation

During the past few decades, mixed ionic-electronic conducting oxides (MIECs) have been the subject of numerous studies for the development of energy-efficient technological devices for oxygen transport and separation at elevated temperatures.^[21,22] Accordingly, MIEC-based dense ceramic membranes can find application in a wide variety of technological fields, including utilization as

membrane reactors for chemical processes such as partial oxidation of methane (POM) to syngas ($\text{CO} + 2\text{H}_2$),^[23-25] oxidative coupling of methane (OCM) to ethylene and ethane,^[26-28] and oxyfuel combustion.^[16,29] Furthermore, MIECs have been investigated for other electrochemical applications such as electrode material for solid oxide fuel cells (SOFC).^[30,31] One of the most important aspects of MIEC-based OTMs is their 100% oxygen perm-selectivity, owing to the electrochemical nature of the oxygen transport mechanism in these materials, as will be discussed in detail in the following sections.

1.2.1. Structural Properties of MIECs

A number of ceramic compounds exhibit ionic oxygen conduction, including perovskite-type, fluorite-type, and K_2NiF_4 -type layered oxides.^[32-34] Among MIECs, perovskite-type oxides with the general formula ABO_3 are the most promising materials in terms of mixed conducting properties.^[21,35] Although the term perovskite originally refers to the mineral CaTiO_3 , named after the Russian mineralogist Count Lev Aleksevich von Perovski, perovskite-type oxides generally denote a class of oxides, with an ideal cubic crystal structure shown in Figure 1.4. The A -site of the ABO_3 structure is occupied by a large cation, such as alkaline earth and rare-earth elements, and is 12-fold coordinated by oxygen ions, whereas a smaller cation (mostly transition metals) occupies the B -site of the structure, coordinated by six oxygen ions. For better comprehensibility, the oxygen ions in Figure 1.4. are depicted much smaller than their actual proportional size. The BO_6 octahedra in an ideal cubic perovskite share corners to form a three-dimensional network. By definition, in an ideal cubic perovskite structure with closely packed hard spheres, the cations at the A - and B -sites are in touching contact with oxygen anions, resulting in the following relationships:

For the face diagonals,

$$a = \sqrt{2} (r_A + r_O) \quad (\text{Eq. 1.2})$$

For the edges,

$$a = 2 (r_B + r_O) \quad (\text{Eq. 1.3})$$

where r_A , r_B , and r_O designate the ionic radii of the components and a is the edge length or the lattice constant. In early 1920s, the tolerance factor, t , was introduced by Goldschmidt to roughly estimate the formation of perovskite structure by a given assembly of ions and describe the degree of deviation from the ideal cubic symmetry, as described in Equation 1.4:^[36]

$$t = \frac{r_A + r_O}{\sqrt{2} (r_B + r_O)} \quad (\text{Eq. 1.4})$$

Generally, a perovskite-type structure is expected to form in the range of $0.75 \leq t \leq 1.0$. For an ideal cubic perovskite symmetry $Pm\bar{3}m$ (space group: 221), the tolerance factor, t , equals unity. A negative deviation of t from unity ($t < 1$), e.g. in case of an undersized A -site cation, the BO_6 octahedra tilts, due to the reduced A -O bond length, resulting in a distorted symmetry. The extent and the nature of the distortion can largely depend on the A - and B -site cation sizes, as well as on the defect chemistry of the crystal lattice. For instance, a trend of increasing orthorhombic distortion with decreasing A -site cation size was reported for the perovskite-type $LnNiO_3$ series, where Ln represents rare-earth elements La, Pr, Nd, and Sm.^[37] In contrast, for $t > 1$, as is the case for structures with oversized A -site and/or undersized B -site cations, the B -O- B links can be strained to the point that the BO_6 octahedra share faces instead of corners, resulting in variations of AO_3 layer stacking sequences. Consequently, the variation of the stacking sequences leads to formation of cubic or hexagonal perovskite structures, known as polytype phases. However, for small deviations of the Goldschmidt's tolerance factor in the range of $0.9 \leq t \leq 1.05$, stabilization of the cubic perovskite structure is possible.^[38,39] A large number of metallic elements can be stabilized in a perovskite structure. Since perovskites can also accommodate high concentrations of dopant elements, their electronic structure and chemical properties can be tailored into a wide variety of applications. A key condition for the ionic conductivity of a perovskite structure is its defect chemistry. The oxygen non-stoichiometry and the related electronic defect structure, which can be achieved by a proper doping strategy, lead to the mixed ionic-electronic conduction properties of perovskites.^[40] The mechanisms associated with the ionic oxygen transport through MIECs are discussed in the following section.

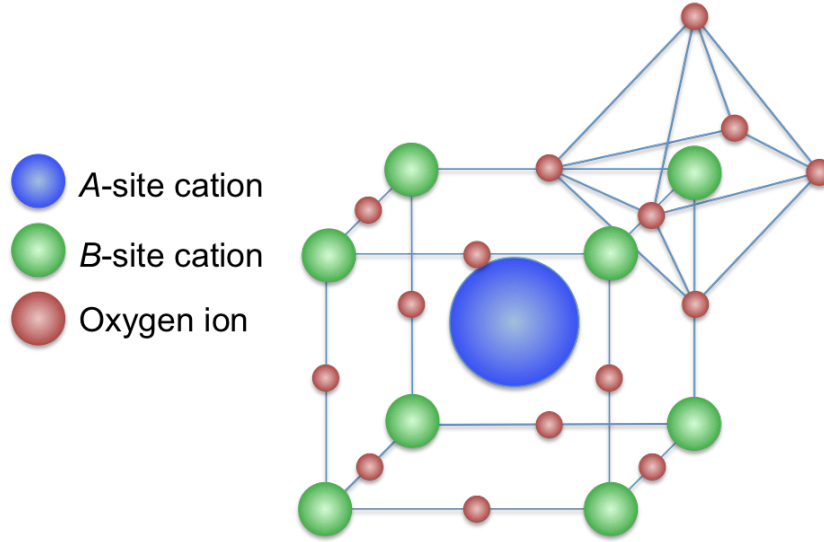


Figure 1.4. Unit cell of a cubic perovskite-type ABO_3 oxide. For simplicity, oxygen ions appear much smaller than their actual proportional size.

1.2.2. Oxygen Transport through MIECs

Generally, ionic defects in MIECs can be in form of vacant lattice sites or vacancies (as in perovskite $(Ba,Sr)(Co,Fe)O_{3-\delta}$ and fluorite-type oxide $Ce_{0.9}Gd_{0.1}O_{2-\delta}$) or in form of interstitial ions (as in K_2NiF_4 -type oxide $La_2NiO_{4+\delta}$).^[41] In a perovskite system, the oxygen vacancies provide a path for ionic diffusion. The amount of defects can be adjusted by introduction of low valence cations to the A -site or the B -site of the lattice. The oxygen transport in a perovskite is basically the result of the oxygen vacancy diffusion, where a chemical potential gradient of the ionic species across the bulk material functions as the driving force for the ionic conduction. The simultaneous movement of the electronic defects (*e.g.* electron holes created by the excitation of electrons from valence to conduction band) preserves the overall electroneutrality. The total conductivity of a MIEC, σ_{tot} , can be expressed by the sum of the ionic conductivity, σ_{ion} , and the electronic conductivity, σ_e :

$$\sigma_{tot} = \sigma_{ion} + \sigma_e \quad (\text{Eq. 1.5})$$

However, the electronic conductivity of a MIEC is much higher than the ionic conductivity and therefore dominates the overall conductivity (*i.e.* $\sigma_{tot} \approx \sigma_e$).^[42] The electrical conductivity of MIECs can be of n-type or p-type nature, depending on a

number of parameters, such as their electronic structure, elemental composition, oxygen partial pressure, temperature, *etc.*^[43] For example, in the acceptor-doped $\text{La}_{1-x}\text{Sr}_x\text{Co}_{0.2}\text{Fe}_{0.8}\text{O}_{3-\delta}$ system, the excess negative charge is compensated by reduction of the *B*-site species and the electronic conduction is mediated by the thermally activated small polaron hopping mechanism *via B-O-B* conduction pairs, which can be described as the following equation:

$$\sigma_e = \frac{C}{T} e^{\frac{-E_a}{kT}} \quad (\text{Eq. 1.6})$$

where T , E_a and k denote absolute temperature, activation energy and the Boltzmann constant, respectively. The pre-exponential constant C is a material characteristic parameter that includes the charge carrier concentration term. At higher temperatures, the electronic conductivity gradually decreases coinciding with the formation of oxygen vacancies at the expense of *p*-type charge carriers.^[44]

The principle mechanisms involved in the oxygen transport in a MIEC (as schematically depicted in Figure 1.5.) can be summarized in three main steps:

- i) On interface I under the higher oxygen partial pressure (feed side): Oxygen surface-exchange reaction, including oxygen dissociation, ionization and sorption into the lattice *via* oxygen vacancies, which can be described in a simplified form using Kröger-Vink notations as follows:^[45]



where h^{\bullet} and $V_{\text{O}}^{\bullet\bullet}$ represent an electron hole and an oxygen vacancy, respectively.

- ii) Bulk diffusion of ionic oxygen and electronic defects in the bulk material, driven by the activity gradients of each species.
- iii) On interface II under the lower oxygen partial pressure (sweep side): The surface-exchange reaction in form of oxygen re-association and desorption, described by the following equation:



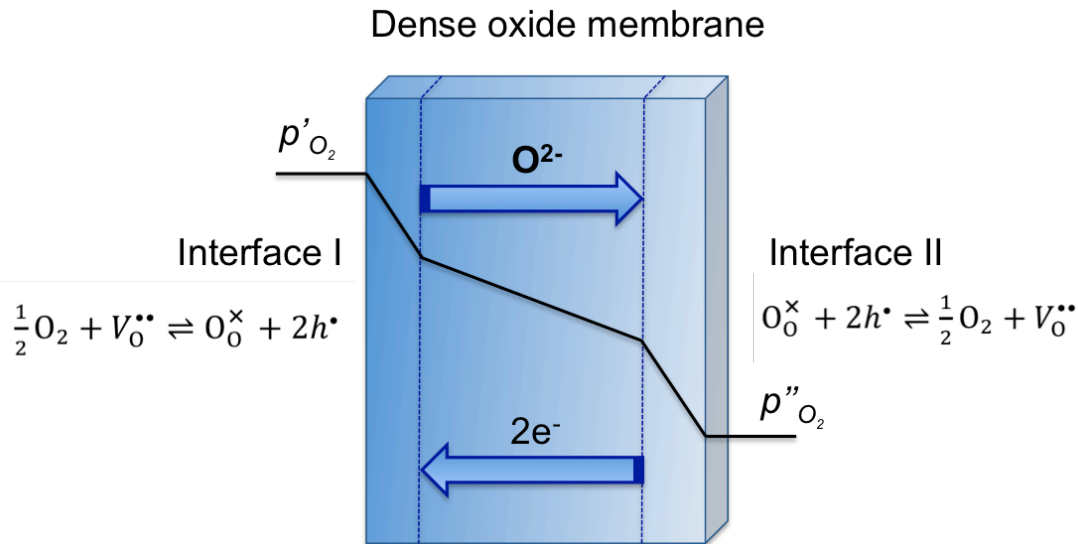


Figure 1.5. Schematic representation of oxygen transport through a dense MIEC membrane under oxygen partial pressure gradient.

The overall rate of oxygen permeation is defined by the rate-limiting step with the slowest reaction rate.^[46,47] Depending on the material properties and the membrane's thickness, surface-exchange reaction or bulk diffusion can determine the overall permeation rate. For a relatively thick membrane, bulk diffusion becomes the rate-limiting step. If the membrane's thickness, L , is reduced below a critical thickness, L_c , the surface exchange reaction on the interfaces of the membrane limits the permeation rate. The critical thickness, L_c , is theoretically attributed to a thickness at which the permeation rate is equally affected by both the diffusion and surface exchange processes and can be defined as the quotient of self-diffusion coefficient of ionic oxygen, D_i , or the tracer diffusion coefficient, D^* , and the surface exchange coefficient, k , as described by the following equation:^[48]

$$L_c = \frac{D_i}{k} = \frac{D^*}{k} \quad (\text{Eq. 1.9})$$

For a sufficiently thick membrane (*i.e.* $L \gg L_c$), the oxygen transport is a diffusion-controlled process and the permeation rate is basically determined by the lattice diffusion of ionic oxygen and counteracting flux of electronic charge carriers. In this case, the oxygen flux can be expressed using the Wagner's theory of ambipolar diffusion,^[49] based on the assumption that the fluxes of the ionic and electronic charge carriers are related by the condition of charge neutrality and no net charge is

transferred across the membrane.^[50] The oxygen flux, j_{O_2} , can be expressed by the following equation:

$$j_{O_2} = -\frac{1}{4^2 F^2} \left(\frac{\sigma_{ion} \cdot \sigma_e}{\sigma_{tot}} \right) \nabla \mu_{O_2} \quad (\text{Eq. 1.10})$$

where F , represents the Faraday's constant. $\nabla \mu_{O_2}$ is the chemical potential gradient, which can be correlated to the oxygen partial pressure, p_{O_2} , by the following equation:

$$\nabla \mu_{O_2} = \frac{\partial RT \ln p_{O_2}}{\partial x} \quad (\text{Eq. 1.11})$$

where R and T are the gas constant and the absolute temperature, respectively, x represents the distance. By the assumption of an oxygen partial pressure gradient of (p'_{O_2}/p''_{O_2}) applied across a membrane with the thickness L , Equation 1.12 can be obtained from Equations 1.10 & 1.11:

$$j_{O_2} = \frac{RT}{4^2 F^2 L} \int_{\ln p''_{O_2}}^{\ln p'_{O_2}} \frac{\sigma_{ion} \cdot \sigma_e}{\sigma_{tot}} d \ln p_{O_2} \quad (\text{Eq. 1.12})$$

As previously mentioned, the total conductivity is dominated by the electronic conductivity. Considering the above assumption, Equation 1.12 can be simplified to:

$$j_{O_2} = \frac{RT}{4^2 F^2 L} \int_{\ln p''_{O_2}}^{\ln p'_{O_2}} \sigma_{ion} d \ln p_{O_2} \quad (\text{Eq. 1.13})$$

The ionic conductivity can be described in relation to the oxygen vacancy concentration, $[V_O^{\bullet\bullet}]$, by the Nernst-Einstein equation:

$$\sigma_{ion} = \frac{4F^2 [V_O^{\bullet\bullet}] D_V}{RT} \quad (\text{Eq. 1.14})$$

where D_V denotes the diffusion coefficient of oxygen vacancies, which can be obtained by ^{18}O - ^{16}O isotope exchange measurements.^[51,52] By assumption of a constant average value for ionic conductivity, $\bar{\sigma}_{ion}$, *e.g.* under low oxygen partial pressure gradients, Equation 1.13 can be integrated to:

$$j_{O_2} = \frac{RT \bar{\sigma}_{ion}}{4^2 F^2 L} \ln \frac{p'_{O_2}}{p''_{O_2}} \quad (\text{Eq. 1.15})$$

However, Wagner's theory is only applicable if bulk diffusion is the rate-limiting step of the permeation process. By reducing the membrane's thickness below the critical thickness (*i.e.* $L \ll L_c$), the surface exchange reaction defines the overall oxygen permeation rate. A number of processes are involved in the surface exchange reaction at the gas/solid interface, including dissociation and re-association of oxygen, charge transfer, adsorption, desorption, *etc.* Accordingly, several models and relations have been proposed depending on the nature of the involved processes. In general, with the assumption of near-equilibrium conditions and exclusion of non-linear effects resulting from high oxygen potential gradients,

$$j_{O_2} = -j_{ex}^0 \frac{\nabla \mu_{O_2}}{RT} \quad (\text{Eq. 1.16})$$

where j_{ex}^0 represents the balanced exchange rate. The kinetic exchange parameter j_{ex}^0 can be determined by ^{18}O - ^{16}O isotopic exchange techniques.^[48]

1.3. MIECs for Oxyfuel Carbon Capture

1.3.1. Perovskite-Type Oxides

High oxygen permeation fluxes through perovskite membranes were first reported by Teraoka *et al.* for perovskite-type oxide series $\text{La}_{1-x}\text{Sr}_x\text{Co}_{1-y}\text{Fe}_y\text{O}_{3-\delta}$ (abbreviated as LSCF), which exhibited oxygen permeation fluxes two to four orders of magnitude higher than that of stabilized zirconia, reaching a maximum value of $3.1 \text{ cm}^3(\text{STP}) \text{ min}^{-1} \text{ cm}^{-2}$ measured on a dense membrane (1 mm thick) with the composition $\text{SrCo}_{0.8}\text{Fe}_{0.2}\text{O}_{3-\delta}$ at $850 \text{ }^\circ\text{C}$.^[32, 53] Since then, perovskite-type OTMs have been extensively studied by many researchers. Among the developed materials, perovskite oxides $\text{Sr}(\text{Co,Fe})\text{O}_{3-\delta}$, $(\text{Ba,Sr})(\text{Co,Fe})\text{O}_{3-\delta}$, and $(\text{La,Sr})(\text{Co,Fe})\text{O}_{3-\delta}$ have gained considerable attention for a wide variety of technological applications.^[35, 54-56] Partial substitution of the *A*- and *B*-site elements by other metal cations can greatly influence a number of material's properties, including the oxygen permeation performance, electrical conductivity and phase stability of the perovskite. Accordingly, different doping strategies have been developed to achieve preferred functionalities. Furthermore, the oxygen permeation performance of a membrane can be enhanced

by means of surface modification. For example, deposition of a porous layer of the same material on the membrane's surface can improve the permeation performance by increasing the surface area. In addition, surface modification or functionalization using other materials such as praseodymium oxide can increase oxygen dissociation rates on the feed side of the membrane, resulting in higher oxygen permeation fluxes.^[57]

Among the above mentioned perovskite systems, $\text{SrCo}_{0.8}\text{Fe}_{0.2}\text{O}_{3-\delta}$ (abbreviated as SCF) and $\text{Ba}_{0.5}\text{Sr}_{0.5}\text{Co}_{0.8}\text{Fe}_{0.2}\text{O}_{3-\delta}$ (abbreviated as BSCF) are the most prominent MIECs in terms of oxygen permeability.^[35,55] However, structural instability of these materials at intermediate temperatures is a major drawback for their technological applications. Oxygen permeability of SCF membranes has been reported to decrease with time, due to a phase transition from cubic perovskite to a vacancy-ordered brownmillerite phase under a low oxygen partial pressure at intermediate temperatures.^[55,58] Some doping strategies have been considered to improve the phase stability of SCF, such as doping 4 at.% Zr at the *B*-site or introduction of La at the *A*-site, which stabilizes the perovskite structure at the cost of lower oxygen permeability.^[59,60]

BSCF was found to decompose into a Ba-rich hexagonal perovskite and a Sr-rich cubic perovskite after long-term dwelling at intermediate temperatures ($T < 900^\circ\text{C}$), resulting in a gradual decrease in oxygen permeation fluxes.^[61,62] According to Yakovlev *et al.* *B*-site doping of BSCF with 3 at.% Zr is effective in stabilization of the cubic perovskite structure down to 800°C , while preserving the oxygen transport properties.^[63]

In one of their early works, Teraoka *et al.* studied the $\text{La}_{0.6}\text{Sr}_{0.4}\text{Co}_{0.8}\text{B}'_{0.2}\text{O}_3$ ($\text{B}' = \text{Mn}, \text{Co}, \text{Fe}, \text{Ni}, \text{Cu}, \text{Cr}$) perovskite-type oxides and reported the following trends of increasing oxygen permeation fluxes for the *B*-site dopant: $\text{Cu} > \text{Ni} > \text{Co} > \text{Fe} > \text{Cr} > \text{Mn}$.^[64] Although partial substitution of Co for Fe has a negative effect on the oxygen permeability of the material, the Fe content at the *B*-site was found to play a crucial role in stabilization of the perovskite structure.^[32,65] Therefore, despite their lower oxygen permeabilities compared to those of SCF and BSCF membranes, the LSCF series have been investigated by many researchers for a variety of applications, due to their superior thermochemical stability. Generally, increasing the Sr and Co contents of these materials improves both their electronic and ionic conductivities. Partial substitution of trivalent La for divalent Sr increases the oxygen

nonstoichiometry of the perovskite lattice and slightly increases the unit cell volume, due to the larger ionic radius of 12-fold coordinated Sr ($r = 144$ pm) compared to that of La ($r = 136$ pm).^[42,44,66,67] In a similar way, increasing oxygen permeability with higher Co content can be correlated to the lower mean valence state of Co in comparison with Fe, and weaker bonding energy of Co-O compared to that of Fe-O.^[42,66,68] However, high concentrations of Co compromises the chemical stability of the membrane in reducing atmospheres. Reduction of Co at intermediate temperatures also results in high thermal expansion coefficients and poor thermomechanical properties of the membrane.^[68] Along with stability issues, other disadvantages associated with Co, such as toxicity, high costs, and increased volatility of Co at elevated-temperatures has led to development of cobalt-free perovskite-type oxides, including $\text{Ba}_{0.5}\text{Sr}_{0.5}\text{Fe}_{0.8}\text{Cu}_{0.2}\text{O}_{3-\delta}$,^[69] $\text{Ba}_{0.5}\text{Sr}_{0.5}\text{Fe}_{0.8}\text{Zn}_{0.2}\text{O}_{3-\delta}$,^[70] $\text{Ba}_{0.5}\text{Sr}_{0.5}\text{Fe}_{0.9}\text{Al}_{0.1}\text{O}_{3-\delta}$,^[71] and $\text{BaFe}_{0.91}\text{La}_{0.04}\text{Zr}_{0.05}\text{O}_{3-\delta}$.^[72]

As mentioned in Section 1.1.4., a key prerequisite for the integration of MIECs in the 4-end oxyfuel configuration is the high stability of these materials in CO_2 -rich environments. However, the majority of perovskite OTMs with reasonable permeabilities developed to date, contain high concentrations of alkaline-earth cations Ba, Sr, and Ca at their *A*-site, which tend to react with gaseous CO_2 to form an oxygen-impermeable carbonate phase on the outer surface layer of the membrane. The formation of alkaline earth carbonates such as BaCO_3 and SrCO_3 results in a dramatic degradation of the membrane's permeation performance.^[21,73] Arnold *et al.* reported an immediate decrease in permeation fluxes to negligible levels on a BSCF membrane when swept with CO_2 at 875 °C. The effect of carbonate formation on the oxygen permeation could be reversed by switching the sweep gas from CO_2 back to helium, as carbonate decomposes to the related alkaline earth oxides and gaseous CO_2 under low partial pressures of CO_2 .^[19] Degradation of SCF membrane during partial oxidation of methane to synthesis gas was described by Pei *et al.* as a result of strontium carbonate formation and the consequence segregation of cobalt and iron oxides.^[74]

Thermodynamic stability of related carbonates depends on the CO_2 partial pressure and temperature. The collective thermodynamic data regarding the formation/decomposition behavior of the carbonates of common metallic components of a perovskite is provided as an Ellingham diagram, shown in Figure 1.6.^[75] The stability of carbonates increases in the order of $\text{Ba}^{2+} > \text{Sr}^{2+} > \text{Ca}^{2+}$, directly

correlating to the associated cation sizes. The polarization power of the divalent alkaline earth cations inversely corresponds to the ionic radius of the cations. Accordingly, with increasing polarization power of the cation, decomposition of the carbonate ion is facilitated; leading to a trend of lower carbonate stabilities with decreasing cation sizes.^[76] However, it should be noted that the Ellingham diagram merely provides an estimation of the carbonate stability, assuming pure oxide phases. For more accuracy in thermodynamic calculations, the stabilization energy of the perovskite structures should also be considered.^[77]

Several approaches have been proposed to increase the CO₂ tolerance of the perovskite membranes, while retaining a reasonable oxygen permeation flux. A complete exclusion of the alkaline earth elements from the *A*-site components results in poor permeation properties of such membranes, making them unsuitable for practical applications. However, partial substitution of the *A*-site Ba and Sr for less reactive elements is considered to be an effective means to improve the resistivity of the membranes in CO₂-rich atmospheres. Rare earth elements, such as La, Pr, Sm, and Gd, with ionic radii comparable to those of alkaline earth elements are regarded as the best alternative cations to partially occupy the *A*-site of the perovskite lattice. Klände *et al.* investigated the effect of partial substitution of *A*-site Sr for La on the CO₂ stability of the SrCo_{0.2}Fe_{0.8}O_{3-δ} system and reported long-term stable oxygen permeation fluxes for the membrane with a Sr content of 40 at.%,^[78] which was in good agreement with previous studies conducted on disk-shaped and hollow fiber membranes.^[73,79]

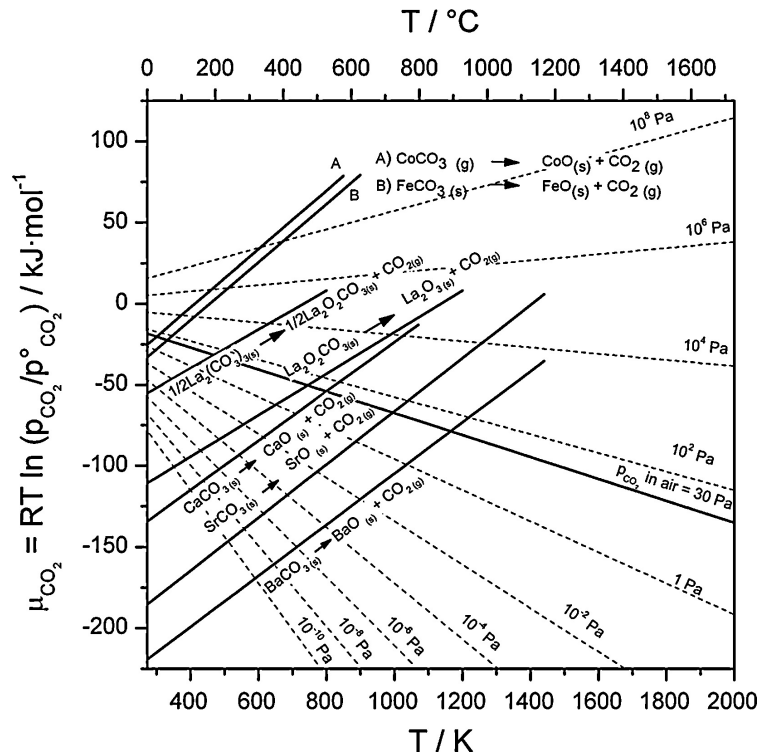


Figure 1.6. Ellingham diagram for the temperature-dependent thermochemical stability of carbonate under different CO_2 partial pressures.^[75]

Doping of the *B*-site has also been considered as an effective strategy for stabilization of the perovskite structure against carbonate formation. Zr-doping of the *B*-site of the proton-conducting $\text{BaCe}_{0.8}\text{Y}_{0.2}\text{O}_{3-\delta}$ resulted in improved CO_2 stability.^[80] According to Zeng *et al.* stability of SCF against acidic CO_2 could be increased by reducing the surface basicity of the perovskite by Ti-doping. Lower surface basicity of $\text{Sr}(\text{Co}_{0.8}\text{Fe}_{0.2})_{0.9}\text{Ti}_{0.1}\text{O}_{3-\delta}$ was attributed to the higher bond energy of Ti-O, compared to those of Fe-O and Co-O, which results in reduced charge density of the oxide ion.^[81] Other high valence cations, such as Nb^{5+} and Ta^{5+} , have also been considered as stabilizing dopants of the *B*-site owing to their relatively high electron affinities. A relative improvement of CO_2 resistivity could be achieved by 20 at.% Nb-doping of $\text{Ba}(\text{Co,Fe})\text{O}_{3-\delta}$, at the cost of decreased oxygen permeability.^[82] Chen *et al.* reported an improved CO_2 stability of SCF by 10 at.% Ta-doping at the *B*-site. Although $\text{Sr}(\text{Co}_{0.8}\text{Fe}_{0.2})_{0.9}\text{Ta}_{0.1}\text{O}_{3-\delta}$ showed lower oxygen permeability in comparison with SCF, the oxygen permeation fluxes were found to be relatively stable for 50 h at 900 °C.^[83]

One of the recent advancements in development of CO_2 -stable membranes for oxygen separation is the concept of composite dual-phase MIECs, which will be discussed in more detail in the following section.

1.3.2. Dual-Phase Compositions

The concept of dual-phase oxygen-transporting membranes is based on a matrix of an ionic-conducting phase and an electronic-conducting phase. The mixed ionic-conducting properties are achieved by formation of a percolation network of these two phases. Moreover, the thermochemical stability of the membrane under harsh practical conditions (including operation in CO₂-rich environments) can be remarkably enhanced by utilization of a highly stable ionic-conducting phase, such as yttrium-stabilized zirconia (YSZ) or doped ceria. The ionic-conducting phase is considered as the main phase, while the electronic-conducting phase functions as an internal short-circuit.^[84] Accordingly, by the assumption of a network consisting of randomly distributed phases, a percolation threshold should be attained. In other words, a critical fraction volume should be considered, above which the theoretical long-range connectivity of each phase is preserved.^[85]

The first-generation dual-phase MIECs contained noble metals (mainly Ag and Pd) as ionic conductors, *e.g.* YSZ-Pd,^[86] Bi_{1.5}Er_{0.5}O₃-Ag,^[87] (Bi₂O₃)_{0.74}(SrO)_{0.26}-Ag,^[88] and Bi_{1.5}Y_{0.3}Sm_{0.2}O₃-Ag.^[89] However, some drawbacks associated with the noble metal phase, led to the development of ceramic-ceramic dual-phase composites. The major issues of the metallic phase in the first-generation dual-phase membranes can be summarized as high production costs and low mechanical strength, due to the mismatch of thermal expansion coefficients of the two phases. Furthermore, oxygen permeation performances of these membranes were reported to be poor.^[90] The new concept of dual-phase MIECs relies on the replacement of the electronic-conducting noble metal phase, with an electronic-conducting or a mixed-conducting oxide phase, such as spinels or perovskites, thus improving the cost efficiency and thermomechanical properties of the membranes. Fluorite-type oxides with high thermochemical stability are commonly applied as the oxygen ionic-conducting phase. Some examples of the metal-free dual-phase membranes include Ce_{0.8}Gd_{0.2}O_{2-δ}-La_{0.7}Sr_{0.3}MnO_{3-δ},^[90] Ce_{0.8}Gd_{0.2}O_{2-δ}-La_{0.8}Sr_{0.2}Fe_{0.8}Co_{0.2}O_{3-δ},^[91] Zr_{0.8}Y_{0.2}O_{0.9-}La_{0.8}Sr_{0.2}CrO_{3-δ},^[92] and Ce_{0.8}Sm_{0.2}O_{1.9}-SmMn_{0.5}Co_{0.5}O₃.^[93] Although the oxygen permeability of these membranes is generally higher than those of the noble metal-containing dual-phase membranes, further improvement of the permeation properties of ceramic-based dual-phase membranes is essential for their large-scale technological

application. Moreover, high contents of alkaline earth cations in the perovskite phase can impair the thermochemical stability of perovskite-based membranes in CO₂-containing environments. Several approaches have been pursued to enhance the permeation performance of dual-phase membranes, while maintaining a reasonable stability under the practice-relevant conditions.

Dual-phase compositions with good stability against CO₂ have been developed by exclusion of CO₂-susceptible alkaline earth elements Ba and Sr. Luo *et al.* reported high CO₂ stability for a dual-phase membrane (NFO-CGO), containing 40 wt.% NiFe₂O₄ as the spinel-structured electron conductor and 60 wt.% Ce_{0.9}Gd_{0.1}O_{2-δ} as the fluorite-type ionic-conducting phase.^[94] However, poor stability of the NFO-CGO membrane under low oxygen partial pressures, led to the development of a nickel-free membrane (FO-CGO), where the spinel phase was replaced with Fe₂O₃.^[95] Despite increased stability, both the NFO-CGO and FO-CGO membranes show low oxygen permeabilities.

Zhu *et al.* investigated the influence of membrane preparation methods on the oxygen permeation properties of dual-phase membrane with the composition 75 wt.% Ce_{0.85}Sm_{0.15}O_{1.925}- 25 wt.% Sm_{0.6}Sr_{0.4}Al_{0.3}Fe_{0.7}O₃. It was reported that by using a solid-state reaction method the distribution of the phases in the membrane was less homogeneous compared to that of the membranes prepared by the conventional EDTA/citric acid complexing method. Zhu *et al.* concluded that in a less homogenous system, mixed-conducting properties could still be achieved with the volume fraction of the perovskite being lower than the percolation threshold.^[96] Further means of providing an internal electronic short-circuit by incorporation of abridged electronic-conducting pathways have been proposed. The mixed-conduction performance of Pr_{0.6}Sr_{0.4}Fe_{0.8}Co_{0.2}O₃- Ce_{0.8}Sm_{0.2}O_{1.9} composite material could be enhanced by using vertically aligned carbon nanotubes, which is suitable for intermediate-temperature applications such as in SOFCs.^[97] Chen *et al.* prepared a dual-phase membrane with 20 vol.% double perovskite PrBaCo₂O_{5+δ} in form of a fiber-like interconnecting phase to mediate the electronic conduction.^[98] However, high contents of Ba and Co are expected to impair the stability properties of this membrane.

Although the CO₂ stability of OTMs is of crucial importance, the oxygen permeation performance of the dual-phase membranes requires further optimization for potential technological applications. Different doping strategies, mainly targeting

the improvement of conduction properties of CO₂-tolerant dual-phase OTMs will be discussed in Chapters 4 and 5.

1.4. Oxygen-Transporting Membranes (OTMs)

1.4.1. Preparation of OTMs

A number of established methods can be employed for the production of MIECs, such as solid-state reaction, co-precipitation, sol-gel techniques, spray pyrolysis, and hydrothermal synthesis.^[99,100] Solid-state reaction and sol-gel synthesis can be counted as the most commonly used techniques for the preparation of powder compositions. In the solid-state method, oxides, carbonates or hydroxides of the associated metals are ground, mixed and reacted in a high-energy milling process. The microstructure and phase purity of the product is strongly dependent on the duration and quality of the mixing process. Low homogeneity and broad particle size distribution are considered to be the main disadvantages of the solid-state synthesis route.^[101]

All of the synthesis procedures included in the present work, are accomplished *via* a sol-gel synthesis route, due its simplicity, high efficiency, homogeneity and precision in control of the stoichiometric composition of the products. Sol-gel synthesis route is a simple method based on preparation of a precursor solution, called sol, which is a highly homogeneous dispersion of the solid components in an aqueous or organic solution. The required level of distribution can be achieved by addition of complexing agents, such as ethylenediamine tetraacetic acid (EDTA) and citric acid (CA). After an aging stage, which may involve heat treatment of the precursor, the sol is transformed into a viscous gel, containing highly dispersed metal components in a three-dimensional matrix of organic ligands. Subsequently, the product can be obtained in form of a high-purity mixed-oxide powder, after the evaporation and calcination procedures for the complete removal of organic species and carbonates.^[102]

1.4.2. Oxygen Permeation Measurements

Oxygen permeation measurements are conducted on gas-tight membranes, prepared from the powder sample of the related MIEC after a sintering process. Since the microstructure and consequently the permeation properties of the membrane are strongly dependent on the sintering process, this step is of crucial importance for the preparation of dense membranes. During sintering, the powder is heated close to the melting point of its main constituents, which enables the particles to relocate and increase the number of adjoining neighbors. Grain boundaries are formed and material is diffused from regions of high chemical potential to regions of lower chemical potential. The driving force of sintering is the reduction of the surface free energy of the system.^[103]

The membranes studied in the present work were prepared by uniaxial pressing of the related powders into green disk pellets, followed by sintering in ambient air. The optimum sintering conditions were determined empirically.

For the evaluation of the oxygen permeation properties, the membranes were fixed unto an alumina tube using gold cermet (conduction paste C5754, Heraeus, Germany) and placed in a high-temperature permeation cell, as schematically shown in Figure 1.7, where the membrane could be exposed to oxygen partial pressure gradients, by applying a stream of an oxygen-rich feed gas one side of the membrane (feed side), while sweeping the permeated oxygen on the opposite side of the membrane (sweep side) with an inert carrier gas. Subsequently, the sweep gas was quantitatively analyzed by an on-line gas chromatograph (GC). Synthetic air, consisting of 80 vol.% N₂ and 20 vol.% O₂, was used as the feed gas. The sweep gas contained pure He, as the inert carrier gas, which was switched to pure CO₂ for the investigation of the membrane's performance under CO₂-rich conditions. The concentration of oxygen in the effluent was calculated according to the related calibration curves. Possible oxygen leakage, caused by insufficient sealing or other impairments could be directly detected by monitoring the concentration of N₂ in the effluent, and subtracted from the total oxygen flux. Neon at a flow of 1.0 cm³ min⁻¹ was added to the sweep gas, as an internal standard for the determination of the total flow of effluent. In order to reduce error, the total flow was also frequently controlled by a soap-film flow meter.

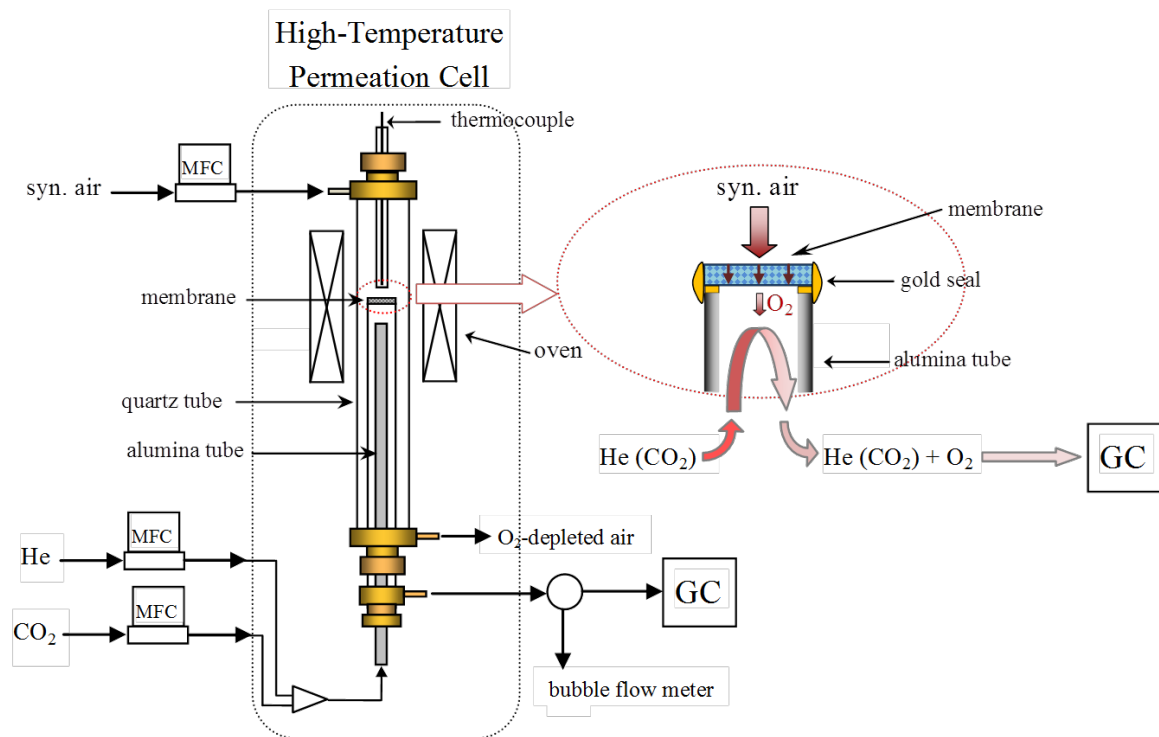


Figure 1.7. Schematic representation of the experimental setup used for the oxygen separation measurements.

1.5. Bibliography

- ¹ DOE/EIA-0484(2013), *International Energy Outlook 2013*, July 2013, Washington DC.
- ² UNEP (2012), *The Emissions Gap Report 2012*. United Nations Environment Programme (UNEP), Nairobi.
- ³ IEA (2014), *CO₂ Emissions from Fuel Combustion 2014*, IEA, Paris.
- ⁴ Schrag, D. P. Preparing to Capture Carbon; *Science* **2007**, *315*, 812-813.
- ⁵ Haszeldine, R. S. Carbon Capture and Storage: How Green Can Black Be? *Science* **2009**, *325*, 1647-1652.
- ⁶ Wang, M.; Lawal, A.; Stephenson, P.; Sidders, J.; Ramshaw, C. Post-Combustion CO₂ Capture with Chemical Absorption: A State-of-the-Art Review. *Chem. Eng. Res. Des.* **2011**, *89*, 1609-1624.
- ⁷ CO₂ Capture and Storage: A Key Carbon Abatement Option; OECD/IEA 2008, Paris, France.
- ⁸ Markewitz, P.; Kuckshinrichs, W.; Leitner, W.; Linssen, J.; Zapp, P.; Bongartz, R.; Schreiber, A.; Müller, T. E. Worldwide Innovations in the Development of Carbon Capture Technologies and the Utilization of CO₂. *Energy Environ. Sci.* **2012**, *5*, 7281-7305.
- ⁹ Adams D. *Flue Gas Treatment for CO₂ Capture*, IEA Clean Coal Centre, 2010.
- ¹⁰ Romeo, L. M.; Bolea, I.; Escosa, J. M. Integration of Power Plant and Amine Scrubbing to Reduce CO₂ Capture Costs. *Appl. Therm. Eng.* **2008**, *28*, 1039–1046.
- ¹¹ Habib, M.; Badr, H.; Ahmed, S.; Ben-Mansour, R.; Mezghani, K.; Imashuku, S.; O', G.; Shao-Horn, Y.; Mancini, N.; Mitsos, A.; Kirchen, P.; Ghoneim, A. F. A Review of Recent Developments in Carbon Capture Utilizing Oxy-fuel Combustion in Conventional and Ion Transport Membrane Systems. *Int. J. Energy Res.* **2011**, *35*, 741–764.
- ¹² Kanniche, M.; Gros-Bonnivard, R.; Jaud, P.; Valle-Marcos, J.; Amann, J.-M.; Bouallou, C. Pre-Combustion, Post-Combustion and Oxy-Combustion in Thermal Power Plant for CO₂ Capture. *Appl. Therm. Eng.* **2010**, *30*, 53-62.
- ¹³ Wall, T.; Liu, Y.; Spero, C.; Elliott, L.; Khare, S.; Rathnam, R.; Zeenathal, F.; Moghtaderi, B.; Buhre, B.; Sheng, C.; Gupta, R.; Yamada, T.; Makino, K.; Yu, J. An Overview on Oxyfuel Coal Combustion—State of the Art Research and

- Technology Development. *Chem. Eng. Res. Des.* **2009**, *87*, 1003-1016.
- ¹⁴ Schulz, M.; Kriegel, R.; Kämpfer, A. Assessment of CO₂ Stability and Oxygen Flux of Oxygen Permeable Membranes. *J. Membr. Sci.* **2011**, *378*, 10-17.
- ¹⁵ Czaperek, M.; Zapp, P.; Bouwmeester, H. J. M.; Modigell, M.; Ebert, K.; Voigt, I.; Meulenbergh, W. A.; Singheiser, L.; Stöver, D. Gas Separation Membranes for Zero-Emission Fossil Power Plants: MEM-BRAIN. *J. Membr. Sci.* **2010**, *359*, 149-159.
- ¹⁶ Engels, S.; Beggel, F.; Modigell, M.; Stadler, H. Simulation of a Membrane Unit for Oxyfuel Power Plants under Consideration of Realistic BSCF Membrane Properties. *J. Membr. Sci.* **2010**, *359*, 93-101.
- ¹⁷ Kneer, R.; Toporov, D.; Förster, M.; Christ, D.; Broeckmann, C.; Pfaff, E.; Zwick, M.; Engels, S.; Modigell, M. OXYCOAL-AC: Towards an Integrated Coal-Fired Power Plant Process with Ion Transport Membrane-Based Oxygen Supply. *Energy Environ. Sci.* **2010**, *3*, 198-207.
- ¹⁸ Stadler, H.; Beggel, F.; Habermehl, M.; Persigehl, B.; Kneer, R.; Modigell, M.; Jeschke, P. Oxyfuel Coal Combustion by Efficient Integration of Oxygen Transport Membranes. *Int. J. Greenhouse Gas Control* **2011**, *5*, 7-15.
- ¹⁹ Arnold, M.; Wang, H. H.; Feldhoff, A. Influence of CO₂ on the Oxygen Permeation Performance and the Microstructure of Perovskite-Type (Ba_{0.5}Sr_{0.5})(Co_{0.8}Fe_{0.2})O_{3-δ}. *J. Membr. Sci.* **2007**, *293*, 44-52.
- ²⁰ Czuprat, O.; Arnold, M.; Schirrmeyer, S.; Schiestel, T.; Caro, J. Influence of CO₂ on the Oxygen Permeation Performance of Perovskite-Type BaCo_xFe_yZr_zO_{3-δ} Hollow Fibre Membranes. *J. Membr. Sci.* **2010**, *364*, 132-137.
- ²¹ Bouwmeester, H. J. M.; Burggraaf, A. J. In *Fundamentals of Inorganic Membrane Science and Technology*; Burggraaf, A. J.; Cot, L., Eds.; Elsevier Science B. V., Amsterdam, The Netherlands **1996**, Chapter 10, pp 435-528.
- ²² Balachandran, U.; Ma, B.; Maiya, P. S.; Mievil, R. L.; Dusek, J. T.; Picciolo, J. J.; Guan, J.; Dorris, S. E.; Liu, M. Development of Mixed-Conducting Oxides for Gas Separation. *Solid State Ionics* **1998**, *108*, 363-370.
- ²³ Dyer, P. N.; Richards, R. E.; Russek, S. L.; Taylor, D. M. Ion Transport Membrane Technology for Oxygen Separation and Syngas Production. *Solid State Ionics* **2000**, *134*, 21-33.

- ²⁴ Balachandran, U.; Dusek, J. T.; Mievilte, R. L.; Poeppel, R. B.; Kleefisch, M. S.; Pei, S.; Kobylinski, T. P.; Udovich, C. A.; Bose, A. C. Dense Ceramic Membranes for Partial Oxidation of Methane to Syngas. *Appl. Catal., A* **1995**, *133*, 19-29.
- ²⁵ Caro, J.; Caspary, K. J.; Hamel, C.; Hoting, B.; Koelsch, P.; Langanke, B.; Nassauer, K.; Schiestel, T.; Schmidt, A.; Schomaecker, R.; Seidel-Morgenstern, A.; Tsotsas, E.; Voigt, I.; Wang, H.; Warsitz, R.; Werth, S.; Wolf, A. Catalytic Membrane Reactors for Partial Oxidation Using Perovskite Hollow Fiber Membranes and for Partial Hydrogenation Using a Catalytic Membrane Contactor. *Ind. Eng. Chem. Res.* **2007**, *46*, 2286-2294.
- ²⁶ Jiang, H. Q.; Cao, Z. W.; Schirrmeister, S.; Schiestel, T.; Caro, J. A Coupling Strategy to Produce Hydrogen and Ethylene in a Membrane Reactor. *Angew. Chem. Int. Ed.* **2010**, *49*, 5656-5660.
- ²⁷ Liang, F. Y.; Caro, J. Perovskite Membranes for High Temperature Oxygen Separation. In *Membrane Engineering for the Treatment of Gases*; Drioli, E., Barbieri, G., Eds.; Royal Society of Chemistry, July **2011**; Vol. 2, pp. 192-221.
- ²⁸ Lin, Y. S.; Zeng, Y. Catalytic Properties of Oxygen Semipermeable Perovskite-Type Ceramic Membrane Materials for Oxidative Coupling of Methane. *J. Catal.* **1996**, *164*, 220-231.
- ²⁹ Tan, X.; Li, K.; Thursfield, A.; Metcalfe, I. S. Oxyfuel Combustion Using a Catalytic Ceramic Membrane Reactor. *Catal. Today* **2008**, *131*, 292-304.
- ³⁰ Shao, Z. P.; Haile, S. M. A High-Performance Cathode for the Next Generation of Solid-Oxide Fuel Cells. *Nature* **2004**, *431*, 170-173.
- ³¹ Huang, K.; Wan, J.; Goodenough, J. B. Oxide-Ion Conducting Ceramics for Solid Oxide Fuel Cells. *J. Mater. Sci.* **2001**, *36*, 1093-1098.
- ³² Teraoka, Y.; Zhang, H. M.; Furukawa, S.; Yamazoe N. Oxygen Permeation through Perovskite-Type Oxides. *Chem. Lett.* **1985**, 1743-1746.
- ³³ Kingery, W. D.; Pappis, J.; Doty, M. E.; Hill, D. C. Oxygen Ion Mobility in Cubic $Zr_{0.85}Ca_{0.15}O_{1.85}$. *J. Am. Ceram. Soc.* **1959**, *42*, 393.
- ³⁴ Minervini, L.; Grimes, R. W.; Kilner, J. A.; Sickafus, K. E. Oxygen Migration in $La_2NiO_{4+\delta}$. *J. Mater. Chem.* **2000**, *10*, 2349-2354.

- ³⁵ Shao, Z. P.; Yang, W. S.; Cong, Y.; Dong, H.; Tong, J. H.; Xiong, G. X. Investigation of the Permeation Behavior and Stability of a $\text{Ba}_{0.5}\text{Sr}_{0.5}\text{Co}_{0.8}\text{Fe}_{0.2}\text{O}_{3-\delta}$ Oxygen Membrane. *J. Membr. Sci.* **2000**, *172*, 177-188.
- ³⁶ Goldschmidt, V. M. Geochemische Verteilungsgesetze der Elemente VII. die Gesetze der Krystallochemie *Skr. Nor. Viedenk.-Akad.*, Kl. I: Mater.-Naturvidensk. Kl. **1926**, No.8.
- ³⁷ Garcia-Munoz, J. L.; Rodriguez-Carvajal, J. Neutron-Diffraction Study of RNiO_3 (R=La,Pr,Nd,Sm)- Electronically Induced Structural Changes across the Metal-Insulator Transition. *Phys. Rev. B* **1992**, *46*, 4414-4425.
- ³⁸ Ramadass, N. ABO_3 -Type Oxides – Their Structure and Properties – A Bird’s Eye View. *Mater. Sci. Eng.* **1978**, *36*, 231-239.
- ³⁹ Stolen, S.; Bakken, E.; Mohn, C. E. Oxygen-Deficient Perovskites: Linking Structures, Energetics, and Ion Transport. *Phys. Chem. Chem. Phys.* **2005**, *8*, 429-447.
- ⁴⁰ Fisher, C. A. J.; Yoshiya, M.; Iwamoto, Y.; Ishii, J.; Asanuma, M.; Yabuta, K. Oxide Ion Diffusion in Perovskite-Structured $\text{Ba}_{1-x}\text{Sr}_x\text{Co}_{1-y}\text{Fe}_y\text{O}_{2.5}$: A Molecular Dynamics Study. *Solid State Ionics* **2007**, *177*, 3425-3431.
- ⁴¹ Kharton, V. V.; Viskup, A. P.; Kovalevsky, A. V.; Naumovich, E. N.; Marques, F. M. B. Ionic Transport in Oxygen-Hyperstoichiometric Phases with K_2NiF_4 -Type Structure. *Solid State Ionics* **2001**, *143*, 337-353.
- ⁴² Stevenson, J. W.; Armstrong, T. R.; Carneim, R. D.; Pederson, L. R.; Weber W. J. Electrochemical Properties of Mixed Conducting Perovskites $\text{La}_{1-x}\text{M}_x\text{Co}_{1-y}\text{Fe}_y\text{O}_{3-\delta}$ (M= Sr, Ba, Ca). *J. Electrochem. Soc.* **1996**, *143*, 2722-2729.
- ⁴³ ten Elshof, J. E.; Bouwmeester, H. J. M.; Verweij, H. Oxygen Transport through $\text{La}_{1-x}\text{Sr}_x\text{FeO}_{3-\delta}$ I. Permeation in Air/He Gradients. *Solid State Ionics* **1995**, *81*, 97-109.
- ⁴⁴ Tai, L. W.; Nasrallah, M. M.; Anderson, H. U.; Sparlin, D. M.; Sehlin S. R. Structural and Electrical Properties of $\text{La}_{1-x}\text{Sr}_x\text{Co}_{1-y}\text{Fe}_y\text{O}_3$. Part 2. The System $\text{La}_{1-x}\text{Sr}_x\text{Co}_{0.2}\text{Fe}_{0.8}\text{O}_3$. *Solid State Ionics* **1995**, *76*, 273-283.
- ⁴⁵ Kröger F. A.; Vink, H. J. Relations between the Concentrations of Imperfections in Crystalline Solids, in: *Solid State Physics*; Academic Press: New York, 1956, pp. 307-435.

- ⁴⁶ Cao, G. Z. Electrical Conductivity and Semipermeability of the Terbia and Ytria Stabilized Zirconia. *J. Appl. Electrochem.* **1994**, *24*, 1222-1227.
- ⁴⁷ Bouwmeester, H. J. M.; Kruidhof, H.; Burggraaf, A. J.; Gellings, P. J. Oxygen Semipermeability of Erbia-Stabilized Bismuth Oxide. *Solid State Ionics* **1992**, *53*, 460-468.
- ⁴⁸ Bouwmeester, H. J. M.; Kruidhof, H.; Burggraaf, A. J. Importance of the Surface Exchange Kinetics as Rate Limiting Step in Oxygen Permeation through Mixed-Conducting Oxides. *Solid State Ionics* **1994**, *72*, 185-194.
- ⁴⁹ Wagner, C. Equations for Transport in Solid Oxides and Sulfides of Transition Metals. *Prog. Solid State Chem.* **1975**, *10*, 3-16.
- ⁵⁰ Van Hassel, B. A.; Kawada, T.; Sakai, N.; Yokokawa, H.; Dokiya, M.; Bouwmeester, H. J. M. Oxygen Permeation Modelling of Perovskites. *Solid State Ionics* **1993**, *66*, 295-305.
- ⁵¹ ten Elshof, J. E.; Bouwmeester, H. J. M.; Verweij, H. Oxidative Coupling of Methane in a Mixed-Conducting Perovskite Membrane Reactor. *Appl. Catal. A: Gen.* **1995**, *130*, 195-212.
- ⁵² Ishigaki, T.; Yamauchi, S.; Kishio, K.; Mizusaki, J.; Fueki, K. Diffusion of Oxide Ion Vacancies in Perovskite-Type Oxides. *J. Solid State Chem.* **1988**, *73*, 179-187.
- ⁵³ Teraoka, Y.; Zhang, H. M.; Okamoto, K.; Yamazoe, N. Mixed Ionic-Electronic Conductivity of $\text{La}_{1-x}\text{Sr}_x\text{Co}_{1-y}\text{Fe}_y\text{O}_{3-\delta}$ Perovskite-Type Oxides. *Mater. Res. Bull.* **1988**, *23*, 51-58.
- ⁵⁴ Vente, J. F.; McIntosh, S.; Haije, W. G.; Bouwmeester, H. J. M. Properties and Performance of $\text{Ba}_x\text{Sr}_{1-x}\text{Co}_{0.8}\text{Fe}_{0.2}\text{O}_{3-\delta}$ for Oxygen Transport Membranes. *J. Solid State Electrochem.* **2006**, *10*, 581-588.
- ⁵⁵ Qiu, L.; Lee, T. H.; Liu, L. M.; Yang, Y. L.; Jacobson, A. J. Oxygen Permeation Studies of $\text{SrCo}_{0.8}\text{Fe}_{0.2}\text{O}_{3-\delta}$. *Solid State Ionics* **1995**, *76*, 321-329.
- ⁵⁶ Chen, C.-S.; Zhang, Z. P.; Jiang, G. S.; Fan, C. G.; Liu, W.; Bouwmeester, H. J. M. Oxygen Permeation through $\text{La}_{0.6}\text{Sr}_{0.4}\text{Co}_{0.2}\text{Fe}_{0.8}\text{O}_{3-\delta}$ Membrane. *Chem. Mater.* **2001**, *13*, 2797-2800.
- ⁵⁷ Borchert, Y.; Sonstrom, P.; Wilhelm, M.; Borchert, H.; Baumer, M. Nanostructured Praseodymium Oxide: Preparation, Structure, and Catalytic Properties. *J. Phys. Chem. C* **2008**, *112*, 3054-3063.

- ⁵⁸ Kruidhof, H.; Bouwmeester, H. J. M.; v. Doorn, R. H. E.; Burggraaf, A. J. Influence of Order-Disorder Transitions on Oxygen Permeability through Selected Nonstoichiometric Perovskite-Type Oxides. *Solid State Ionics* **1993**, *63-65*, 816-822.
- ⁵⁹ Chen, W.; Zuo, Y. B.; Chen, C. S.; Winnubst, A. J. A. Effect of Zr⁴⁺ Doping on the Oxygen Stoichiometry and Phase Stability of SrCo_{0.8}Fe_{0.2}O_{3-δ} Oxygen Separation Membrane. *Solid State Ionics* **2010**, *181*, 971-975.
- ⁶⁰ Prado, F.; Grunbaum, N.; Caneiro, A.; Manthiram, A. Effect of La³⁺ Doping on the Perovskite-to-Brownmillerite Transformation in Sr_{1-x}La_xCo_{0.8}Fe_{0.2}O_{3-δ} (0 ≤ x ≤ 0.4). *Solid State Ionics* **2004**, *167*, 147-154.
- ⁶¹ Arnold, M.; Gesing, T. M.; Martynczuk, J.; Feldhoff, A. Correlation of the Formation and the Decomposition Process of the BSCF Perovskite at Intermediate Temperatures. *Chem. Mater.* **2008**, *20*, 5851-5858.
- ⁶² Svarcova, S.; Wiik, K.; Tolchar, J.; Bouwmeester, H. J. M.; Grande, T. Structural Instability of Cubic Perovskite Ba_xSr_{1-x}Co_{1-y}Fe_yO_{3-δ}. *Solid State Ionics* **2008**, *178*, 1787-1791.
- ⁶³ Yakovlev, S.; Yoo, C.-Y.; Fang, S.; Bouwmeester, H. J. M. Phase Transformation and Oxygen Equilibration Kinetics of Pure and Zr-Doped Ba_{0.5}Sr_{0.5}Co_{0.8}Fe_{0.2}O_{3-δ} Perovskite Oxide Probed by Electrical Conductivity Relaxation. *Appl. Phys. Lett.* **2010**, *96*, 254101.
- ⁶⁴ Teraoka, Y.; Nobunaga, T.; Yamazoe, N. Effect of Cation Substitution on the Oxygen Semipermeability of Perovskite-Type Oxides. *Chem. Lett.* **1988**, 503-506.
- ⁶⁵ Petric, A.; Huang, P.; Tietz, F. Evaluation of La-Sr-Co-Fe-O Perovskites for Solid Oxide Fuel Cells and Gas Separation Membranes. *Solid State Ionics* **2000**, *135*, 719-725.
- ⁶⁶ Tai, L. W.; Nasrallah, M. M.; Anderson, H. U.; Sparlin, D. M.; Sehlin S. R. Structural and Electrical Properties of La_{1-x}Sr_xCo_{1-y}Fe_yO₃. Part 1. The System La_{0.8}Sr_{0.2}Co_{1-y}Fe_yO₃. *Solid State Ionics* **1995**, *76*, 259-271.
- ⁶⁷ Shannon, R. D. Revised Effective Ionic Radii and Systematic Studies of Interatomic Distances in Halides and Chalcogenides. *Acta Crystallogr., Sect. A: Cryst. Phys., Diffr., Theor. Gen. Crystallogr.* **1976**, *32*, 751-767.
- ⁶⁸ Chen, Z.; Ran, R.; Zhou, W.; Shao, Z.; Liu, S. Assessment of Ba_{0.5}Sr_{0.5}Co_{1-y}Fe_yO_{3-δ} (y = 0.0-1.0) for Prospective Application as Cathode for IT-SOFCs or Oxygen Permeating Membrane. *Electrochim. Acta* **2007**, *52*, 7343-7351.

- ⁶⁹ Efimov, K.; Halfer, T.; Kuhn, A.; Heitjans, P.; Caro, J.; Feldhoff, A. Novel Cobalt-Free Oxygen-Permeable Perovskite-Type Membrane. *Chem. Mater.* **2010**, *22*, 1540-1544.
- ⁷⁰ Wang, H. H.; Tablet, C.; Feldhoff, A.; Caro, J. A Cobalt-Free Oxygen-Permeable Membrane Based on the Perovskite-Type Oxide $\text{Ba}_{0.5}\text{Sr}_{0.5}\text{Zn}_{0.2}\text{Fe}_{0.8}\text{O}_{3-\delta}$. *Adv. Mater.* **2005**, *17*, 1785-1788.
- ⁷¹ Martynczuk, J.; Liang, F. Y.; Arnold, M.; Sepelak, V.; Feldhoff, A. Aluminum-Doped Perovskites as High-Performance Oxygen Permeation Materials. *Chem. Mater.* **2009**, *21*, 1586-1594.
- ⁷² Liang, F. Y.; Partovi, K.; Jiang, H. Q.; Luo, H. X.; Caro, J. B-Site La-Doped $\text{BaFe}_{0.95-x}\text{La}_x\text{Zr}_{0.05}\text{O}_{3-\delta}$ Perovskite-Type Membranes for Oxygen Separation *J. Mater. Chem. A* **2013**, *1*, 746-751.
- ⁷³ Benson, S. J.; Waller, D.; Kilner, J. A. Degradation of $\text{La}_{0.6}\text{Sr}_{0.4}\text{Fe}_{0.8}\text{Co}_{0.2}\text{O}_{3-\delta}$ in Carbon Dioxide and Water Atmospheres. *J. Electrochem. Soc.* **1999**, *146*, 1305-1309.
- ⁷⁴ Pei, S.; Kleefisch, M. S.; Kobylinski, T. P.; Faber, J.; Udovich, C. A.; Zhang-McCoy V.; Dabrowski, B.; Balachandran, U.; Mieville, R. L.; Poeppel, R. B. Failure Mechanisms of Ceramic Membrane Reactors in Partial Oxidation of Methane to Synthesis Gas. *Catal. Lett.* **1995**, *30*, 201-212.
- ⁷⁵ Efimov, K.; Klande, T.; Juditzki, N.; Feldhoff, A. Ca-Containing CO_2 -Tolerant Perovskite Materials for Oxygen Separation. *J. Membr. Sci.* **2012**, *389*, 205-215.
- ⁷⁶ Stern, K. H.; Weise, E. L. High Temperature Properties and Decomposition of Inorganic Salts, Part 2: Carbonates, NSRDS-NBS **1969**, *30*, 1-27.
- ⁷⁷ Yokokawa, H.; Sakai, N.; Kawada, T.; Dokiya, M. Thermodynamic Stabilities of Perovskite Oxides for Electrodes and Other Electrochemical Materials *Solid State Ionics* **1992**, *52*, 43-56.
- ⁷⁸ Klande, T.; Ravkina, O.; Feldhoff, A. Effect of A-Site Lanthanum Doping on the CO_2 Tolerance of $\text{SrCo}_{0.8}\text{Fe}_{0.2}\text{O}_{3-\delta}$ Oxygen-Transporting Membranes. *J. Membr. Sci.* **2013**, *437*, 122-130.
- ⁷⁹ Tan, X.; Liu, N.; Meng, B.; Sunarso, J.; Zhang, K.; Liu, S. Oxygen Permeation Behavior of $\text{La}_{0.6}\text{Sr}_{0.4}\text{Co}_{0.8}\text{Fe}_{0.2}\text{O}_3$ Hollow Fibre Membranes with Highly Concentrated CO_2 Exposure. *J. Membr. Sci.* **2012**, *389*, 216-222.

- ⁸⁰ Zuo, C. D.; Dorris, S. E.; Balachandran, U.; Liu, M. L. Effect of Zr-Doping on the Chemical Stability and Hydrogen Permeation of the Ni BaCe_{0.8}Y_{0.2}O_{3-δ} Mixed Protonic Electronic Conductor. *Chem. Mater.* **2006**, *18*, 4647-4650.
- ⁸¹ Zeng, Q.; Zuo, Y.; Fan, C.; Chen, C. CO₂-Tolerant Oxygen Separation Membranes Targeting CO₂ Capture Application. *J. Membr. Sci.* **2009**, *335*, 140-144.
- ⁸² Yi, J.; Schroeder, M.; Weirich, T.; Mayer, J. Behavior of Ba(Co, Fe, Nb)O_{3-δ} Perovskite in CO₂-Containing Atmospheres: Degradation Mechanism and Materials Design. *Chem. Mater.* **2010**, *22*, 6246-6253.
- ⁸³ Chen, W.; Chen, C.; Winnubst, L. Ta-Doped SrCo_{0.8}Fe_{0.2}O_{3-δ} Membranes: Phase Stability and Oxygen Permeation in CO₂ Atmosphere. *Solid State Ionics* **2011**, *196*, 30-33.
- ⁸⁴ Mazanec, T. J.; Cable, T. L.; Frye, Jr. J.G. Electrocatalytic Cells for Chemical Reaction. *Solid State Ionics* **1992**, *53-56*, 111-118.
- ⁸⁵ Chen, C. S.; Boukamp, B. A.; Bouwmeester, H. J. M.; Cao, G. Z.; Kruidhof, H.; Winnubst, A. J. A.; Burggraaf, A. J. Microstructural Development, Electrical Properties and Oxygen Permeation of Zirconia-Palladium Composites. *Solid State Ionics* **1995**, *76*, 23-28.
- ⁸⁶ Chen, C. S.; Kruidhof, H.; Bouwmeester, H. J. M.; Verweij, H.; Burggraaf, A. J. Oxygen Permeation through Oxygen Ion Oxide-Noble Metal Dual Phase Composites. *Solid State Ionics* **1996**, *86-88*, 569-572.
- ⁸⁷ ten Elshof, J. E.; Nguyen, N. Q.; den Otter, M. W.; Bouwmeester, H. J. M. Oxygen Permeation Properties of Dense Bi_{1.5}Er_{0.5}O₃-Ag Cermet Membranes. *J. Electrochem. Soc.* **1997**, *144*, 4361-4366.
- ⁸⁸ Wu, K.; Xie, S.; Jiang, G. S.; Liu, W.; Chen, C. S. Oxygen Permeation through (Bi₂O₃)_{0.74}(SrO)_{0.26}-Ag (40% v/o) Composite. *J. Membr. Sci.* **2001**, *188*, 189-193.
- ⁸⁹ Kim, J.; Lin, Y. S. Synthesis and Oxygen Permeation Properties of Ceramic-Metal Dual-Phase Membranes. *J. Membr. Sci.* **2000**, *167*, 123-133.
- ⁹⁰ Kharton, V. V.; Kovalevsky, A. V.; Viskup, A. P.; Figueiredo, F. M.; Yaremchenko, A. A.; Naumovich, E. N.; Marques, F. M. B. Oxygen Permeability of Ce_{0.8}Gd_{0.2}O_{2-δ}-La_{0.7}Sr_{0.3}MnO_{3-δ} Composite Membranes *J. Electrochem. Soc.* **2000**, *147*, 2814-2821.

- ⁹¹ Kharton, V. V.; Kovalevsky, A. V.; Viskup, A. P.; Shaula, A. L.; Figueiredo, F. M.; Naumovich, E. N.; Marques, F. M. B. Oxygen Transport in $\text{Ce}_{0.8}\text{Gd}_{0.2}\text{O}_{2-\delta}$ -Based Composite Membranes. *Solid State Ionics* **2003**, *160*, 247-258.
- ⁹² Wang, B.; Zhan, M. C.; Zhu, D. C.; Liu, W.; Chen, C. S. Oxygen Permeation and Stability of $\text{Zr}_{0.8}\text{Y}_{0.2}\text{O}_{0.9}$ - $\text{La}_{0.8}\text{Sr}_{0.2}\text{CrO}_{3-\delta}$ Dual-Phase Composite. *J. Electrochem. Soc.* **2006**, *10*, 625-628.
- ⁹³ Zhu, X. F.; Liu, H.; Cong, Y.; Yang, W. Novel Dual-Phase Membranes for CO_2 Capture via an Oxyfuel Route. *Chem. Commun.* **2012**, *48*, 251-253.
- ⁹⁴ Luo, H. X.; Efimov, K.; Jiang, H. Q.; Feldhoff, A.; Wang, H. H.; Caro, J. CO_2 -Stable and Cobalt-Free Dual-Phase Membrane for Oxygen Separation. *Angew. Chem. Int. Ed.* **2011**, *50*, 759-763.
- ⁹⁵ Luo, H. X.; Jiang, H. Q.; Efimov, K.; Liang, F. Y.; Wang, H. H.; Caro, J. CO_2 -Tolerant Oxygen-Permeable Fe_2O_3 - $\text{Ce}_{0.9}\text{Gd}_{0.1}\text{O}_{2-\delta}$ Dual Phase Membranes. *Ind. Eng. Chem. Res.* **2011**, *50*, 13508-13517.
- ⁹⁶ Zhu, X. F.; Liu, Y.; Cong, Y.; Yang, W. S. $\text{Ce}_{0.85}\text{Sm}_{0.15}\text{O}_{1.925}$ - $\text{Sm}_{0.6}\text{Sr}_{0.4}\text{Al}_{0.3}\text{Fe}_{0.7}\text{O}_3$ Dual-Phase Membranes: One-Pot Synthesis and Stability in a CO_2 Atmosphere. *Solid State Ionics* **2013**, *253*, 57-63.
- ⁹⁷ Pinedo, R.; Ruiz de Larramendi, I.; Khavrus, V. O.; Jimenez de Aberasturi, D.; Ruiz de Larramendi, J. I.; Ritscheld, M.; Leonhardt, A.; Rojo, T. Microstructural Improvements of the Gradient Composite Material $\text{Pr}_{0.6}\text{Sr}_{0.4}\text{Fe}_{0.8}\text{Co}_{0.2}\text{O}_3/\text{Ce}_{0.8}\text{Sm}_{0.2}\text{O}_{1.9}$ by Employing Vertically Aligned Carbon Nanotubes. *Int. J. Hydrogen Energ.* **2014**, *39*, 4074-4080.
- ⁹⁸ Chen, T.; Zhao, H.; Xie, Z.; Wang, J.; Lu, Y.; Xu, N. $\text{Ce}_{0.8}\text{Sm}_{0.2}\text{O}_{2-\delta}$ - $\text{PrBaCo}_2\text{O}_{5+\delta}$ Dual-Phase Membrane: Novel Preparation and Improved Oxygen Permeability. *J. Power Sources* **2013**, *223*, 289-292.
- ⁹⁹ Sunarso, J.; Baumann, S.; Serra, J. M.; Meulenberg, W. A.; Liu, S.; Lin, Y. S.; Diniz da Costa, J. C. Mixed Ionic-Electronic Conducting (MIEC) Ceramic-Based Membranes for Oxygen Separation. *J. Membr. Sci.* **2008**, *320*, 13-41.
- ¹⁰⁰ Garcia-Torregrosa, I.; Pilar Lobera, M.; Solis, C.; Atienzar, P.; Serra, J. M. Development of CO_2 Protective Layers by Spray Pyrolysis for Ceramic Oxygen Transport Membranes. *Adv. Energy Mater.* **2011**, *1*, 618-625.
- ¹⁰¹ Cousin, P.; Ross, R. A. Preparation of Mixed Oxides: A Review. *Mater. Sci. Eng. A* **1990**, *130*, 119-125.

- ¹⁰² Feldhoff, A.; Arnold, M.; Martynczuk, J.; Gesing, T. M.; Wang, H. H. The Sol-Gel Synthesis of Perovskites by an EDTA/Citrate Complexing Method Involves Nanoscale Solid State Reactions. *Solid State Sciences* **2008**, *10*, 689-701.
- ¹⁰³ Li, K. Ceramic Membranes for Separation and Reaction; John Wiley & Sons Ltd, Chichester, England 2007.

Chapter 2

Effect of Thermocycling on the Microstructure and Permeation Properties of a Single-Phase Perovskite Membrane

2.1. Summary

As mentioned in Section 1.3.1, perovskite-type oxides are considered to be the most prominent OTMs in terms of oxygen permeation performance. For applications in CO₂-rich environments, (La,Sr)(Co,Fe)O_{3-δ} series have been extensively studied, due to their good stability and reasonable permeabilities.

The following chapter deals with the oxygen permeation properties of a newly developed single-phase perovskite membrane Pr_{0.6}Sr_{0.4}Co_{0.5}Fe_{0.5}O_{3-δ} (PSCF), which exhibited a better oxygen permeation performance compared to that of conventional LSCF. The stability of the membrane was investigated in a long-term oxygen permeation test, summing up to 1000 h in total. During these measurements under oxygen/CO₂ partial pressure gradients, the membrane was subjected to periodic thermal cycling in the temperature range of 850 and 1000 °C. The effect of thermal cycles on the microstructure and the oxygen permeation properties of the membrane were investigated and it was found that the oxygen permeation fluxes slightly increased after each thermal cycle. Furthermore, the CO₂ stability of the PSCF membrane was tested for 400 h at the constant temperature of 800 °C. SEM and EDXS were employed to study the microstructure and morphology of the membrane before and after long-term CO₂ exposure. The structural properties and phase transition behavior of PSCF were studied using high-temperature *in-situ* XRD in a 100 vol.% CO₂ atmosphere.

2.2. High-Flux Oxygen-Transporting Membrane

$\text{Pr}_{0.6}\text{Sr}_{0.4}\text{Co}_{0.5}\text{Fe}_{0.5}\text{O}_{3.8}$: CO_2 Stability and Microstructure

Kaveh Partovi, Fangyi Liang, Olga Ravkina, and Jürgen Caro

Published in ACS Applied Materials & Interfaces **2014**, *6*, 10274-10282.

Reprinted with permission from ACS Applied Materials & Interfaces.
Copyright (2014) American Chemical Society.

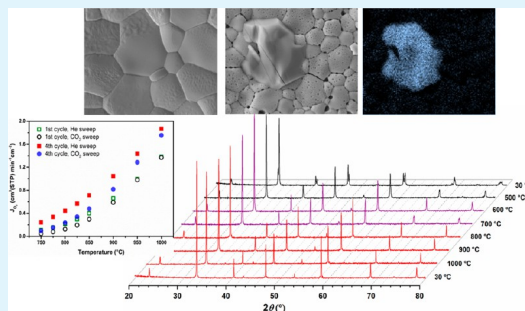
High-Flux Oxygen-Transporting Membrane $\text{Pr}_{0.6}\text{Sr}_{0.4}\text{Co}_{0.5}\text{Fe}_{0.5}\text{O}_{3-\delta}$: CO_2 Stability and Microstructure

Kaveh Partovi,* Fangyi Liang, Olga Ravkina, and Jürgen Caro

Institute of Physical Chemistry and Electrochemistry, Leibniz University Hannover, Callinstraße 3A, D-30167 Hannover, Germany

ABSTRACT: High oxygen permeability and good thermochemical stability of oxygen-transporting membranes (OTMs) are two main requirements concerning the applicability of these devices in chemical processes, such as CO_2 capture using the oxyfuel concept or catalytic membrane reactors. In this work, a single-phase perovskite-type membrane $\text{Pr}_{0.6}\text{Sr}_{0.4}\text{Co}_{0.5}\text{Fe}_{0.5}\text{O}_{3-\delta}$ (PSCF) with 0.6-mm thickness was subjected to periodic thermal cycling in the temperature range between 850 and 1000 °C in a 1000-h long-term permeation test with pure CO_2 as the sweep gas. The results of this long-term permeation operation revealed a stepwise increase in oxygen permeation values at 1000 °C after each thermal cycle, reaching from 1.38 cm^3 (STP) $\text{min}^{-1} \text{cm}^{-2}$ in the first cycle to 1.75 cm^3 (STP) $\text{min}^{-1} \text{cm}^{-2}$ in the fourth cycle. Furthermore, the membrane showed very good CO_2 stability at 900 °C and above. Despite a partial decrease in oxygen permeation fluxes at 850 °C, a steady state of 0.25 cm^3 (STP) $\text{min}^{-1} \text{cm}^{-2}$ was reached and maintained for more than 100 h. The newly developed PSCF membrane also exhibited a higher oxygen permeation flux with He and CO_2 sweeping at all measured temperatures compared to a similar $\text{La}_{0.6}\text{Sr}_{0.4}\text{Co}_{0.8}\text{Fe}_{0.2}\text{O}_{3-\delta}$ (LSCF) membrane.

KEYWORDS: CO_2 -stable membrane, perovskite, mixed conductor, oxygen permeation, long-term stability, phase transition



1. INTRODUCTION

Mixed ionic–electronic conducting (MIEC) ceramic oxides have gained considerable attention, because of their wide variety of potential applications as oxygen-transporting membranes (OTMs) in energy industries and petrochemical processes involving oxygen separation at high temperatures.¹ Some examples include utilization of OTMs as oxygen suppliers and distributors in processes such as oxidative coupling of methane to ethylene and ethane (OCM)^{2–4} and partial oxidation of methane (POM) to syngas ($\text{CO} + \text{H}_2$)^{5–7} or as cathode materials for solid oxide fuel cells (SOFCs).^{8,9} Furthermore, OTMs have recently received more attention as potential oxygen suppliers for CO_2 capture through an oxyfuel route in power plants.^{10–12}

Among perovskite-type mixed oxides, the highest values of oxygen permeation flux have been observed for the compositions containing alkaline-earth metal ions (especially Ba^{2+} and Sr^{2+}) on the A site of their ABO_3 structures.^{13,14} However, in the presence of notable concentrations of CO_2 on the feed or permeate side of the membrane, formation of a continuous layer of alkaline-earth carbonate on the membrane's surface hinders the oxygen exchange reaction, resulting in a dramatic drop of the oxygen flux to a negligible level.^{15–18} Therefore, the CO_2 tolerance of an OTM is of crucial importance for its applicability in chemical processes involving CO_2 , such as the oxyfuel concept.

One strategy to obtain CO_2 -stable membranes is to develop perovskite or perovskite-like materials completely free of alkaline-earth metals as single-phase or as mixed-matrix membranes. However, the oxygen permeability of these materials is very low for practical applications.^{12,19} Another approach is the enhancement of the membrane's CO_2 stability by partial substitution of the cations in the A and/or B sites with elements that are less reactive toward CO_2 , thus preserving the perovskite structure against carbonate formation at the cost of lower permeation levels. For example, it was reported that the CO_2 tolerance in $\text{SrCo}_{0.8}\text{Fe}_{0.2}\text{O}_{3-\delta}$ could be improved by replacing 10% of the cobalt and iron in the B site by tantalum²⁰ or titanium.²¹

Furthermore, the concept of replacing higher contents of alkaline-earth elements in the A site with rare-earth cations has been developed. Rare-earth cations are similar in size to alkaline-earth cations, but their carbonates decompose at lower temperatures.²² As an example, the A site of calcium- and strontium-containing perovskites was partially exchanged with the rare-earth element lanthanum.^{23,24} Evaluation of the collective data regarding the thermodynamic stabilities of carbonates under different CO_2 partial pressures, provided as an Ellingham diagram,²³ predicted a decomposition temper-

Received: March 20, 2014

Accepted: June 5, 2014

Published: June 5, 2014

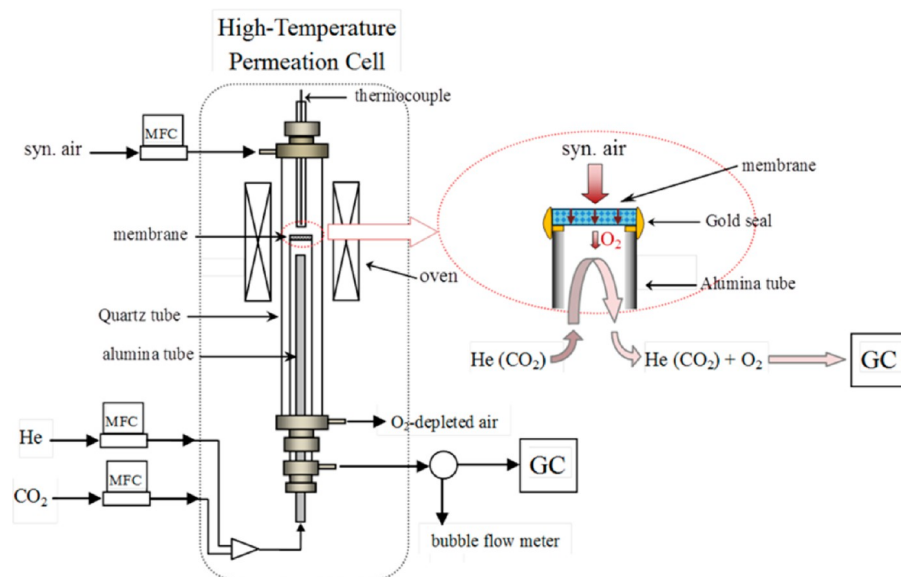


Figure 1. Schematic drawing of the experimental setup for oxygen permeation measurements.

ature of >1100 °C for pure SrCO₃ under an atmospheric pressure of CO₂. However, according to studies by Yokokawa et al.,²⁵ in the case of perovskite mixed oxides, the stabilization energy of the perovskite should also be taken into consideration. In other words, large negative stabilization energies of the perovskite oxide in Sr-containing perovskite structures result in higher stability against SrCO₃ formation. However, despite their acceptable tolerance in long-term oxygen permeation experiments under CO₂-containing atmospheres, the oxygen fluxes of these materials are relatively low, because of the higher-valence state of La³⁺ in comparison with Sr²⁺, which results in a lower concentration of oxygen vacancies. Furthermore, the smaller size of La³⁺(XII) ($r = 136$ pm)²⁶ compared to Sr²⁺(XII) ($r = 144$ pm)²⁶ results in reduced lattice parameters and, therefore, leads to a decreased oxygen flux. To compensate this deficit of low oxygen flux, surface-rich hollow fibers of La_{0.6}Sr_{0.4}Co_{0.8}Fe_{0.2}O_{3-δ} have been developed.²⁷

Perovskite-type strontium cobaltite with A-site Pr substitution (Pr_{0.6}Sr_{0.4}CoO_{3-δ}) was introduced by an early work of Teraoka et al.²⁸ In a more recent work, Serra et al. studied the system A_{0.68}Sr_{0.3}Fe_{0.8}Co_{0.2}O_{3-δ} (where A represents rare-earth metals and Ba) as cathode materials.²⁹ Also, in previous works by our group, we developed two dual-phase membranes containing perovskites with A-site Pr substitution as the mixed conducting phase, such as Ce_{0.9}Pr_{0.1}O_{2-δ}-Pr_{0.6}Sr_{0.4}FeO_{3-δ} (CP-PSF)³⁰ and Ce_{0.9}Pr_{0.1}O_{2-δ}-Pr_{0.6}Sr_{0.4}Fe_{0.5}Co_{0.5}O_{3-δ} (CP-PSFC),³¹ that show high oxygen permeability and good chemical stability in a CO₂ atmosphere at high temperatures. In this paper, we describe a new perovskite material, Pr_{0.6}Sr_{0.4}Co_{0.5}Fe_{0.5}O_{3-δ}, that shows a much higher oxygen flux in the presence of pure CO₂ than the perovskite-type oxygen-transporting materials published so far. Furthermore, the Pr_{0.6}Sr_{0.4}Co_{0.5}Fe_{0.5}O_{3-δ} material was carefully tested in long-term permeation operations with pure He or pure CO₂ as the sweep gas on the permeate side of the membrane.

2. EXPERIMENTAL SECTION

Synthesis and Membrane Preparation. A powder sample of Pr_{0.6}Sr_{0.4}Co_{0.5}Fe_{0.5}O_{3-δ} (abbreviated as PSFC) was synthesized by a conventional one-pot sol-gel ethylenediaminetetraacetic acid (EDTA)/citric acid complexing method by mixing proper ratios of the metal nitrates with a total metal cation/EDTA/citric acid ratio of 1:1:1.5, as described elsewhere.³² The as-synthesized powder was pressed into disks in a stainless steel module (18-mm i.d.) under a pressure of ~ 120 MPa that were then sintered at 1200 °C for 5 h in ambient air with heating/cooling rates of 2 °C min⁻¹ to obtain disk membranes (approximately 0.6-mm thickness and 16-mm i.d.). The sintering time for the 1-mm-thick membrane was increased to 10 h under the same conditions.

X-ray Diffraction. The structural properties of the membranes were analyzed using X-ray diffraction (XRD) techniques. The data set was acquired at room temperature and in ambient air on a Bruker-AXS D8 Advance instrument with Cu K α radiation in the step-scan mode within a 2θ range of 20–80° at 0.02° intervals. In situ XRD measurements between 30 and 1000 °C were conducted in an in situ cell HTK-1200 N (Anton-Paar) in an atmosphere consisting of 100 vol % CO₂ with a heating rate of 12 °C min⁻¹ and an equilibrium time of 30 min prior to each measurement. The XRD data were analyzed using TOPAS 4.2 software (Bruker AXS).

Oxygen Permeation. The oxygen permeation flux was measured using a high-temperature permeation device schematically depicted in Figure 1. Freshly sintered disk membranes were sealed with gold paste (conducting paste CS754, Heraeus, Hanau, Germany) onto an alumina tube and positioned at the center of a vertical tubular oven. Synthetic air (20 vol % O₂/80 vol % N₂) at a flow of 150 cm³ (STP) min⁻¹ was applied to one side of the membrane, and the permeate side of the membrane was alternately swept with 50 cm³ (STP) min⁻¹ of He (Linde, 99.999%) and CO₂ (Linde, 99.5%). Mass flow controllers (MFCs) (Bronkhorst, Ruurlo, The Netherlands) were applied for all inlet gases, and the total effluent flow rate was measured with a soap-film flow meter. The quantitative analysis of the effluent mixture was performed using an online-coupled gas chromatograph (Agilent 6890A). Gas leakage through possible flaws in the sealing could be detected by monitoring the N₂ concentration in the effluent. The O₂ leakage could then be calculated and subtracted from the total O₂ flux.

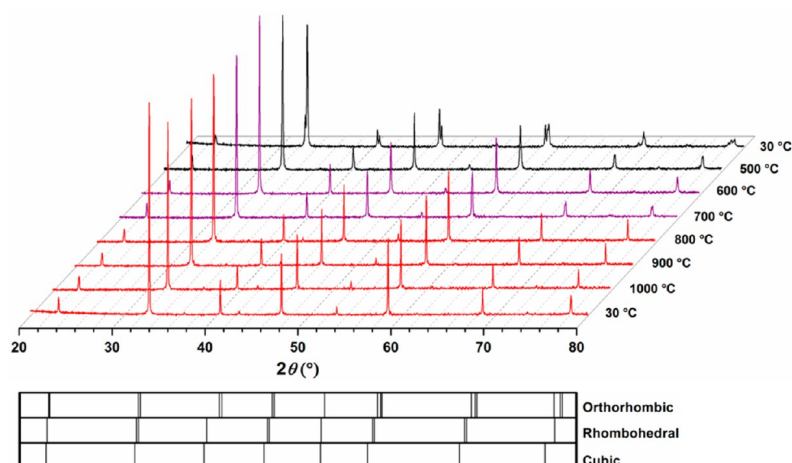


Figure 2. In situ XRD patterns of PSCF powder in an atmosphere of 100 vol % CO_2 at the given temperatures with the reflex positions of orthorhombic, rhombohedral, and cubic perovskite structures.

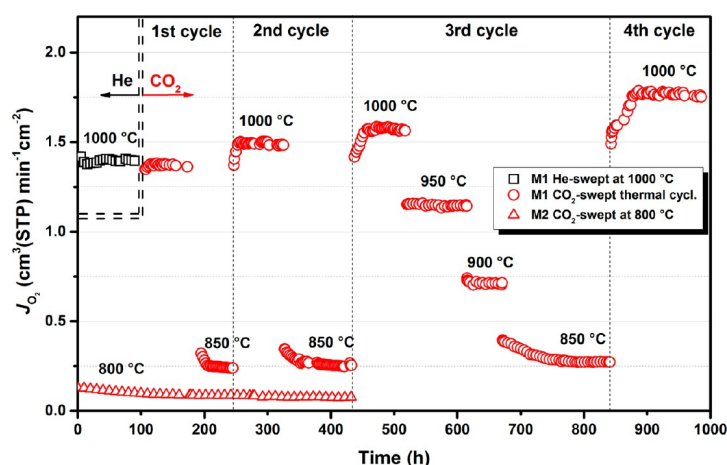


Figure 3. Oxygen permeation flux through PSCF disk membrane M1 with thermal cycling between 850 and 1000 °C and M2 at 800 °C. Sweep side M1: $50 \text{ cm}^3 \text{ (STP) min}^{-1}$ He (black squares)/ CO_2 (red circles). Sweep side M2: $50 \text{ cm}^3 \text{ (STP) min}^{-1}$ CO_2 (red triangles). Feed side M1 and M2: $150 \text{ cm}^3 \text{ (STP) min}^{-1}$ synthetic air. Membrane thickness: 0.6 mm.

The initial oxygen permeation measurements on a 0.6-mm-thick PSCF membrane M1 were conducted with He as the sweep gas at 1000 °C. After a constant oxygen permeation flux was reached, the permeation fluxes were measured at varying temperatures in the following order: 1000, 950, 900, 850, and 800 °C. The measurements were continued for 100 h at 1000 °C, during which a constant permeation flux was maintained. The sweep gas was then switched to CO_2 , and measurements were continued for 1000 h, during which the membrane was subjected to four thermal cycles as described in the next subsection. The heating/cooling rate was $2 \text{ }^\circ\text{C min}^{-1}$ for all temperature variations.

Thermal Cycling with CO_2 as the Sweep Gas. At 1000 °C, the system reached and maintained a constant oxygen flux after 80 h. The temperature was then lowered to 850 °C, and the oxygen flux was further measured. After 50 h at 850 °C with a stable oxygen flux, the second thermal cycle was started by ramping the temperature to 1000 °C. As in the first thermal cycle, the temperature was again lowered to 850 °C after a constant permeation level had been held for more than 100 h. Further oxygen permeation measurements were conducted for

the third and fourth thermal cycles. After the oxygen flux had been measured at different temperatures (1000–800 °C) during the fourth thermal cycle, the temperature was again adjusted to 1000 °C, and the sweep gas was switched back to He. The oxygen permeation was then measured again at temperatures ranging from 1000 to 800 °C with He as the sweep gas.

Further long-term oxygen permeation measurements were conducted on 0.6-mm-thick PSCF membrane M2 at 800 °C with CO_2 sweeping for 450 h.

Scanning Electron Microscopy (SEM). The microstructures and surface morphologies of the membranes before and after the oxygen permeation measurements were studied using a field-emission scanning electron microscope of the type JEOL JSM-6700F at an excitation voltage of 2 kV. Energy-dispersive X-ray spectroscopy (EDXS) was employed using an Oxford Instruments INCA A-300 spectrometer at an excitation voltage of 20 kV to study the elemental distributions on the membrane's surface and within the grains.

3. RESULTS AND DISCUSSION

CO₂ Stability by in Situ XRD. The phase stability of PSCF was investigated using high-temperature in situ XRD measurements conducted on a powder sample in an atmosphere of 100 vol % CO₂ (Figure 2). An orthorhombic perovskite structure [space group *Imma* (No. 74)] exists at room temperature. Between 500 and 600 °C, a phase transition from orthorhombic to rhombohedral symmetry [space group *R $\bar{3}c$* (No. 167)] occurs. The system undergoes a second phase transition to cubic perovskite symmetry [space group *Pm $\bar{3}m$* (No. 221)] at 700–800 °C. It should be noted that, in an oxygen-free atmosphere, the cubic structure is maintained after the sample has been cooled to room temperature (Figure 2). However, during another in situ XRD measurement in an atmosphere of 50% CO₂ and 50% synthetic air, the initial orthorhombic symmetry was observed after the sample had been cooled to room temperature as a result of a declining oxygen vacancy concentration with decreasing temperature in an oxygen-containing atmosphere. The possible formation of SrCO₃ could not be confirmed from the in situ XRD results.

Oxygen Permeation. To investigate the membranes' CO₂ stability, long-term oxygen permeation measurements were conducted on two 0.6-mm-thick PSCF membranes with pure He (black squares) or pure CO₂ (red circles and triangles) as the sweep gas at different temperatures, as shown in Figure 3. Membrane M1 was stressed by rigorous thermal cycling, and the oxygen permeation flux was measured for both He and CO₂ as the sweep gases in the temperature range between 850 and 1000 °C. During the initial measurements at 1000 °C with He as the sweep gas, the PSCF membrane maintained a stable oxygen permeation flux of $\sim 1.38 \text{ cm}^3 \text{ (STP) min}^{-1} \text{ cm}^{-2}$ for 100 h. Then, CO₂ was used as the sweep gas for the thermal cycling instead of He. During the first thermal cycle at 1000 °C, no significant decrease in permeation values was observed, and a constant permeation flux of $1.37 \text{ cm}^3 \text{ (STP) min}^{-1} \text{ cm}^{-2}$ was measured for 80 h. Then, the temperature was gradually decreased from 1000 to 850 °C. At 850 °C, after a slow decrease in the oxygen permeation flux in the first 20 h, a steady state was reached, and a stable value of $0.25 \text{ cm}^3 \text{ (STP) min}^{-1} \text{ cm}^{-2}$ was maintained for more than 50 h. This observation of a state with slowly decreasing fluxes followed by a steady state was also repeated in the following cycles (second and third cycles) at 850 °C. Moreover, from the first cycle to the third cycle, the duration of the state with decreasing fluxes increased from ca. 20 to ca. 100 h, and the oxygen permeation flux increased slightly from 0.25 to $0.27 \text{ cm}^3 \text{ (STP) min}^{-1} \text{ cm}^{-2}$. After the temperature had been increased from 850 to 1000 °C in the second, third, and fourth cycles, at the constant temperature of 1000 °C, a state of increasing fluxes and a steady state were clearly observed for each cycle. With increasing number of cycles, the duration of the state with increasing fluxes increased from ca. 10 to ca. 50 h, and the oxygen permeation flux increased clearly from 1.37 to $1.78 \text{ cm}^3 \text{ (STP) min}^{-1} \text{ cm}^{-2}$. The observation of a state of decreasing fluxes at 850 °C and a state of increasing fluxes at 1000 °C can be explained by carbonate formation at the grain boundaries at the lower temperature of 850 °C, followed by thermal decomposition at the higher temperature of 1000 °C, resulting in increased porosity of the membrane's surface on the CO₂-swept side, as shown in Figures 6 and 7. In addition to an increased surface area, the effect of a locally reduced membrane thickness due to grain depletion should not be overlooked. The

observed holes varied in dimensions and were not uniformly distributed on the membrane surface, making it difficult to exactly determine the effect of the membrane's reduced thickness on the permeation flux. However, the observed depth of the local holes varied between 100 and 150 μm , which is obviously not sufficient to increase the permeation fluxes from 1.37 to $1.78 \text{ cm}^3 \text{ (STP) min}^{-1} \text{ cm}^{-2}$. Therefore, it can be concluded that the higher membrane surface area is the crucial factor for the increased oxygen permeation flux. The increased porosity of the membrane's surface on the CO₂-swept side can also explain the fact that, after each cycle, the system needed more time to achieve a steady state of oxygen permeation flux because increasing the membrane's surface area led to the formation of more carbonate and the higher amount of formed carbonate required a longer decomposition time at 1000 °C. It should be noted that the oxygen permeation flux maintained constant values of 0.74 and $1.18 \text{ cm}^3 \text{ (STP) min}^{-1} \text{ cm}^{-2}$ during the whole time at 900 and 950 °C, respectively. It can be expected that the formation of carbonate on the PSCF membrane surface would not take place at 900 °C and above. It should also be considered that, according to the previously discussed in situ XRD results, no phase transitions were expected to occur in the temperature range of 850–1000 °C used for the thermal cycling and the perovskite-type cubic symmetry (*Pm $\bar{3}m$*) was maintained during each cycle. Possible phase transitions could have resulted in mechanical stresses across the membrane, thus leading to fractures and crack formation. The absence of cracks was verified by monitoring the concentration of N₂ in the effluent, which remained insignificant during the entire experiment.

Moreover, to investigate carbonate formation at lower temperatures, additional long-term oxygen permeation measurements were conducted on PSCF membrane M2 at 800 °C with pure CO₂ as the sweep gas. After the initial fast decrease of the oxygen permeation flux from 0.12 to $0.08 \text{ cm}^3 \text{ (STP) min}^{-1} \text{ cm}^{-2}$ in the first 150 h at 800 °C, the oxygen permeation flux gradually reached a steady state after 300 h. This initial decrease of the oxygen concentration could be indicative of the local formation of SrCO₃ on the membrane's surface on the CO₂-swept side, which was further explored using SEM and EDX spectroscopy (Figures 5–11). The rate of SrCO₃ formation on the membrane surface is dependent on the concentration of Sr²⁺ on the membrane's surface layer, which decreases with the operation time at 800 °C. As a result, a steady state can be observed as the carbonate formation reaction ($\text{Sr}^{2+} + \text{CO}_3^{2-} \rightleftharpoons \text{SrCO}_3$) is limited by very low amounts of Sr²⁺ on the membrane's surface layer.

Structure Characterization and Phase Stability. For the characterization of the PSCF membrane after long-term oxygen permeation measurements with 100 vol % CO₂ exposure on the sweep side at 1000 °C, X-ray diffraction (XRD) was applied on both feed and sweep sides of the spent membrane. The resulting XRD patterns measured at room temperature (Figure 4) indicate that the orthorhombic body-centered perovskite structure [space group *Imma* (No. 74)] of the freshly sintered PSCF membrane was maintained after the long-term oxygen permeation measurements with CO₂ as the sweep gas. No carbonate formation was evidenced, despite the fact that the A site of PSCF contains 40% alkaline-earth metal ion Sr²⁺ because the carbonate formed at the lower temperature of 850 °C was decomposed at the higher temperature of 1000 °C, before the sample was cooled to room temperature.

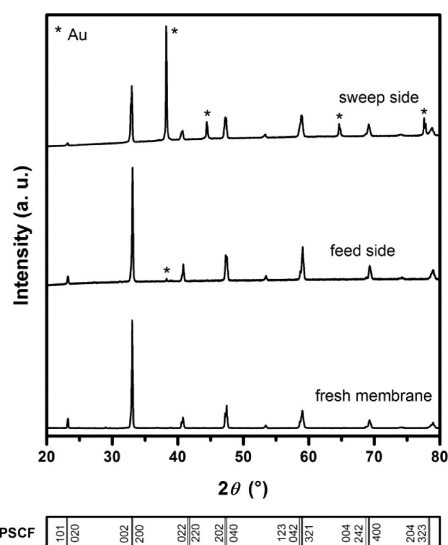


Figure 4. Room-temperature XRD patterns of freshly sintered PSCF membrane M1 (bottom), feed side of the spent membrane (middle), and sweep side of the membrane after 900 h of CO₂ exposure and 1000 h of long-term oxygen permeation operation (top). The reflex positions pertaining to gold from the sealing paste are marked with asterisks (*).

Microstructure and Elemental Analysis. The surface microstructure of the PSCF membranes before and after the long-term measurements with CO₂ sweeping was studied by SEM, as shown in Figures 5–7. The elemental distribution was

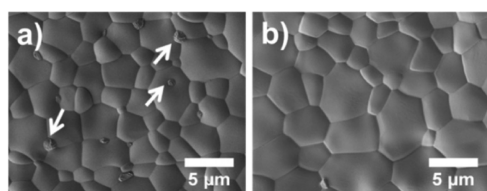


Figure 5. SEM micrographs of the PSCF membrane: (a) fresh membrane (cobalt oxide particles are marked with white arrows), (b) feed side of PSCF membrane M1 after long-term oxygen permeation operation with thermal cycling between 850 and 1000 °C.

studied by EDXS. The SEM micrographs of the fresh PSCF membrane show densely packed grains and a crack-free membrane surface (Figure 5a). However, some small particles could frequently be observed on the surface, which were found to be Co-rich particles (most probably cobalt oxide) using EDXS mapping. This observation of Co-rich particles was also found on the fresh La_{0.6}Sr_{0.4}Co_{0.8}Fe_{0.2}O_{3-δ} (LSCF) membrane by Klande et al.²⁴ Nonetheless, the elemental distribution throughout the membrane's surface and within the grains was homogeneous. After the long-term measurements for 1000 h, SEM micrographs of the feed/air side of PSCF membrane M1 showed no deterioration of the microstructure, and the Co-rich particles almost disappeared from the surface (Figure 5b). However, SEM micrographs of the membrane's cross section (Figure 6a) revealed a high occurrence of the local disintegration of grains on the sweep side of the membrane,

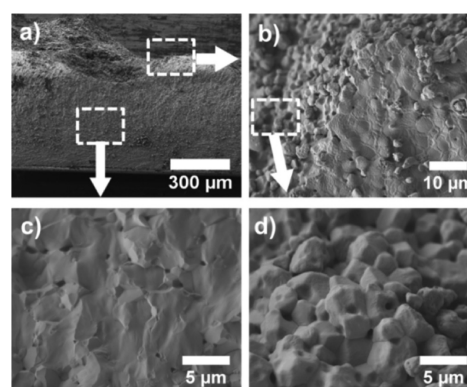


Figure 6. SEM micrographs of PSCF membrane M1 after long-term oxygen permeation operation with thermal cycling between 850 and 1000 °C: (a) membrane cross section, (b) formation of a flat hole as grains disintegrate from the permeate side, (c) cross section of the unchanged part in the middle of the membrane with densely packed grains and some closed porosity (black pinholes), (d) microstructure of the surface of the flat hole showing disintegrated grains.

which led to formation of several spots with alternating grain depletion (Figure 6b,d) and grain accumulation (Figure 7).

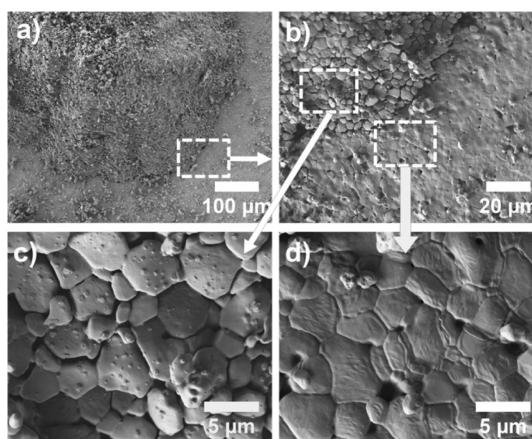


Figure 7. SEM micrographs of the permeate side of PSCF membrane M1 after long-term oxygen permeation operation with thermal cycling between 850 and 1000 °C: (a,b) local disintegration of the grains with different magnifications, (c) microstructure of the disintegrated grains, (d) unchanged part of the membrane with densely packed grains and some closed porosity (black pinholes).

This phenomenon could be caused by several thermal cycles with CO₂ sweeping. Long dwell times at 850 °C and below in the presence of 100 vol % CO₂ could have resulted in the formation of carbonates in the grain boundaries. The subsequent temperature rise at the end of each cycle should have then caused the decomposition of the formed carbonates, followed by the release of gaseous CO₂ from the grain boundaries, resulting in the local disintegration of grains from the membrane's surface and the formation of hills/valleys. The observation of the local accumulation of grains in the form of hills on the sweep side of the membrane was difficult to explain.

However, it is plausible that a mechanism similar to the primary nucleation stage during crystallization could be responsible for this phenomenon. Furthermore, no additional alteration of the microstructure could be detected in the inner depths of PSCF membrane M1 (Figure 6c). The formation of carbonates could not be verified by the in situ XRD results under pure CO₂ atmosphere at temperatures below 850 °C, which might be because the amount of the carbonate formed in the short dwell time was lower than the detection limit of the XRD instrument.

PSCF Membrane after 450 h of CO₂ Sweeping at 800 °C (M2). To investigate the CO₂ tolerance of the PSCF membrane at lower temperatures, a long-term oxygen permeation test was conducted on a PSCF membrane at 800 °C for 450 h of CO₂ sweeping, followed by SEM, EDXS, and XRD analyses. The SEM micrographs and the related elemental EDXS mappings of the sweep side and of the membrane's cross section close to the sweep side are depicted in Figures 8 and 9,

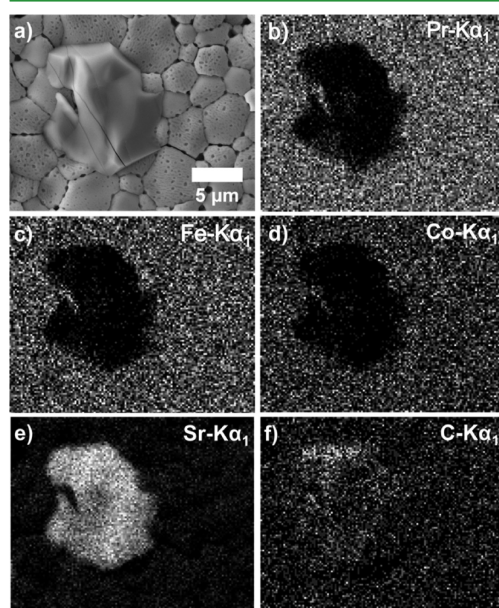


Figure 8. (a) SEM micrograph of the sweep side of PSCF membrane M2 after 450 h of CO₂ sweeping at 800 °C, (b–f) elemental distributions by EDXS of the area shown in panel a.

respectively. As expected, no alteration of the microstructure was observed on the feed side of the membrane. However, SEM imaging of the CO₂-swept permeate side revealed several spots where local formation of a second phase had occurred on top of the membrane's surface. Furthermore, numerous pores were formed at the grain boundaries, frequently resulting in dislocation of the grains. The EDXS analysis of the membrane's surface indicated that the extra phase was rich in Sr and C, as shown in Figure 8e,f. A closer inspection of the Sr distribution depicted in Figure 8e confirms the relative Sr depletion from the grain boundaries. However, no interconnecting cracks were observed, which was also in accordance with the absence of N₂ leakage in the gas chromatographs. The EDXS mapping of the membrane's cross section shows that the Sr-rich layer was

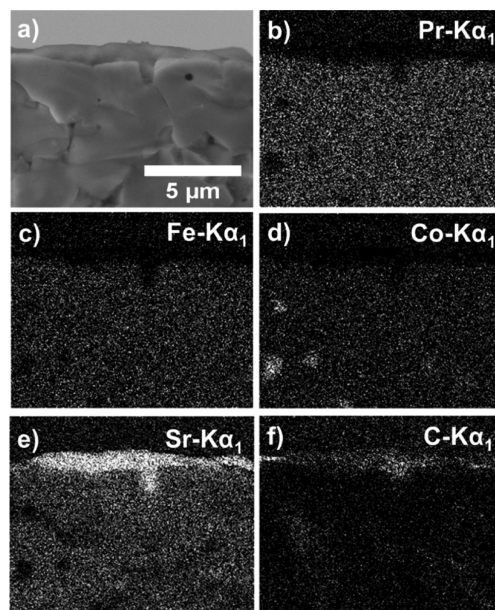


Figure 9. (a) SEM micrograph of PSCF membrane M2 cross section close to the permeate side after 450 h of CO₂ sweeping at 800 °C, (b–f) elemental distributions by EDXS of the area shown in panel a.

approximately 1–2 μm thick (Figure 9a). The formation of carbonates at 800 °C resulted in a decline in the oxygen permeation flux in the long run. However, it can be observed from Figure 3 that, after 150 h of slowly decreasing fluxes, a steady state was reached for at least 300 h. The existence of a micrometer-thick continuous carbonate layer was previously observed by Arnold et al.¹⁷ and Klande et al.²⁴ In the case of the PSCF membrane, several isolated patches of SrCO₃ were formed on the membrane's surface. Furthermore, several Co-rich spots were detected, which were most probably cobalt oxide particles. The remaining elements, namely, Pr, Sr, and Fe, were homogeneously distributed. The presence of SrCO₃ could also be verified by the subsequent XRD measurements at room temperature on the spent PSCF M2 membrane (Figure 10).

PSCF Membrane after 300 h of CO₂ Sweeping at 950 °C (M3). To investigate the effect of CO₂ on the microstructure of the PSCF membrane, an additional test on PSCF membrane M3 was performed using CO₂ as the sweep gas at 950 °C for 300 h. After this test, the microstructure of the surface of the PSCF membrane M3 on the sweep side was characterized by SEM, and room-temperature XRD measurements were conducted to investigate the carbonate formation on the surface. The XRD patterns of PSCF membranes M2 and M3 and the corresponding SEM micrographs of their CO₂-swept sides are depicted in Figure 10. Although the formation of small amounts of carbonate on membrane M2 (after long-term CO₂ sweeping at 800 °C) is obvious, no carbonate formation on the M3 membrane surface was observed. In addition, no local disintegration of grains on the membrane surface on the sweep side of membrane M3 was observed in the SEM micrograph. In addition, the SEM micrograph of membrane M2 clearly exhibits pore formation at the grain boundaries due to strontium

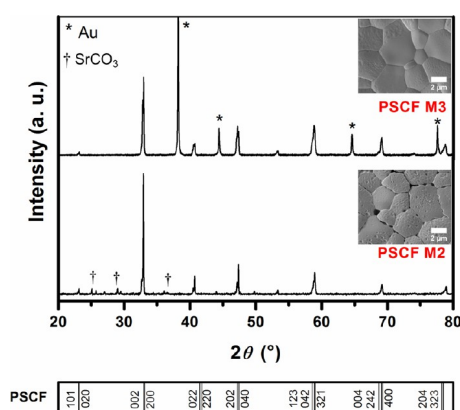


Figure 10. Top: Room-temperature XRD patterns of spent PSCF membranes M2 and M3 after long-term oxygen permeation operation with related SEM images. The reflex positions of gold from the gold paste and the formed SrCO_3 are marked with asterisks (*) and daggers (†), respectively.

depletion, as was previously confirmed by EDXS analysis (Figure 8). The EDX mapping of the elements on the sweep side of membrane M3 also confirms a homogeneous elemental distribution and no detectable carbonate formation. By combining the results of the long-term operation of PSCF membrane M1 at 900 °C with constant fluxes during the third thermal cycle and no carbonate formation on the surface of PSCF membrane M3 at 950 °C, it can be deduced that the PSCF membrane exhibits an excellent stability in CO_2 at 900 °C and above.

Comparison of the Oxygen Permeabilities of PSCF and LSCF Membranes. The comparative results of oxygen permeation measurements conducted on the 1-mm-thick PSCF membrane and the previously reported $\text{La}_{0.6}\text{Sr}_{0.4}\text{Co}_{0.8}\text{Fe}_{0.2}\text{O}_{3-\delta}$ (LSCF)²⁴ membrane with the same thickness are shown in Figure 11. As can be seen, our PSCF perovskite membrane provided higher permeation fluxes than the LSCF perovskite membrane, which also had 40% Sr on the A site. For instance, at 950 °C, the PSCF membrane exhibited an oxygen permeation flux of $0.54 \text{ cm}^3 (\text{STP}) \text{ min}^{-1} \text{ cm}^{-2}$, which was slightly higher than the $0.30 \text{ cm}^3 (\text{STP}) \text{ min}^{-1} \text{ cm}^{-2}$ value measured on the LSCF membrane with the same sweep gas (He). It should be noted that, at a lower temperature of 850 °C, the PSCF membrane had a higher permeation flux in an air/ CO_2 oxygen gradient in comparison to the LSCF membrane in an air/He oxygen gradient. Nevertheless, in terms of CO_2 stability, the LSCF membrane also exhibited a good tolerance in CO_2 atmosphere after more than 200 h of operation at 900 °C,²⁴ which was similar to the tolerance of our PSCF membrane.

It is expected from the ionic radii of Pr^{3+} (132 pm) and La^{3+} (136 pm)²⁶ that replacing Sr^{2+} (144 pm) with Pr should result in a smaller unit cell than replacing Sr^{2+} with La. Nevertheless, the data analysis of the in situ XRD measurements shows a negligible difference in lattice parameters of the cubic perovskite structures at 1000 °C, with 39.3 and 39.4 pm for PSCF and LSCF, respectively.²⁴ However, from a steric point of view, doping the A site with a smaller rare-earth cation could increase the oxygen-ion mobility in the cubic perovskite lattice, which is in accordance with the geometric calculations of Kilner

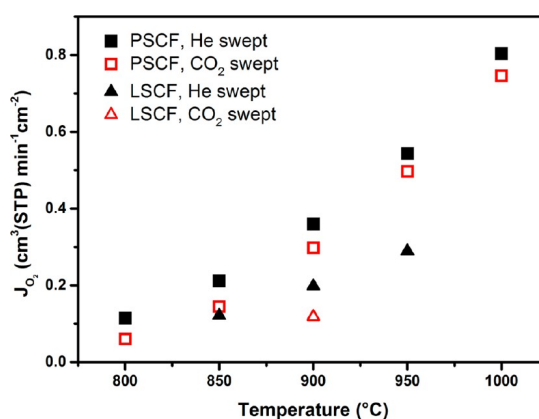
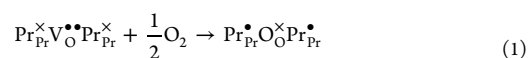


Figure 11. Temperature-dependent oxygen permeation fluxes of 1-mm-thick PSCF (square) and LSCF (triangle) disk membranes. Feed side: $150 \text{ cm}^3 (\text{STP}) \text{ min}^{-1}$ of synthetic air. Sweep side for PSCF: $50 \text{ cm}^3 (\text{STP}) \text{ min}^{-1}$ flow rate of He (solid) and CO_2 (open). The oxygen partial pressure gradient $[\ln(P_{\text{O}_2, \text{feed}}/P_{\text{O}_2, \text{permeate}})]$ across the PSCF membrane at 950 °C was 2.894 with He as the sweep gas. Sweep side for LSCF: $30 \text{ cm}^3 (\text{STP}) \text{ min}^{-1}$ flow of He (solid) and CO_2 (open). The oxygen partial pressure gradient across the LSCF membrane at 950 °C was 2.996 with He as the sweep gas.²⁴

and Brook on LnAlO_3 systems (Ln = lanthanides), predicting a slight decrease in the oxygen migration enthalpies with decreasing dopant (here, rare-earth metal) ionic radius, for a fixed B-site composition.³³ In the comparative case of LSCF and PSCF, both materials contain 40 at. % Sr at the A site of the perovskite. However, the smaller ionic radius of Pr compared to La could facilitate oxygen-ion migration through the saddle-point configuration (the triangle of two A-site and one B-site cations), according to various studies.^{28,33,34} Furthermore, it should be noted that Pr can simultaneously exist in the two valence states of Pr^{3+} and Pr^{4+} in its oxide form,³⁵ whereas La^{3+} , with the highest fourth ionization energy among lanthanides and the xenon noble-gas electron configuration, maintains its trivalent oxidation state.³⁶ The concurrence of different valence states of Pr^{3+} and Pr^{4+} could also be beneficial to the dissociation and reduction of molecular oxygen on the membrane's surface. Furthermore, Ishihara et al. reported high dissociation rates of molecular oxygen into ionic oxygen, which might be related to the facile redox cycle of $\text{Pr}^{4+}/\text{Pr}^{3+}$ in $\text{Pr}_{0.6}\text{Sr}_{0.4}\text{MnO}_3$,³⁷ thus contributing to faster surface-exchange kinetics, when considering the dissociation of molecular oxygen at a Pr-terminated surface as in the following reaction using Kröger–Vink notation



where $\text{Pr}_{\text{Pr}}^{\times}$ and $\text{Pr}_{\text{Pr}}^{\bullet}$ are Pr^{3+} and Pr^{4+} , respectively, and $\text{V}_{\text{O}}^{\bullet}$ is an oxygen vacancy.

4. CONCLUSIONS

The perovskite-type mixed-oxide conductor $\text{Pr}_{0.6}\text{Sr}_{0.4}\text{Co}_{0.5}\text{Fe}_{0.5}\text{O}_{3-\delta}$ was successfully prepared by a conventional sol–gel citric acid/EDTA complexing method. In situ XRD measurements revealed a structure transition from orthorhombic perovskite symmetry to rhombohedral symmetry at 500–600 °C and a second phase transition from

rhombohedral to cubic at 700–800 °C. In comparison with the extensively studied $\text{La}_{0.6}\text{Sr}_{0.4}\text{Co}_{0.8}\text{Fe}_{0.2}\text{O}_{3-\delta}$ (LSCF) materials under similar conditions, the PSCF membrane shows higher permeation fluxes because of the smaller ionic radius of the Pr^{3+} cation, which can decrease the potential energy barrier of oxygen migration. The fact that Pr can simultaneously exist in two valence states, Pr^{3+} and Pr^{4+} , not only could facilitate oxygen migration in the lattice from a steric perspective, but also could enhance the dissociation rate of molecular oxygen into ionic oxygen. A series of long-term oxygen permeation studies and chemical stability tests conducted on PSCF membranes showed that the PSCF membrane exhibits an excellent CO_2 tolerance and a high oxygen permeation performance at 900 °C and above, which suggests that PSCF can be considered as a promising candidate for applications in chemical processes involving the oxyfuel concept for CO_2 capture in this temperature range.

AUTHOR INFORMATION

Corresponding Author

*E-mail: kaveh.partovi@pci.uni-hannover.de. Tel.: +49-511-762-2125. Fax: +49-511-762-3175.

Notes

The authors declare no competing financial interest.

ACKNOWLEDGMENTS

The authors gratefully acknowledge financial support from the Sino-German Centre for Research Promotion (GZ676 and GZ911).

REFERENCES

- (1) Dyer, P. N.; Richards, R. E.; Russek, S. L.; Taylor, D. M. Ion Transport Membrane Technology for Oxygen Separation and Syngas Production. *Solid State Ionics* **2000**, *134*, 21–33.
- (2) Liang, F. Y.; Caro, J. Perovskite Membranes for High Temperature Oxygen Separation. In *Membrane Engineering for the Treatment of Gases*; Drioli, E., Barbieri, G., Eds.; Royal Society of Chemistry: London, 2011; Vol. 2, pp 192–221.
- (3) Lin, Y. S.; Zeng, Y. Catalytic Properties of Oxygen Semi-permeable Perovskite-Type Ceramic Membrane Materials for Oxidative Coupling of Methane. *J. Catal.* **1996**, *164*, 220–231.
- (4) Jiang, H. Q.; Cao, Z. W.; Schirmer, S.; Schiestel, T.; Caro, J. A Coupling Strategy to Produce Hydrogen and Ethylene in a Membrane Reactor. *Angew. Chem., Int. Ed.* **2010**, *49*, S656–S660.
- (5) Caro, J.; Caspary, K. J.; Hamel, C.; Hoting, B.; Koelsch, P.; Langanke, B.; Nassauer, K.; Schiestel, T.; Schmidt, A.; Schomaeker, R.; Seidel-Morgenstern, A.; Tsotsas, E.; Voigt, L.; Wang, H.; Warsitz, R.; Werth, S.; Wolf, A. Catalytic Membrane Reactors for Partial Oxidation Using Perovskite Hollow Fiber Membranes and for Partial Hydrogenation Using a Catalytic Membrane Contactor. *Ind. Eng. Chem. Res.* **2007**, *46*, 2286–2294.
- (6) Jiang, H. Q.; Wang, H. H.; Liang, F. Y.; Werth, S.; Schiestel, T.; Caro, J. Direct Decomposition of Nitrous Oxide to Nitrogen by in Situ Oxygen Removal with a Perovskite Membrane. *Angew. Chem., Int. Ed.* **2009**, *48*, 2983–2986.
- (7) Balachandran, U.; Dusek, J. T.; Mievile, R. L.; Poeppel, R. B.; Kleefisch, M. S.; Pei, S.; Kobylinski, T. P.; Udovich, C. A.; Bose, A. C. Dense Ceramic Membranes for Partial Oxidation of Methane to Syngas. *Appl. Catal. A* **1995**, *133*, 19–29.
- (8) Shao, Z. P.; Haile, S. M. A High-Performance Cathode for the Next Generation of Solid-Oxide Fuel Cells. *Nature* **2004**, *431*, 170–173.
- (9) Huang, K.; Wan, J.; Goodenough, J. B. Oxide-Ion Conducting Ceramics for Solid Oxide Fuel Cells. *J. Mater. Sci.* **2001**, *36*, 1093–1098.
- (10) Liang, F. Y.; Luo, H. X.; Partovi, K.; Ravkina, O.; Cao, Z. W.; Liu, Y.; Caro, J. A Novel CO_2 -Stable Dual Phase Membrane with High Oxygen Permeability. *Chem. Commun.* **2014**, *50*, 2451–2454.
- (11) Luo, H. X.; Efimov, K.; Jiang, H. Q.; Feldhoff, A.; Wang, H. H.; Caro, J. CO_2 -Stable and Cobalt-Free Dual-Phase Membrane for Oxygen Separation. *Angew. Chem., Int. Ed.* **2011**, *50*, 759–763.
- (12) Zhu, X.; Liu, H.; Cong, Y.; Yang, W. Novel Dual-Phase Membranes for CO_2 Capture via an Oxyfuel Route. *Chem. Commun.* **2012**, *48*, 251–253.
- (13) Bouwmeester, H. J. M.; Burggraaf, A. J. Dense Ceramic Membranes for Oxygen Separation. In *Fundamentals of Inorganic Membrane Science and Technology*; Burggraaf, A. J.; Cot, L., Eds.; Elsevier Science B. V.: Amsterdam, The Netherlands, 1996; Vol. 4, Chapter 10, pp 435–528.
- (14) Efimov, K.; Arnold, M.; Martynczuk, J.; Feldhoff, A. Crystalline Intermediate Phases in the Sol-Gel-Based Synthesis of $\text{La}_2\text{NiO}_{4+\delta}$. *J. Am. Ceram. Soc.* **2009**, *92*, 876–880.
- (15) Liang, F. Y.; Jiang, H. Q.; Luo, H. X.; Caro, J.; Feldhoff, A. Phase Stability and Permeation Behavior of a Dead-End $\text{Ba}_{0.5}\text{Sr}_{0.5}\text{Co}_{0.8}\text{Fe}_{0.2}\text{O}_{3-\delta}$. *Chem. Mater.* **2011**, *23*, 4765–4772.
- (16) ten Elshof, J. E.; Bouwmeester, H. J. M.; Verweij, H. Oxygen Transport through $\text{La}_{1-x}\text{Sr}_x\text{FeO}_{3-\delta}$. *Solid State Ionics* **1996**, *89*, 81–92.
- (17) Arnold, M.; Wang, H.; Feldhoff, A. Influence of CO_2 on the Oxygen Permeation Performance and the Microstructure of Perovskite-Type ($\text{Ba}_{0.5}\text{Sr}_{0.5}$)($\text{Co}_{0.8}\text{Fe}_{0.2}$) $\text{O}_{3-\delta}$. *J. Membr. Sci.* **2007**, *293*, 44–52.
- (18) Czuprat, O.; Arnold, M.; Schirmer, S.; Schiestel, T.; Caro, J. Influence of CO_2 on the Oxygen Permeation Performance of Perovskite-Type $\text{BaCo}_x\text{Fe}_y\text{Zr}_z\text{O}_{3-\delta}$. *J. Membr. Sci.* **2010**, *364*, 132–137.
- (19) Kharton, V. V.; Kovalevsky, A. V.; Viskup, A. P.; Figueiredo, F. M.; Yaremchenko, A. A.; Naumovich, E. N.; Marques, F. M. B. Oxygen Permeability of $\text{Ce}_{0.8}\text{Gd}_{0.2}\text{O}_{2-\delta}$ - $\text{La}_{0.7}\text{Sr}_{0.3}\text{MnO}_{3-\delta}$ Composite Membranes. *J. Electrochem. Soc.* **2000**, *147*, 2814–2821.
- (20) Chen, W.; Chen, C.; Winnubst, L. Ta-Doped $\text{SrCo}_{0.8}\text{Fe}_{0.2}\text{O}_{3-\delta}$ Membranes: Phase Stability and Oxygen Permeation in CO_2 Atmosphere. *Solid State Ionics* **2011**, *196*, 30–33.
- (21) Zeng, Q.; Zuo, Y.; Fan, C.; Chen, C. CO_2 -Tolerant Oxygen Separation Membranes Targeting CO_2 Capture Application. *J. Membr. Sci.* **2009**, *335*, 140–144.
- (22) Sunarso, J.; Baumann, S.; Serra, J. M.; Meulenberg, W. A.; Liu, S.; Lin, Y. S.; da Costa, J. C. D. Mixed Ionic-Electronic Conducting (MIEC) Ceramic-Based Membranes for Oxygen Separation. *J. Membr. Sci.* **2008**, *320*, 13–41.
- (23) Efimov, K.; Klande, T.; Juditzki, N.; Feldhoff, A. Ca-Containing CO_2 -Tolerant Perovskite Materials for Oxygen Separation. *J. Membr. Sci.* **2012**, *389*, 205–215.
- (24) Klande, T.; Ravkina, O.; Feldhoff, A. Effect of A-Site Lanthanum Doping on the CO_2 Tolerance of $\text{SrCo}_{0.8}\text{Fe}_{0.2}\text{O}_{3-\delta}$ Oxygen-Transporting Membranes. *J. Membr. Sci.* **2013**, *437*, 122–130.
- (25) Yokokawa, H.; Sakai, N.; Kawada, T.; Dokiya, M. Thermodynamic Stabilities of Perovskite Oxides for Electrodes and Other Electrochemical Materials. *Solid State Ionics* **1992**, *52*, 43–56.
- (26) Shannon, R. D. Revised Effective Ionic Radii and Systematic Studies of Interatomic Distances in Halides and Chalcogenides. *Acta Crystallogr. A: Cryst. Phys., Diffr., Theor. Gen. Crystallogr.* **1976**, *32*, 751–767.
- (27) Tan, X.; Liu, N.; Meng, B.; Sunarso, J.; Zhang, K.; Liu, S. Oxygen Permeation Behavior of $\text{La}_{0.6}\text{Sr}_{0.4}\text{Co}_{0.8}\text{Fe}_{0.2}\text{O}_3$ Hollow Fibre Membranes with Highly Concentrated CO_2 Exposure. *J. Membr. Sci.* **2012**, *389*, 216–222.
- (28) Teraoka, Y.; Nobunaga, T.; Yamazoe, N. Effect of Cation Substitution on the Oxygen Semipermeability of Perovskite-Type Oxides. *Chem. Lett.* **1988**, 503–506.
- (29) Serra, J. M.; Vert, V. B.; Betz, M.; Haanappel, V. A. C.; Meulenberg, W. A.; Tietz, F. Screening of A-Substitution in the System $\text{A}_{0.68}\text{Sr}_{0.3}\text{Fe}_{0.8}\text{Co}_{0.2}\text{O}_{3-\delta}$ for SOFC Cathodes. *J. Electrochem. Soc.* **2008**, *155*, B207–B214.
- (30) Luo, H. X.; Jiang, H. Q.; Klande, T.; Cao, Z. W.; Liang, F. Y.; Wang, H. H.; Caro, J. Novel Cobalt-Free, Noble Metal-Free Oxygen-

Permeable $40\text{Pr}_{0.6}\text{Sr}_{0.4}\text{FeO}_{3-\delta}-60\text{Ce}_{0.9}\text{Pr}_{0.1}\text{O}_{2-\delta}$ Dual-Phase Membrane. *Chem. Mater.* **2012**, *24*, 2148–2154.

(31) Liang, F. Y.; Luo, H. X.; Partovi, K.; Ravkina, O.; Cao, Z. W.; Yi, L.; Caro, J. A Novel CO_2 -Stable Dual Phase Membrane with High Oxygen Permeability. *Chem. Commun.* **2014**, *50*, 2451–2454.

(32) Liang, F. Y.; Partovi, K.; Jiang, H. Q.; Luo, H. X.; Caro, J. B-Site La-Doped $\text{BaFe}_{0.95-x}\text{La}_x\text{Zr}_{0.05}\text{O}_{3-\delta}$ Perovskite-Type Membranes for Oxygen Separation. *J. Mater. Chem. A* **2013**, *1*, 746–751.

(33) Kilner, J. A.; Brook, R. J. A Study of Oxygen Ion Conductivity in Doped Non-Stoichiometric Oxides. *Solid State Ionics* **1982**, *6*, 237–252.

(34) Cherry, M.; Islam, M. S.; Catlow, C. R. A. Oxygen Ion Migration in Perovskite-Type Oxides. *J. Solid State Chem.* **1995**, *118*, 125–132.

(35) Borchert, Y.; Sonstrom, P.; Wilhelm, M.; Borchert, H.; Baumer, M. Nanostructured Praseodymium Oxide: Preparation, Structure, and Catalytic Properties. *J. Phys. Chem. C* **2008**, *112*, 3054–3063.

(36) Lang, F.; Smith, B. C. Ionization Energies of Lanthanides. *J. Chem. Educ.* **2010**, *87*, 875–881.

(37) Ishihara, T.; Kudo, T.; Matsuda, H.; Takita, Y. Doped PrMnO_3 Perovskite Oxide as a New Cathode of Solid Oxide Fuel Cells for Low Temperature Operation. *J. Electrochem. Soc.* **1995**, *142*, 1519–1524.

Chapter 3

Effect of the *B*-Site Co/Fe Ratio on the Permeation Properties and CO₂ Susceptibility of PSCF Membrane

3.1. Summary

Several doping strategies for the improvement of CO₂ stability of MIECs were discussed in Section 1.3.1. A large number of perovskite membranes contain Co and Fe at their *B*-site. Co is known to enhance the ionic conduction, as well as electronic conduction properties of the perovskite and Fe is essential for the phase stability of the membrane. However, the effect of varying Co/Fe ratios on the oxygen permeation performance of the perovskite membranes under air/CO₂ oxygen partial pressure gradient has never been systematically studied.

The following chapter investigates different aspects of varying *B*-site Co contents. Thereby, the structural properties of Pr_{0.6}Sr_{0.4}Co_{*x*}Fe_{1-*x*}O_{3- δ} with $0 \leq x \leq 1$ were studied by XRD techniques and the unit cell parameters were calculated using Rietveld Refinement method. The electrical conductivities of the PSCF series were measured in the temperature range of 30-1000 °C. TGA/DTA was employed to study the oxygen release and retake behavior of PSCF at 30-1250 °C.

The temperature-dependent oxygen permeation fluxes of each membrane under He-sweeping and CO₂-sweeping were compared to establish a relationship between the CO₂ susceptibility and the Co content of the membrane. It was found that generally the oxygen fluxes of the membranes with higher Co contents were more strongly affected by CO₂-sweeping. This effect could also be observed on the microstructures of the spent membranes using SEM. Among the membranes under study, PSC_{*x*}F with $x = 0.2$, showed the lowest CO₂ susceptibility. In conclusion, the membrane also displayed good results as membrane reactor for POM reaction to syngas.

3.2. Effect of the *B*-Site Composition on the Oxygen Permeability and the CO₂ Stability of Pr_{0.6}Sr_{0.4}Co_{*x*}Fe_{1-*x*}O_{3- δ} (0.0 ≤ *x* ≤ 1.0) Membranes

Kaveh Partovi, Benjamin Geppert, Fangyi Liang, Claus H. Rüscher, and Jürgen Caro

Published in Chemistry of Materials **2015**, *27*, 2911-2919.

Reprinted with permission from Chemistry of Materials.

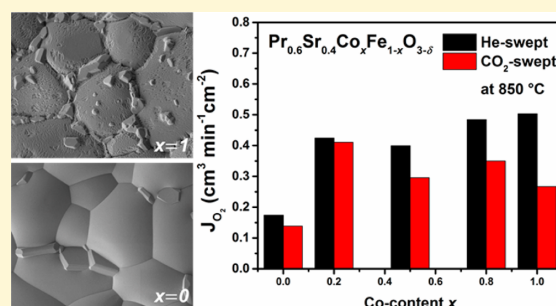
Copyright (2015) American Chemical Society.

Effect of the B-Site Composition on the Oxygen Permeability and the CO₂ Stability of Pr_{0.6}Sr_{0.4}Co_xFe_{1-x}O_{3-δ} (0.0 ≤ x ≤ 1.0) Membranes

Kaveh Partovi,^{*,†} Benjamin Geppert,[†] Fangyi Liang,[†] Claus H. Rüscher,[‡] and Jürgen Caro[†]

[†]Institute of Physical Chemistry and Electrochemistry and [‡]Institute of Mineralogy, Leibniz University of Hannover, Callinstr. 3a, D-30167 Hannover, Germany

ABSTRACT: Dense single-phase perovskite-type Pr_{0.6}Sr_{0.4}Co_xFe_{1-x}O_{3-δ} (0.0 ≤ x ≤ 1.0) membranes (0.6 mm thick) were synthesized via EDTA–citric acid complexing route. Subsequently, the effect of various B-site Co/Fe compositions on oxygen permeability, temperature-dependent CO₂ stability, microstructure, and electrical properties of the membranes were studied. The crystal structures and the high-temperature phase stability of the perovskite structure in a CO₂-containing atmosphere were analyzed using X-ray diffraction. The highest oxygen permeation flux was observed for Pr_{0.6}Sr_{0.4}CoO_{3-δ} with 1.57 cm³(STP) min⁻¹ cm⁻² and 1.37 cm³(STP) min⁻¹ cm⁻² at 1000 °C under air/He and air/CO₂ gradients, respectively. Furthermore, the effect of CO₂ as the sweep gas on the temperature-dependent oxygen permeability and stability of the membranes was studied. Basically, the membranes with lower Co contents were found to be less susceptible to CO₂ exposure and their microstructures were less affected by CO₂. The partial oxidation of methane (POM) to syngas was successfully performed for more than 80 h at 950 °C using a PSCF membrane with a Co content of x = 0.2. The POM reaction shows an average CH₄ conversion rate of >98% and a CO selectivity of >95%.



INTRODUCTION

Mixed ionic-electronic conducting materials (MIECs) and their potential utilization as dense ceramic oxygen-transporting membranes (OTMs) for clean and cost-efficient oxygen production at high temperatures have been the subject of numerous studies during the recent decades. Among MIECs, oxygen-deficient perovskite-type oxides with the general formula ABO₃ such as (Ba,Sr)(Co,Fe)O_{3-δ} and (La,Sr)(Co,Fe)O_{3-δ} have been extensively studied, because of their high oxygen permeabilities.^{1–6} However, the thermochemical and mechanical stability of the perovskite-type oxides under practice-relevant conditions have been a major drawback for the industrial application of perovskites as OTMs. Although the presence of high amounts of alkaline-earth metals, mainly Ba and Sr at the A-site of the perovskite structure enhances the membrane's oxygen permeability, it also increases the reactivity of the membrane material toward acidic gases such as CO₂ and SO₂, ultimately leading to degradation of the membrane performance.^{7–9} Therefore, the CO₂ stability of MIECs is of crucial importance for their application as OTMs in air separation operations involving CO₂-rich environments such as power plants using the oxyfuel concept for carbon capture and sequestration.¹⁰

In order to enhance the CO₂ tolerance of MIECs, several concepts have been developed and studied. Traditional dual-phase materials consisting of a highly stable ionic conductive phase (such as yttrium-stabilized zirconia YSZ) and an electronic conductive phase (mainly noble metals) exhibited

improved thermochemical stability.¹¹ However, lower oxygen permeation fluxes and higher cost of dual-phase membranes compared to perovskite single phase membranes have led to the development of more cost-efficient dual phase materials by replacing the pure electronic conducting phase (such as Pt, Pd, and Ag) with a mixed conducting perovskite phase. Ce_{0.8}Sm_{0.2}O_{1.9}–SmMn_{0.3}Co_{0.5}O₃,¹² Ce_{0.8}Gd_{0.2}O_{2-δ}–La_{0.7}Sr_{0.3}MnO_{3-δ},¹ and Ce_{0.9}Pr_{0.1}O_{2-δ}–Pr_{0.6}Sr_{0.4}Fe_{0.5}Co_{0.5}O_{3-δ}¹⁴ are some examples of dual-phase membranes consisting of a fluorite oxide phase as the ionic conductor and a mixed conducting phase, which showed improved CO₂ tolerance. However, the permeation fluxes of these materials are not sufficient for their large-scale industrial application.

Further approaches have been investigated for the stabilization of the perovskite phase against the formation of Ba or Sr carbonates in CO₂-rich atmospheres. Zeng et al.¹⁵ and Chen et al.¹⁶ reported improved CO₂ stability of SrCo_{0.8}Fe_{0.2}O_{3-δ} (SCF) by Ti and Ta doping of the perovskite's B-site, respectively, and attributed this finding to the reduced basicity of the SCF which results from stronger binding energies of Ti–O and Ta–O, compared to those of Fe–O and Co–O. In our recent paper,¹⁷ we investigated the oxygen permeability and the long-term CO₂ stability of a newly developed

Received: January 14, 2015

Revised: March 30, 2015

Published: March 31, 2015

Pr_{0.6}Sr_{0.4}Co_{0.5}Fe_{0.5}O_{3-δ} (PSCF) membrane and studied the effect of thermal cycles (800–1000 °C) on the membrane's microstructure and permeation performance. The PSCF membrane showed high oxygen permeation fluxes compared to a similar La_{0.6}Sr_{0.4}Co_{0.8}Fe_{0.2}O_{3-δ} (LSCF) membrane under He and CO₂, despite the higher Co content of the LSCF membrane, and maintained a very good CO₂ stability at $T \geq 900$ °C. In the present work, the influence of the Co/Fe ratio at the B-site of the PSCF perovskite on the membrane's oxygen permeation performance, as well as the electrical and structural properties of Pr_{0.6}Sr_{0.4}Co_xFe_{1-x}O_{3-δ} ($0.0 \leq x \leq 1.0$) has been investigated.

■ EXPERIMENTAL SECTION

Sample Preparation. Powder samples of Pr_{0.6}Sr_{0.4}Co_xFe_{1-x}O_{3-δ} (abbreviated as PSCF), with $x = 0, 0.05, 0.2, 0.5, 0.8,$ and 1.0 , were synthesized by a one-pot sol-gel complexing method using ethylenediamine tetraacetic acid (EDTA) and citric acid. Stoichiometric amounts of aqueous solutions of the metal nitrates were mixed together with the complexing agents to obtain a total metal cation/EDTA/citric acid ratio of $\sim 1:1:1.5$. The pH of the solution was adjusted to ~ 9 via the addition of an ammonia solution. The detailed description of the synthesis route is provided elsewhere.^{18,19} The ground powder samples were uniaxially pressed into pellets under a pressure of ~ 120 MPa using a stainless-steel module (18 mm i.d.). The green pellets were sintered at 1200 °C for 5 h in air with heating/cooling rates of 2 °C min⁻¹ to obtain dense disk-shaped PSCF membranes (0.6 mm thick and 16 mm i.d.).

Characterization Techniques. The phase compositions of the samples were analyzed by X-ray diffraction (XRD) techniques at room temperature and in air using a Bruker AXS D8 Advance diffractometer with a Cu K α radiation source. The dataset was acquired in a step-scan mode at an interval of 0.02° in the range of $20^\circ \leq 2\theta \leq 80^\circ$. The high-temperature *in situ* XRD measurements on the PSCF membrane with $x = 0.5$ were performed in an atmosphere consisting of 50 vol % CO₂ and 50 vol % in an *in situ* cell (Model HTK-1200 N, Anton Paar) from 30 °C to 1000 °C using a heating/cooling rate of 12 °C min⁻¹ with a thermal equilibrium time of 30 min prior to data collection at each temperature. Rietveld refinement was applied for the XRD analysis using TOPAS 4.2 software.

The microstructure and the elemental distribution on the surface of the sintered membranes before and after the oxygen permeation measurements were analyzed by scanning electron microscopy (SEM) and energy-dispersive X-ray spectroscopy (EDXS) using a JEOL Model JSM-6700F field-emission scanning electron microscope equipped with a spectrometer (Model INCA A-300, Oxford Instruments) at excitation voltages of 2 kV and 20 kV for SEM and EDXS analyses, respectively.

Temperature-dependent electrical conductivity measurements were conducted on sample bars (~ 1.5 mm \times 0.6 mm \times 10 mm) cut out of the sintered PSCF disks in the temperature range of 30 °C to 1000 °C in ambient air with a heating/cooling rate of 3 °C min⁻¹. The total DC conductivity of the samples was measured on Keithley Model 2100 6-1/2 Digit multimeters with four Pt wires contacted on the sample bar, building a 4-probe geometry. The total conductivity (σ_{total}) can be described as follows:

$$\sigma_{\text{total}} = \frac{I \times L}{V \times A} \quad (1)$$

where V , I , and A represent voltage, current and the cross-section area of the bars, respectively, and L is the distance between the two inner terminals.

Thermoanalysis (TGA/DTA) was performed on Pr_{0.6}Sr_{0.4}Co_xFe_{1-x}O_{3-δ} powder samples with Co contents of $x = 0.05$, $x = 0.2$, and $x = 0.5$, using a Setaram Setsys Evolution 1750 thermoanalyzer from 30 °C to 1250 °C with heating/cooling rates of 10 °C min⁻¹ in synthetic air and a He atmosphere at a flow rate of 20 cm³(STP) min⁻¹. The samples underwent three thermal cycles in a

synthetic air atmosphere and were cooled to room temperature after a hold time of 10 min at the maximum temperature of 1250 °C. In order to minimize the oxygen partial pressure prior to the measurements under He as the inert purge gas, the sample chamber was evacuated for 2 h. Subsequently, three thermal cycles were performed in a He atmosphere. The oxygen uptake behavior was studied after the purge gas was switched back to synthetic air in three additional thermal cycles.

Oxygen Permeation Measurements and Partial Oxidation of Methane. The oxygen permeation measurements were conducted in a homemade high-temperature permeation device described elsewhere.¹⁷ The sintered PSCF membranes were sealed onto an alumina tube using conducting gold paste C5754 (Heraeus, Hanau, Germany) at 950 °C for 5 h. The effective inner surface area of the membranes was ~ 0.6 cm². Synthetic air (20 vol % O₂ and 80 vol % N₂) with a flow rate of 150 cm³(STP) min⁻¹ was applied as the feed gas to one side of the membrane, while the other side of the membrane was swept with He (Linde, 99.999%) or CO₂ (Linde, 99.5%) at a flow of 50 cm³(STP) min⁻¹. All inlet gas streams were controlled by mass flow controllers (MFCs) (Bronkhorst, Ruurlo, The Netherlands) and the total flow rate of the effluent gas was measured by a soap-film flow meter. The gas composition of the effluent was analyzed by an online-coupled gas chromatograph (Agilent, Model 6890A) equipped with a Model Carboxen-1000 column (Supelco). Negligible amounts (<1%) of oxygen leakage from imperfections in the gold sealing were calculated by monitoring the nitrogen concentration in the effluent gas mixture and subtracted from the total flux of oxygen. The operation temperature was measured by a thermocouple placed close to the membrane's surface and all the temperature-dependent data points were acquired after a steady state was reached.

Subsequently, a PSCF membrane with a Co content of $x = 0.2$ was applied as a membrane reactor for the catalytic partial oxidation of methane (POM) to syngas. The experimental setup for the POM reaction was similar to that of the oxygen permeation operation as described previously. 0.4 g of a Ni-based catalyst (Süd Chemie AG) was packed on the permeate side of the membrane. The gas mixture applied on the permeate side of the membrane consisted of methane (Linde, 99.5%) at a flow of 9.2 cm³(STP) min⁻¹ as the reactant gas and Ne (Linde, 99.995%) at a flow of 1.0 cm³(STP) min⁻¹ as the inert internal standard gas for the determination of the total flux of the effluent, while synthetic air with a flow rate of 150 cm³(STP) min⁻¹ was applied on the feed side of the membrane at a reaction temperature of 950 °C. The gas composition of the effluents was analyzed by the online-coupled gas chromatograph.

■ RESULTS AND DISCUSSION

X-ray Diffraction (XRD). The room-temperature X-ray diffraction (XRD) patterns of the as-sintered Pr_{0.6}Sr_{0.4}Co_xFe_{1-x}O_{3-δ} samples are presented in Figure 1. All the PSCF samples consisted of a single perovskite phase, except for the samples with high Co contents of $x = 0.8$ and $x = 1.0$, which contained small amounts of cubic CoO as impurity. The crystal symmetry of the PSCF series at room temperature was found to be a pseudo-cubic perovskite structure with orthorhombic distortion [space group: *Imma* (No. 74)], which is in accordance with previous studies on similar PSCF materials.^{20,21} As shown in Figure 1b, with increasing Co content at the B-site of the ABO₃ structure, a gradual shift of the main reflex position toward higher angles occurs, which is indicative of a reduction of the unit-cell volume. Table 1 lists the calculated unit cell parameters of the PSCF samples at room temperature. This trend of decreasing lattice volume with increasing Co content can be explained by the smaller ionic radii of the 6-fold coordinated high-spin Co cation ($r(\text{Co}^{3+}) = 61$ pm, $r(\text{Co}^{4+}) = 53$ pm) compared to those of high-spin Fe with the same coordination number ($r(\text{Fe}^{3+}) = 64.5$ pm, $r(\text{Fe}^{4+}) = 58.5$ pm).²² The same trend of decreasing cell volume

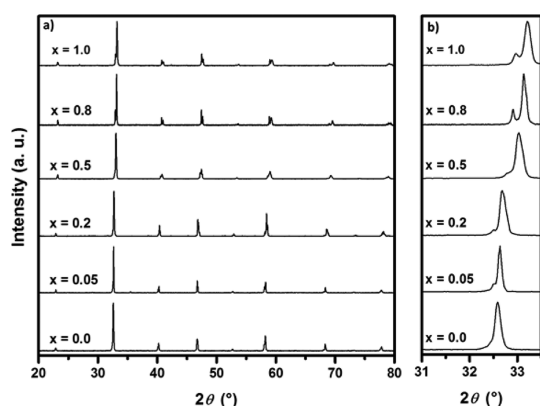


Figure 1. (a) XRD patterns of the as-sintered $\text{Pr}_{0.6}\text{Sr}_{0.4}\text{Co}_x\text{Fe}_{1-x}\text{O}_{3-\delta}$ samples with varying Co contents at room temperature. (b) Magnification of the XRD pattern at $31^\circ \geq 2\theta \geq 33.5^\circ$.

Table 1. Calculated Lattice Constants of $\text{Pr}_{0.6}\text{Sr}_{0.4}\text{Co}_x\text{Fe}_{1-x}\text{O}_{3-\delta}$ with Varying Co Content at Room Temperature

| Co content | <i>a</i> (Å) | <i>b</i> (Å) | <i>c</i> (Å) | <i>V</i> (Å ³) |
|-----------------|--------------|--------------|--------------|----------------------------|
| <i>x</i> = 0.0 | 5.479 | 7.750 | 5.503 | 233.67 |
| <i>x</i> = 0.05 | 5.480 | 7.750 | 5.496 | 233.42 |
| <i>x</i> = 0.2 | 5.452 | 7.709 | 5.484 | 230.50 |
| <i>x</i> = 0.5 | 5.427 | 7.674 | 5.427 | 225.99 |
| <i>x</i> = 0.8 | 5.411 | 7.632 | 5.437 | 223.93 |
| <i>x</i> = 1.0 | 5.383 | 7.607 | 5.429 | 222.34 |

with increasing Co content was reported by Tai et al.²³ for $\text{La}_{1-x}\text{Sr}_x\text{Co}_{1-y}\text{Fe}_y\text{O}_3$ systems.

In order to assess the phase stability of the PSCF materials in CO₂-containing atmospheres, *in situ* XRD measurements were conducted on a powder sample with *x* = 0.5 under an atmosphere of 50 vol % CO₂ and 50 vol % synthetic air at temperatures ranging from room temperature to 1000 °C. The results of the high-temperature *in situ* XRD and the reflex positions of the related structures are presented in Figure 2. It can be seen that a single perovskite phase is maintained during the measurements and no carbonate formation could be evidenced from the *in situ* XRD results. As previously mentioned, the PSCF samples have an orthorhombic perovskite structure at room temperature. With increasing temperature, a phase transition from orthorhombic to rhombohedral symmetry [space group: $R\bar{3}c$ (No. 167)] occurs between 500 °C and 600 °C. The system undergoes a second phase transition to cubic perovskite symmetry [space group $Pm\bar{3}m$ (No. 221)] at 700–800 °C. In our previous paper,¹⁷ we reported the *in situ* phase transitions of the same material in an oxygen-free atmosphere containing 100 vol % CO₂ and it was mentioned that the cubic structure above 800 °C is maintained after cooling the sample to room temperature. However, as XRD patterns in Figure 2 show, in an oxygen-containing environment, the oxygen loss from the lattice is compensated as the temperature decreases to room temperature and, consequently, the initial orthorhombic symmetry is observed again after cooling to room temperature.

Thermogravimetric Analysis (TGA). TGA was performed in order to study the temperature-dependent oxygen release and uptake properties of the $\text{Pr}_{0.6}\text{Sr}_{0.4}\text{Co}_x\text{Fe}_{1-x}\text{O}_{3-\delta}$ powder

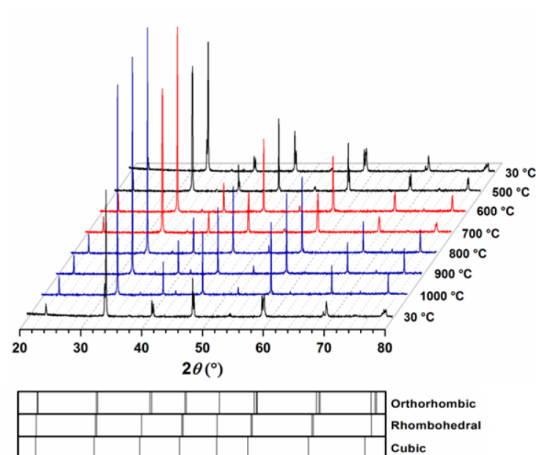


Figure 2. *In situ* XRD patterns of $\text{Pr}_{0.6}\text{Sr}_{0.4}\text{Co}_{0.5}\text{Fe}_{0.5}\text{O}_{3-\delta}$ powder in an atmosphere containing 50 vol % CO₂ and 50 vol % synthetic air at the given temperatures with the reflex positions of orthorhombic, rhombohedral, and cubic perovskite structures.

samples with Co contents of *x* = 0.05, *x* = 0.2, and *x* = 0.5. The TGA results under an oxygen-containing atmosphere using synthetic air as the purge gas are shown in Figure 3a. All samples started to lose weight in a similar trend at ~300 °C, which is attributed to the release of oxygen from the lattice, because of the reduction of Fe and Co cations during heating. The changes of mass displayed complete reversibility upon cooling for the samples with *x* = 0.2 and *x* = 0.5, whereas the sample with the Co content of *x* = 0.05 showed relatively less oxygen uptake after cooling. However, the observed total weight loss after cooling could also be resulted from the high-temperature evaporation of small amounts of Co from the bulk material, as will be discussed later. The rates of weight loss increased gradually with temperature and reached a maximum for *x* = 0.2 and *x* = 0.5 between 900 °C and 950 °C, which is more clearly shown in the inset in Figure 3a. The change of course in weight loss rates between 900 °C and 950 °C can be associated with the reduction of Co and the resulting phase transition from rhombohedral to cubic, which could be confirmed by the appearance of the related endothermic peaks of the temperature-dependent heat flow in Figure 3b. It should be noted that the observed phase transitions are dependent on the oxygen vacancy concentration in the lattice, which can be confirmed by the absence of the related endothermic peaks during the second and the third TG cycles in He. Accordingly, with increasing Co content, the onset temperature of the phase transition decreases and higher weight loss is observed. The occurrence of phase transitions is also in accordance with the previously discussed *in situ* XRD results of $\text{Pr}_{0.6}\text{Sr}_{0.4}\text{Co}_{0.5}\text{Fe}_{0.5}\text{O}_{3-\delta}$. However, the transition from rhombohedral symmetry to cubic symmetry was observed at a lower temperature range (700–800 °C) during the *in situ* XRD measurements compared to the TGA/DTA results (900–950 °C). This temperature shift results from differences in operational parameters during the *in situ* XRD measurements, including application of a 30 min equilibrium time prior to data collection at each temperature and lower oxygen partial pressure applied in the *in situ* cell consisting of 50 vol % CO₂ and 50 vol % synthetic air.

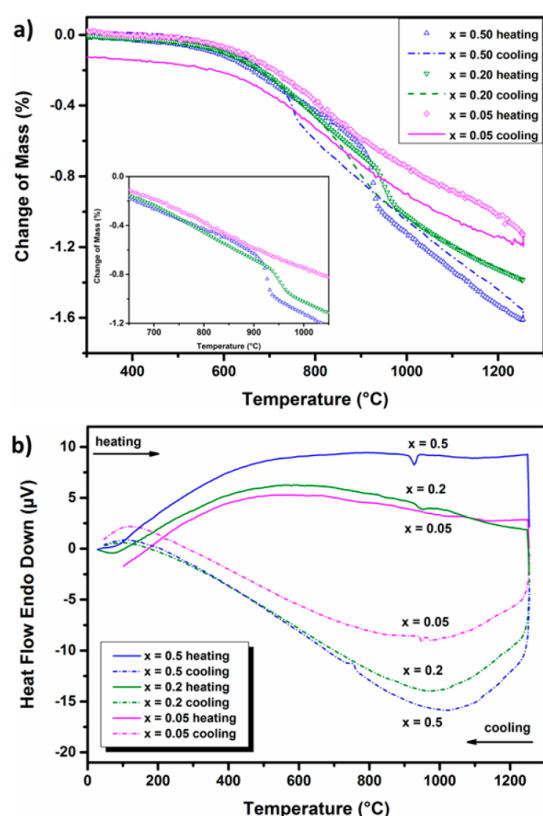


Figure 3. TGA results of Pr_{0.6}Sr_{0.4}Co_xFe_{1-x}O_{3-δ} powder samples with Co contents of $x = 0.05, 0.2,$ and 0.5 in synthetic air: (a) temperature-dependent change of mass (the inset shows only the heating TGA curves), and (b) DTA heating of the PSCF samples as a function of temperature. [Conditions: flow of synthetic air, 20 cm³ min⁻¹; heating/cooling rate, 10 °C min⁻¹.]

In order to enhance the oxygen release performance of the PSCF samples, the TGA measurements were repeated in an oxygen-free atmosphere consisting of pure He as the purge gas. The TGA results are shown in Figure 4a. As expected, the application of He as the purge gas increased the maximum weight loss observed for the sample with $x = 0.5$ from 1.6% to 2.7%, while lowering the onset temperature of oxygen loss. Accordingly, no changes of weight could be observed during cooling in He, because of the absence of oxygen in the purge gas. The oxygen uptake behavior of the samples was studied by the substitution of synthetic air for He as the purge gas. Figure 4b shows the TGA results of the PSCF samples in synthetic air from 30 °C to 1250 °C after the primary cycles in He. The initial weight increase during heating occurs at temperatures below 100 °C for the samples with higher contents of Co, i.e., $x = 0.2$ and $x = 0.5$, whereas, for the low Co content of $x = 0.05$, a higher onset temperature at ~200 °C could be observed. At the end of the temperature cycle in synthetic air, the PSCF sample with a Co content of $x = 0.2$ displayed the lowest total weight loss with 0.1%. The maximum amounts of weight loss and the total weight loss after oxygen uptake for the various PSCF samples are summarized in Table 2. The total weight loss indicates that the reoxidized samples do not fully reach their former weight. This could be resulted from increased volatile

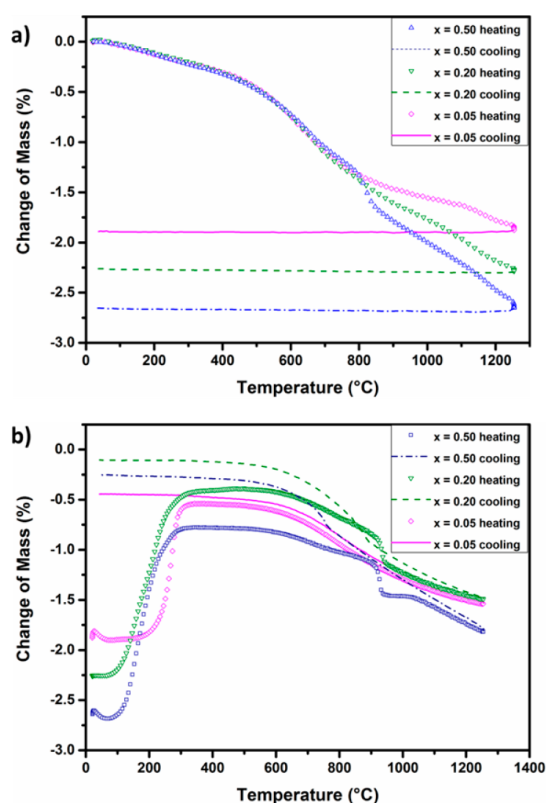


Figure 4. TGA results of Pr_{0.6}Sr_{0.4}Co_xFe_{1-x}O_{3-δ} powder samples with Co contents of $x = 0.05, 0.2,$ and 0.5 (a) in He and (b) in synthetic air. [Conditions: flow of He or synthetic air, 20 cm³ min⁻¹; heating/cooling rate, 10 °C min⁻¹.]

Table 2. Maximum Weight Loss of the PSCF Samples after Heating to 1250 °C in Synthetic Air and He as the Purge Gases and the Total Weight Loss after the Oxygen Uptake

| Co content | max. weight loss in syn air (%) | max. weight loss in He (%) | total weight loss after uptake (%) |
|------------|---------------------------------|----------------------------|------------------------------------|
| $x = 0.05$ | 1.1 | 1.9 | 0.4 |
| $x = 0.2$ | 1.4 | 2.3 | 0.1 |
| $x = 0.5$ | 1.6 | 2.7 | 0.3 |

behavior of cobalt, which tends to evaporate from the material at elevated temperatures. It should be noted that the highest amount of total weight loss was observed for the PSCF sample with the lowest Co content of $x = 0.05$. This might be correlated to the larger unit cell of this sample compared to those of $x = 0.2$ and $x = 0.5$, which can facilitate the diffusion of Co out of the bulk material. However, other possibilities, such as slight changes of structure due to high-temperature treatment under low oxygen partial pressures should also be taken into consideration.

Electrical Conductivity. In terms of electronic conductivity, our PSCF material exhibited a semiconductor behavior at the lower temperature range, where conductivity increased with temperature until a maximum conductivity was reached at a certain temperature. At higher temperatures, however, the conductivities decreased with increasing temperatures, implying

metallic behavior. Figure 5 shows the temperature-dependent total electrical conductivity of the Pr_{0.6}Sr_{0.4}Co_xFe_{1-x}O_{3-δ}

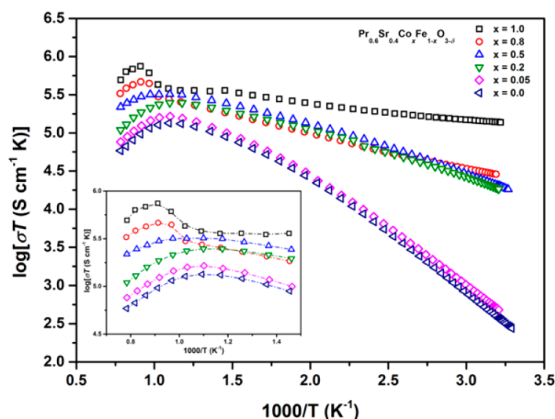
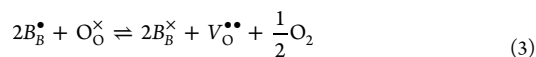


Figure 5. Temperature dependence of electrical conductivities of Pr_{0.6}Sr_{0.4}Co_xFe_{1-x}O_{3-δ} membranes in air, represented as Arrhenius plots.

samples with varying Co contents ($0.0 \leq x \leq 1.0$) measured in ambient air. According to previous studies,^{24,25} the ionic oxygen conduction in perovskite-type oxides is ~ 2 orders of magnitude smaller than the electronic conductivity, therefore the measured values for total electrical conductivity can be attributed to the electronic conductivity, which ranged from 0.904 S cm^{-1} for $x = 0$ at room temperature to a maximum of 705 S cm^{-1} for $x = 1$ at 1060 K (ca. $787 \text{ }^\circ\text{C}$). At lower temperatures, the conductivity (denoted as σ) increases almost linearly with increasing temperature, indicating that the electronic conduction is mediated by small-polaron hopping mechanism via B–O–B conduction pairs,²⁶ which can be expressed by the following equation:^{27,28}

$$\sigma = \frac{C}{T} \exp\left(-\frac{E_a}{kT}\right) \quad (2)$$

where T is the absolute temperature, E_a is the activation energy, and k represents the Boltzmann constant. The pre-exponential constant (C) is a material characteristic parameter that includes the charge carrier concentration term.²⁹ A deviation from linearity is observed at higher temperatures. After reaching a maximum conductivity at T_{max} , the conductivities decrease with increasing temperature, as a result of the significant increase of oxygen vacancies in the lattice. Many effects are explained by the decreasing electronic conductivity with the increasing loss of oxygen lattice at temperatures above T_{max} , as the pre-exponential factor in eq 2 containing the charge carrier concentration becomes a predominant factor for conductivity. With loss of oxygen lattice at higher temperatures, the concentration of the p -type charge carriers inclines, i.e., the B-site species in their higher oxidation states are reduced,²⁹ as described by the following equation using Kröger–Vink notations:³⁰



where B represents the B-site cation (e.g., Co and Fe) and $V_O^{\bullet\bullet}$ is an oxygen vacancy. Another important effect associated with decreasing conductivity due to lattice oxygen loss, is the loss of

the overlap between the $3d$ -orbitals of the transition metal and the $2p$ -orbitals of oxygen, which mediates the hopping mechanism.³¹

The magnitude of maximum conductivity increases with Co content at the B-site, as a result of increased acceptor doping, which is also in agreement with previous studies on similar perovskite-type oxides such as La_{1-x}Sr_xCo_yFe_{1-y}O_{3-δ} (LSCF)²⁴ and Ba_{0.5}Sr_{0.5}Co_{1-y}Fe_yO_{3-δ} (BSCF).³² Furthermore, for $x \geq 0.2$, the T_{max} values shifted to higher temperatures with increasing Co content. Table 3 lists the empirical T_{max} values

Table 3. Calculated Activation Energies for Electronic Conduction of Pr_{0.6}Sr_{0.4}Co_xFe_{1-x}O_{3-δ} with Varying Co Content at Temperatures of 30–400 °C

| Co content | E_a (eV) | T_{max} (°C) |
|------------|------------|-----------------------|
| $x = 0.0$ | 0.24 | 560–570 |
| $x = 0.05$ | 0.24 | 600–610 |
| $x = 0.2$ | 0.11 | 500–510 |
| $x = 0.5$ | 0.11 | 530–540 |
| $x = 0.8$ | 0.10 | 770–775 |
| $x = 1.0$ | 0.05 | 785–790 |

and the activation energies for the electronic conduction, which were calculated using the linear fit of the Arrhenius plots (Figure 5) between $30 \text{ }^\circ\text{C}$ and $400 \text{ }^\circ\text{C}$. The calculated values for activation energy range between 0.054 and 0.244 eV , which is comparable to the data reported in the literature for the similar LSCF compounds with E_a from 0.04 eV to 0.14 eV .^{24,29} Although a general trend of decreasing activation energies with increasing Co content can be observed, the calculated E_a for a Co content of $x = 0.2$ was found to be slightly smaller than that of the compound with $x = 0.5$.

Oxygen Permeation. The oxygen permeation fluxes of the PSCF membranes at temperatures between $750 \text{ }^\circ\text{C}$ and $1000 \text{ }^\circ\text{C}$ were measured using pure He (Figure 6a) and pure CO₂ (Figure 6b) as the sweep gases. For the He-swept measurements, an increasing oxygen permeability was observed with increasing Co content at the B-site, which is in agreement with previous studies.^{32–34} As expected, the end-members Pr_{0.6}Sr_{0.4}CoO_{3-δ} and Pr_{0.6}Sr_{0.4}FeO_{3-δ} with oxygen fluxes of 1.57 and $0.63 \text{ cm}^3(\text{STP}) \text{ min}^{-1} \text{ cm}^{-2}$ exhibited the highest and the lowest oxygen permeation fluxes, respectively, among the PSCF membranes under study. This trend can be primarily attributed to the lower average valence state of Co, compared to that of Fe, which results in a higher concentration of oxygen lattice vacancies, as well as smaller binding energy of Co–O than Fe–O.^{32,33} Further oxygen permeation measurements were conducted on the same membranes using pure CO₂ as the sweep gas. As expected, a slight decrease of the oxygen permeation fluxes was observed for the membranes with CO₂ sweeping, in comparison with He sweeping. However, as shown in Figure 6b, the decrease in oxygen fluxes is dependent on the Co contents of the membranes, resulting in a different trend of oxygen fluxes than the trend observed for the measurements with He sweeping. For example, at $1000 \text{ }^\circ\text{C}$, the oxygen permeation fluxes measured for the CO₂-swept Pr_{0.6}Sr_{0.4}Co_xFe_{1-x}O_{3-δ} membranes with $x \geq 0.5$ were almost equal, whereas at the same temperature the permeation fluxes of the same membranes with He as the sweep gas differed considerably, according to their Co contents. As a result, at $850 \text{ }^\circ\text{C}$ the order of oxygen fluxes observed for CO₂-swept membranes changed from that of He-swept membranes,

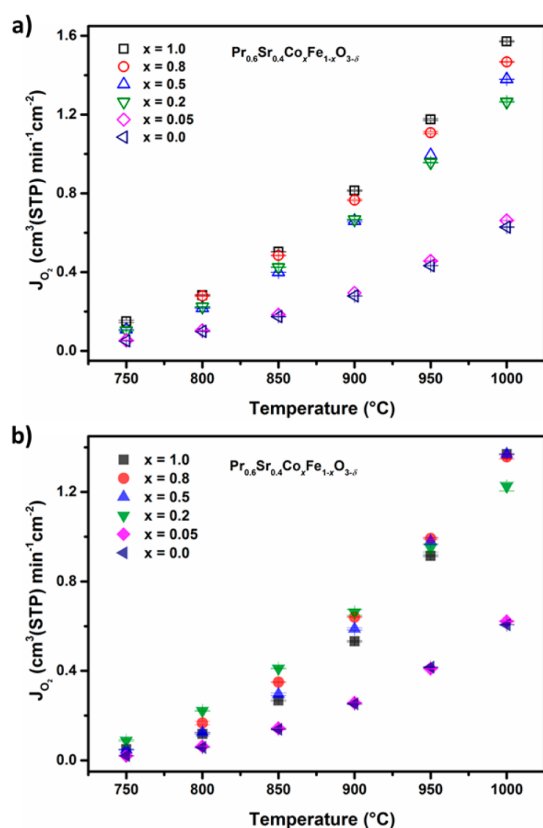


Figure 6. Temperature dependence of oxygen permeation fluxes measured on PSCF membranes with various Co contents at the B-site with (a) He as the sweep gas and (b) CO₂ as the sweep gas. [Conditions: feed-side flow rate, 150 cm³(STP) min⁻¹ of synthetic air; sweep-side flow rate, 50 cm³(STP) min⁻¹ of He (panel a) or CO₂ (panel b); membrane thickness, 0.6 mm.]

where the highest oxygen permeation flux was measured for $x = 0.2$, followed by $x = 0.8$ and $x = 0.5$, with the end member Pr_{0.6}Sr_{0.4}CoO_{3- δ} exhibiting less oxygen permeability than the other three compositions. The low-Co samples with $x = 0.0$ and $x = 0.05$ exhibited the lowest permeation fluxes with both He and CO₂ as the sweep gases.

The oxygen permeation changes due to the switching of the sweep gas from He to CO₂ can be roughly presented as the ratio of decrease in oxygen flux to the oxygen flux measured with He sweeping at different temperatures (as shown in Figure 7):

$$J_{\text{O}_2} \text{ drop (\%)} = \frac{J_{\text{O}_2, \text{He}} - J_{\text{O}_2, \text{CO}_2}}{J_{\text{O}_2, \text{He}}} \times 100 \quad (4)$$

where $J_{\text{O}_2, \text{He}}$ and $J_{\text{O}_2, \text{CO}_2}$ represent the oxygen permeation fluxes with He and CO₂ as the sweep gases, respectively. As expected, the changes in oxygen permeation flux become increasingly larger with decreasing temperature, since the carbonate formation is thermodynamically favored at lower temperatures. However, this trend could not be observed for the PSCF membrane with a Co content of $x = 0.2$, which showed the lowest susceptibility against carbonate formation among all

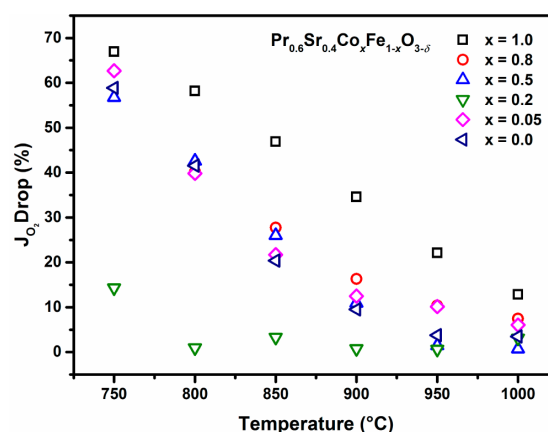


Figure 7. Temperature-dependent changes in oxygen permeation fluxes for the PSCF membranes with different B-site compositions as the sweep gas was switched from He to CO₂.

membranes. In direct contrast to the results of PSCF with $x = 0.2$, the end-member Pr_{0.6}Sr_{0.4}CoO_{3- δ} showed a semilinear trend of increasing change with decreasing temperatures and its permeability was most negatively affected by CO₂ exposure, at all temperatures.

Generally, perovskites with higher stabilization energies are less vulnerable to carbonate formation in a CO₂-containing atmosphere. Moreover, the basicity of the alkaline-earth oxide (here, Sr) plays a major role in the reactivity of the perovskite with acidic CO₂ and thermodynamically favorable formation of carbonate.³⁵ In an oxygen-deficient PSCF perovskite system, the average oxidation state of Fe (between 3+ and 4+) is higher than that of Co (between 2+ and 3+).³⁶ Therefore, the higher resistance against SrCO₃ formation for Fe-rich perovskites can result from the higher electronegativity of Fe compared to Co, causing increased acidity of the B-site species. The influence of the electronegativity of the B-site cations on the CO₂-stability was recently reported for the proton-conducting BaCe_{1-x-y}Nb_xZr_yO_{3- δ} .³⁷ Similar behavior of increased CO₂ stability was observed for the perovskite-type system Ba(Co,Fe,Nb)O_{3- δ} , as the Fe content was increased in relation to Co.³⁸ It should be noted that both of the above-mentioned systems contain a single A-site element, whereas our PSCF perovskites contains two A-site cations. Moreover, the enhanced oxygen permeation performance of the PSCF membrane with a Co content of $x = 0.2$ under a CO₂ atmosphere (at $T \leq 950$ °C) and its lowest CO₂ susceptibility among other membranes implies that a conditional balance between high oxygen ionic conductivity and low CO₂ reactivity might be achieved with 20 at. % Co doping at the B-site.

The CO₂ stability of the PSCF membrane with $x = 0.2$ was further investigated in a long-term permeation test for more than 400 h using pure He and pure CO₂ as sweep gases, as shown in Figure 8. The PSCF membrane showed very good stability at 1000 °C under CO₂ for more than 150 h. Furthermore, the oxygen permeation performance at the lower temperature of 850 °C was very good and no decrease of oxygen flux was observed for more than 100 h in total. The absence of decreasing oxygen fluxes at 850 °C for the PSCF membrane with $x = 0.2$, is in contrast with the results of the long-term oxygen permeation measurements of our previously

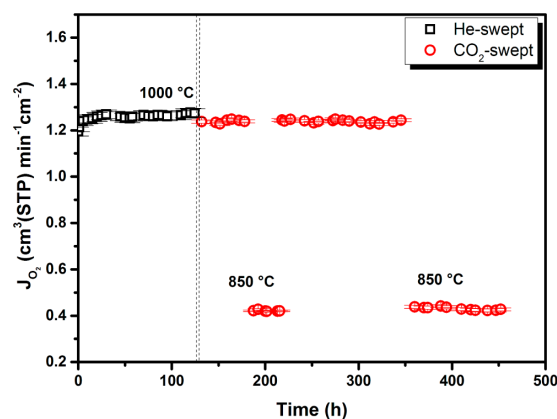


Figure 8. Long-term oxygen permeation performance of the PSCF membrane with a Co content of $x = 0.2$ with He (black square, ■) and CO₂ (red circle, ●) as sweeping gases at 1000 °C and 850 °C. [Conditions: sweep side flow rate, 50 cm³(STP) min⁻¹ of He or CO₂; feed side flow rate, 150 cm³(STP) min⁻¹ of synthetic air; membrane thickness, 0.6 mm.]

published PSCF membrane with $x = 0.5$, that showed states of decreasing and increasing oxygen fluxes at 850 and 1000 °C, respectively, because of the formation and decomposition of SrCO₃ on the CO₂-swept side of the membrane.¹⁷ This finding is also in good accordance with the observation of increased CO₂ susceptibility of membranes with higher Co contents.

Scanning Electron Microscopy (SEM). The surface microstructure of the PSCF membranes before and after the long-term measurements with CO₂ sweeping was studied using SEM. Figure 9 shows the SEM micrographs of the surface of the PSCF membranes with varying Co content before (insets) and after the measurements with CO₂ as the sweeping gas. The freshly sintered membranes were found to be free of cracks and consisted of densely packed grains. However, considering similar sintering parameters (i.e., ramping rate, sintering temperature, and dwell time, as mentioned in the Experimental Section) applied for all samples, a gradual increase of grain size with increasing Co content is observed. Furthermore, for the membranes with $x \geq 0.8$ (Figures 9e and 9f), Co-rich particles were detected on the as-sintered membrane surface using EDXS. The observation of CoO particles as a secondary phase has been previously reported for similar LSCF compositions.²⁹

All membranes were measured under controlled conditions, i.e., the operation temperatures and the duration of CO₂ exposure at each temperature were identical for all samples. However, for the PSCF membranes with Co contents of $x = 0.5$ and higher, some etching patterns on the grains surfaces can be observed, which could not be recognized for other membranes with lower Co contents. This finding could also be relevant to the detected changes in the oxygen permeation fluxes by switching the sweep gas from He to CO₂, suggesting that perovskites with higher Co/Fe concentrations are more susceptible to carbonate formation.

Partial Oxidation of Methane to Syngas. One of the potential applications of MIECs, which has been investigated intensively during the past two decades, is their utilization as oxygen-transporting membranes (OTMs) for chemical processes such as catalytic partial oxidation of methane (POM) to syngas (CO + 2H₂),^{39–41} described by the following equation:

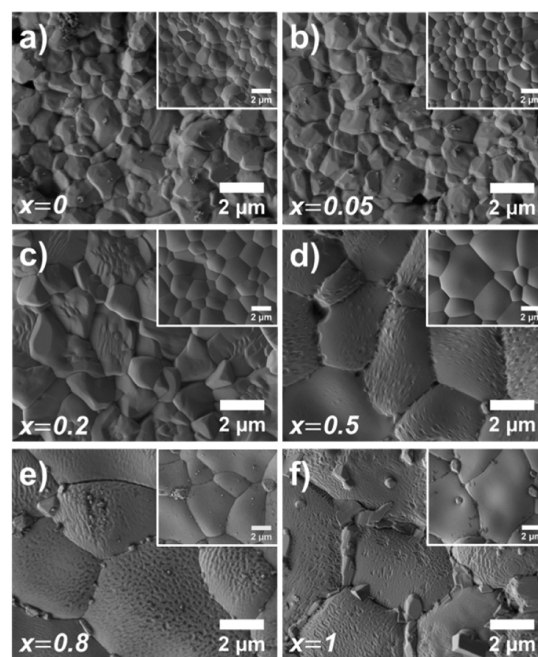
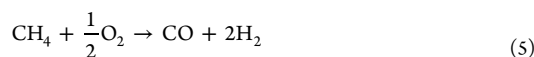


Figure 9. SEM micrographs of the Pr_{0.6}Sr_{0.4}Co_xFe_{1-x}O_{3-δ} membranes with varying Co content ($0.0 \leq x \leq 1.0$) after oxygen permeation measurements with CO₂ as the sweeping gas. The insets are the micrographs of the as-sintered membranes.



Syngas production via POM is an attractive route for gas-to-liquid (GTL) processes, since the reaction with an enthalpy of $\Delta H(298 \text{ K}) = -35.67 \text{ kJ mol}^{-1}$ is slightly exothermic in comparison with the strongly endothermic steam reforming ($\Delta H(298 \text{ K}) = +206.16 \text{ kJ mol}^{-1}$) as the dominant process for syngas production.^{39,41,42} The high-purity oxygen feed for the catalytic POM reaction is traditionally provided by a cryogenic air separation unit. However, the replacement of the cryogenic air separation unit with MIECs as the oxygen suppliers and distributors can result in an estimated reduction of the related costs by 25%–30%.^{42,43}

In an attempt to assess the applicability of our PSCF membranes for the POM reaction, the membrane with a Co content of $x = 0.2$ was selected, because of its relatively good performance in the previously discussed oxygen permeation operations with pure CO₂ as the sweep gas. The results of the POM reaction using an alumina-supported NiO-based catalyst are shown in Figure 10. The conversion rate of methane increased from 90% to >98% after an activation stage of more than 20 h, during which Ni, in its oxidized form, was reduced to the catalytically active Ni⁰ species.⁴² This initial activation stage has been reported in various studies.^{44,45} After the initial activation stage, a conversion rate of 98%–99% was maintained for more than 80 h of total operation time. Furthermore, the CO selectivity was found to be 95%–98%, which is comparable with results from other studies on dual-phase membranes under similar conditions.^{44,46}

In conclusion, our preliminary results for the application of the PSCF membrane in POM to syngas were in good

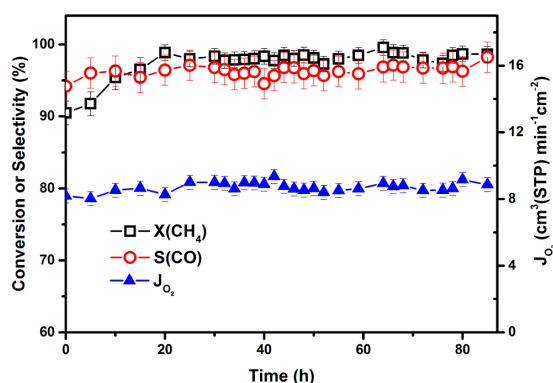


Figure 10. Time-dependent CH₄ conversion ($X(\text{CH}_4)$), CO selectivity ($S(\text{CO})$), and O₂ permeation flux (J_{O_2}) with Pr_{0.6}Sr_{0.4}Co_xFe_{1-x}O_{3- δ} membrane for POM to syngas at 950 °C. [Conditions: feed side flow rate, 150 cm³(STP) min⁻¹ of synthetic air; sweep side flow rate, 9.2 cm³(STP) min⁻¹ of CH₄ + 1 cm³(STP) min⁻¹ of Ne as the internal standard; membrane thickness, 0.6 mm.]

agreement with literature data. Nevertheless, the long-term chemical stability and the possible failure mechanisms associated with the operation under reducing atmospheres could be the subject of another study.

CONCLUSION

All the Pr_{0.6}Sr_{0.4}Co_xFe_{1-x}O_{3- δ} (PSCF) samples under study with Co contents of $0.0 \leq x \leq 1.0$ possess an orthorhombic perovskite structure at room temperature. The *in situ* XRD analysis revealed a cubic symmetry above 800 °C for the $x = 0.5$ composition. This phase transition could also be observed in the TG/DTA measurements by an endothermic peak. Among the CO₂-stable oxygen transporting membranes, our PSCF membrane shows high oxygen permeation fluxes both with pure He and pure CO₂ as sweep gases. Although the permeation flux under a synthetic air/He oxygen partial pressure gradient increased with the Co content of the B-site, it was found that this trend slightly changed under an air/CO₂ oxygen partial pressure gradient, as a result of increased basicity of the material, because of a higher Co content. Subsequently, the SEM imaging revealed increased deterioration of the microstructure for the membranes with higher Co contents after using CO₂ as the sweep gas. The lowest CO₂ susceptibility was observed for the PSCF membrane with 20 at. % Co at the B-site, which exhibited the highest oxygen permeation flux with CO₂ sweeping in the temperature range of 750–900 °C. The long-term performance of the PSCF membrane ($x = 0.2$) was further tested with pure CO₂ as the sweep gas for more than 150 h at 1000 °C and 100 h at 850 °C, which showed very good CO₂ stability and no degradation of the oxygen permeation flux. The performance of the PSCF ($x = 0.2$) membrane as a membrane reactor for the partial oxidation of methane to syngas has been successfully evaluated.

AUTHOR INFORMATION

Corresponding Author

*E-mail: kaveh.partovi@pci.uni-hannover.de.

Notes

The authors declare no competing financial interest.

ACKNOWLEDGMENTS

The authors greatly acknowledge the financial support by the Sino-German Centre for Research Promotion (Nos. GZ676 and GZ911) and DFG Ca 147/18-1. Prof. A. Feldhoff is gratefully acknowledged for the fruitful discussions. O. Ravkina, A. Schulz, and A. Duong are acknowledged for the *in situ* XRD analyses and measurements.

REFERENCES

- (1) Shao, Z. P.; Yang, W. S.; Cong, Y.; Dong, H.; Tong, J. H.; Xiong, G. X. *J. Membr. Sci.* **2000**, *172*, 177.
- (2) Liang, F. Y.; Jiang, H. Q.; Luo, H. X.; Caro, J.; Feldhoff, A. J. *Chem. Mater.* **2011**, *23*, 4765.
- (3) Baumann, S.; Serra, J. M.; Lobera, M. P.; Escolástico, S.; Schulze-Küppers, F.; Meulenberg, W. A. J. *J. Membr. Sci.* **2011**, *377*, 198.
- (4) Teraoka, Y.; Zhang, H. M.; Yamazoe, N. *Chem. Lett.* **1985**, 1367.
- (5) Petric, A.; Huang, P.; Tietz, F. *Solid State Ionics* **2000**, *135*, 719.
- (6) Klande, T.; Ravkina, O.; Feldhoff, A. J. *J. Membr. Sci.* **2013**, *437*, 122.
- (7) Bouwmeester, H. J. M.; Burggraaf, A. J. In *Fundamentals of Inorganic Membrane Science and Technology*; Burggraaf, A. J., Cot, L., Eds.; Elsevier Science BV: Amsterdam, 1996; Chapter 10, p 435.
- (8) Arnold, M.; Wang, H. H.; Feldhoff, A. J. *J. Membr. Sci.* **2007**, *293*, 44.
- (9) Benson, S. J.; Waller, D.; Kilner, J. A. J. *Electrochem. Soc.* **1999**, *146*, 1305.
- (10) Schulz, M.; Krieger, R.; Kämpfer, A. J. *J. Membr. Sci.* **2011**, *378*, 10.
- (11) Chen, C. S.; Kruidhof, H.; Bouwmeester, H. J. M.; Verweij, H.; Burggraaf, A. J. *Solid State Ionics* **1996**, *86–88*, 569.
- (12) Zhu, X. F.; Liu, H.; Cong, Y.; Yang, W. *Chem. Commun.* **2012**, *48*, 251.
- (13) Kharton, V. V.; Kovalevsky, A.; Viskup, A.; Figueiredo, F.; Yaremchenko, A.; Naumovich, E.; Marques, F. J. *Electrochem. Soc.* **2000**, *147*, 2814.
- (14) Liang, F. Y.; Luo, H. X.; Partovi, K.; Ravkina, O.; Cao, Z. W.; Liu, Y.; Caro, J. *Chem. Commun.* **2014**, *50*, 2451.
- (15) Zeng, Q.; Zuo, Y.; Fan, C.; Chen, C. J. *J. Membr. Sci.* **2009**, *335*, 140.
- (16) Chen, W.; Chen, C.; Winnubst, L. *Solid State Ionics* **2011**, *196*, 30.
- (17) Partovi, K.; Liang, F. Y.; Ravkina, O.; Caro, J. *ACS Appl. Mater. Interfaces* **2014**, *6*, 10274.
- (18) Martynczuk, J.; Arnold, M.; Wang, H. H.; Caro, J.; Feldhoff, A. *Adv. Mater.* **2007**, *19*, 2134.
- (19) Liang, F. Y.; Partovi, K.; Jiang, H. Q.; Luo, H. X.; Caro, J. *J. Membr. Sci.* **2013**, *1*, 746.
- (20) Qiu, L.; Ichikawa, T.; Hirano, A.; Imanishi, N.; Takeda, Y. *Solid State Ionics* **2003**, *158*, 55.
- (21) Yin, Y. M.; Xiong, M. W.; Yang, N. T.; Tong, Z.; Guo, Y. Q.; Ma, Z. F.; Sun, E.; Yamanis, J.; Jing, B. Y. *Int. J. Hydrogen Energy* **2011**, *36*, 3989.
- (22) Shannon, R. D. *Acta Crystallogr., Sect. A: Cryst. Phys., Diffr., Theor. Gen. Crystallogr.* **1976**, *32*, 751.
- (23) Tai, L. W.; Nasrallah, M. M.; Anderson, H. U.; Sparlin, D. M.; Sehlin, S. R. *Solid State Ionics* **1995**, *76*, 259.
- (24) Stevenson, J. W.; Armstrong, T. R.; Carneim, R. D.; Pederson, L. R.; Weber, W. J. *J. Electrochem. Soc.* **1996**, *143*, 2722.
- (25) Tsai, Ch. Y.; Dixon, A. G.; Ma, Y. H.; Moser, W. R.; Pascucci, M. R. *J. Am. Ceram. Soc.* **1998**, *81*, 1437.
- (26) ten Elshof, J. E.; Bouwmeester, H. J. M.; Verweij, H. *Appl. Catal., A* **1995**, *130*, 195.
- (27) Karim, D. P.; Aldred, A. T. *Phys. Rev. B* **1979**, *20*, 2255.
- (28) Goodenough, J. B. *Phys. Rev.* **1967**, *164*, 785.
- (29) Tai, L. W.; Nasrallah, M. M.; Anderson, H. U.; Sparlin, D. M.; Sehlin, S. R. *Solid State Ionics* **1995**, *76*, 273.
- (30) Kröger, F. A.; Vink, H. J. *Solid State Physics*; Academic Press: New York, 1956.

- (31) Deng, Z. Q.; Zhang, G. G.; Liu, W.; Peng, D. K.; Chen, C. L. *Solid State Ionics* **2002**, *152–153*, 735.
- (32) Chen, Z.; Ran, R.; Zhou, W.; Shao, Z.; Liu, S. *Electrochim. Acta* **2007**, *52*, 7343.
- (33) Teraoka, Y.; Zhang, H. M.; Furukawa, S.; Yamazoe, N. *Chem. Lett.* **1985**, 1743.
- (34) Teraoka, Y.; Nobunaga, T.; Okamoto, K.; Miura, N.; Yamazoe, N. *Solid State Ionics* **1991**, *48*, 207.
- (35) Yokokawa, H.; Sakai, N.; Kawada, T.; Dokiya, M. *Solid State Ionics* **1992**, *52*, 43.
- (36) Mueller, D.; De Souza, R.; Brendt, J.; Samuelis, D.; Martin, M. J. *Mater. Chem.* **2009**, *19*, 1960.
- (37) Gore, C.; White, J.; Wachsman, E.; Thangadurai, V. *J. Mater. Chem. A* **2014**, *2*, 2363.
- (38) Yi, J.; Schroeder, M.; Weirich, T.; Mayer, J. *Chem. Mater.* **2010**, *22*, 6246.
- (39) Caro, J.; Caspary, K. J.; Hamel, C.; Hoting, B.; Koelsch, P.; Langanke, B.; Nassauer, K.; Schiestel, T.; Schmidt, A.; Schomaecker, R.; Seidel-Morgenstern, A.; Tsotsas, E.; Voigt, I.; Wang, H.; Warsitz, R.; Werth, S.; Wolf, A. *Ind. Eng. Chem. Res.* **2007**, *46*, 2286.
- (40) Balachandran, U.; Dusek, J. T.; Mieville, R. L.; Poeppel, R. B.; Kleefisch, M. S.; Pei, S.; Kobylinski, T. P.; Udovich, C. A.; Bose, A. C. *Appl. Catal., A* **1995**, *133*, 19.
- (41) Wang, H. H.; Tablet, C.; Schiestel, T.; Werth, S.; Caro, J. *Catal. Commun.* **2006**, *7*, 907.
- (42) Dong, H.; Shao, Z.; Xiong, G.; Tong, J.; Sheng, S.; Yang, W. *Catal. Today* **2001**, *67*, 3.
- (43) Bouwmeester, H. J. M. *Catal. Today* **2003**, *82*, 141.
- (44) Luo, H. X.; Jiang, H. Q.; Klande, T.; Cao, Z. W.; Liang, F. Y.; Wang, H. H.; Caro, J. *Chem. Mater.* **2012**, *24*, 2148.
- (45) Tong, J.; Yang, W.; Suda, H.; Haraya, K. *Catal. Today* **2006**, *118*, 144.
- (46) Zhu, X. F.; Li, Q.; He, Y.; Cong, Y.; Yang, W. *J. Membr. Sci.* **2010**, *360*, 454.

Chapter 4

Cobalt-Containing Dual-Phase Membranes

4.1. Summary

As discussed in Section 1.3.2., dual-phase membranes containing fluorite-type doped ceria as the main oxygen ion conducting phase, show higher stability in CO₂-rich environments.

The following chapter introduces a newly developed dual-phase membrane based on the previously studied PSCF perovskite, with the composition 40 wt.% Pr_{0.6}Sr_{0.4}Co_{0.5}Fe_{0.5}O_{3-δ}- 60 wt.% Ce_{0.9}Pr_{0.1}O_{2-δ} (PSCF-CP). The membrane showed remarkably improved permeation properties compared to a Co-free dual-phase membrane PSF-CP with a similar composition. The long-term CO₂ stability of the membranes was studied for a total of 800 h at the temperature range of 800-1000 °C. The room temperature phase structure, as well as the high-temperature structural properties of the composite material under CO₂ atmosphere were investigated using *in-situ* XRD, which were in good agreement with the previously conducted studies conducted on PSCF perovskites, presented in Chapters 2 & 3.

4.2. A Novel CO₂-Stable Dual Phase Membrane with High Oxygen Permeability

Fangyi Liang, Huixia Luo, Kaveh Partovi, Olga Ravkina, Zhengwen Cao, Yi Liu, and Jürgen Caro

Published in *Chemical Communications* **2014**, *50*, 2451-2454.

Reprinted with permission from *Chemical Communications*.

Copyright (2014) Royal Society of Chemistry.



ChemComm

COMMUNICATION

View Article Online
View Journal | View Issue

A novel CO₂-stable dual phase membrane with high oxygen permeability†

Cite this: *Chem. Commun.*, 2014, 50, 2451Received 16th October 2013,
Accepted 9th January 2014

DOI: 10.1039/c3cc47962e

www.rsc.org/chemcomm

Fangyi Liang,*^a Huixia Luo,^b Kaveh Partovi,^a Olga Ravkina,^a Zhengwen Cao,^a Yi Liu^a and Jürgen Caro^a

By cobalt-doping of the mixed conducting phase PSFC, a good combination of high CO₂ stability and high oxygen permeability is obtained for the 60 wt% Ce_{0.9}Pr_{0.1}O_{2-δ}-40 wt% Pr_{0.6}Sr_{0.4}Fe_{0.5}Co_{0.5}O_{3-δ} (CP-PSFC) dual phase membrane, which suggests that CP-PSFC is a promising membrane for industrial applications in the oxyfuel process for CO₂ capture.

CO₂ capture and storage technologies in power plants have gained attention worldwide¹ since the combustion of fossil fuel is considered to be the main contribution to CO₂ emissions. Oxygen transporting membranes (OTMs)² based on mixed electronic and ionic conductors, can supply oxygen of 100% purity to power stations for CO₂ capture according to the oxyfuel for CO₂ capture and storage.³ The oxyfuel concept involves the combustion of fossil fuels with an oxygen/exhaust gas mixture. The pure oxygen used in the oxyfuel process can be produced using the Linde cryogenic technique. However, by using OTMs, oxygen can be separated from air by using a part of the exhaust gas CO₂ as a sweep gas. Oxygen production by using OTMs can reduce the costs by 35% and save 60% energy compared to the conventional cryogenic process.⁴ A part of the exhaust gas CO₂ is sequestered, and another part is recycled and used as sweep gas for the oxygen separation through the OTMs. Thus, the OTMs for CO₂ capture in the oxyfuel process should have not only good stability in a CO₂ atmosphere but also high oxygen permeation performance at elevated temperatures. Moreover, OTMs can be used in many promising potential applications, such as in high-purity oxygen production,⁵ in catalytic membrane reactors,⁶ and as cathodes in solid oxide fuel cells (SOFCs).⁷

Among OTMs, many cobalt-based single phase perovskite-type membranes such as Ba_{1-x}Sr_xCo_{1-y}Fe_yO_{3-δ} exhibit high oxygen permeability⁸ since cobalt can provide a high concentration of

mobile oxygen vacancies in the perovskite lattice over a wide temperature range.⁹ However, under a CO₂ atmosphere these membranes immediately lose their oxygen permeation flux, since the alkaline-earth metals on the A site of the perovskite framework form carbonates with CO₂.¹⁰ Recently, dual phase membranes with good structural stability and CO₂ resistance, made of a micro-scale mixture of well separated grains of the two phases of an oxygen ionic conductor and an electronic conductor, have attracted much attention for the application of the O₂ production in the oxyfuel concept. However, the low oxygen permeability of dual phase membranes needs to be improved to meet the industrial application requirements.¹¹ Zhu *et al.* improved the oxygen permeability of their CO₂-stable dual phase membranes, such as Ce_{0.8}Sm_{0.2}O_{1.9}-SmMn_{0.5}Co_{0.5}O₃¹² and Ce_{0.85}Sm_{0.15}O_{1.925}-Sm_{0.6}Sr_{0.4}FeO₃,¹³ by coating Co-containing porous layers on the membrane surface to enlarge the oxygen exchange surface. In our group, we have developed some novel Co-free CO₂-stable dual phase membranes, such as NiFe₂O₄-Ce_{0.9}Gd_{0.1}O_{2-δ} (NF-CG),¹⁴ Fe₂O₃-Ce_{0.9}Gd_{0.1}O_{2-δ} (F-CG)¹⁵ and Ce_{0.9}Pr_{0.1}O_{2-δ}-Pr_{0.6}Sr_{0.4}FeO_{3-δ} (CP-PSF).¹⁶ The CP-PSF membrane shows a good chemical stability under the harsh conditions of the POM reaction and in a CO₂ atmosphere at high temperatures.¹⁶ Thus, cobalt-doping of the PSF phase in the dual phase CP-PSF membrane can enhance the oxygen vacancy concentration in the membrane lattice, which should result in a combination of good CO₂ stability and high oxygen permeability.

In this paper, we present the novel dual phase membrane, 60 wt% Ce_{0.9}Pr_{0.1}O_{2-δ}-40 wt% Pr_{0.6}Sr_{0.4}Fe_{0.5}Co_{0.5}O_{3-δ} (abbreviated as CP-PSFC) prepared *via* a one-pot sol-gel synthesis method.¹⁷ In this dual phase system, the CP phase is mainly for ionic transport, and the PSFC phase for both electronic and ionic transport. The XRD pattern in Fig. 1 shows that after sintering at 1200 °C for 5 h in air, the dual phase CP-PSFC membrane consists of only the cubic fluorite CP phase (space group 225: *Fm3m*) and the orthorhombic distorted perovskite PSFC phase (space group 74: *Imma*). The phase stability of the dual phase CP-PSFC material against CO₂ was evaluated by *in situ* XRD measurements (Fig. S2, ESI†) between 30 and 1000 °C in an atmosphere of 50 vol% CO₂/50 vol% air. No carbonate formation was observed in the *in situ* XRD patterns

^a Institute of Physical Chemistry and Electrochemistry, Leibniz University of Hannover, Callinstr. 3a, D-30167 Hannover, Germany.
E-mail: fangyi.liang@pci.uni-hannover.de; Fax: +49-511-762-19121;
Tel: +49-511-762-2942

^b Department of Chemistry, Princeton University, Princeton, New Jersey 08544, USA

† Electronic supplementary information (ESI) available: Experimental details. See DOI: 10.1039/c3cc47962e

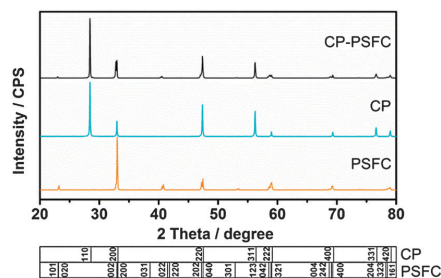


Fig. 1 XRD patterns of the dual phase CP-PSFC membrane, and of the single phases CP and PSFC, all sintered at 1200 °C in air for 5 h.

from 30 to 1000 °C, which is in good agreement with the *in situ* XRD finding in previous reports of the CP-PSF¹⁶ and La_{0.6}Sr_{0.4}Co_{0.8}Fe_{0.2}O_{3-δ}¹⁸ under similar experimental conditions. In this temperature range, the CP phase retains the cubic structure. Moreover, two phase transitions of the PSFC phase from the orthorhombic to the rhombohedral symmetry at ca. 600 °C and from the rhombohedral to the cubic symmetry at ca. 800 °C could be observed. However, the PSF phase without Co in the dual phase CP-PSF powder retains the orthorhombic symmetry under the same conditions.¹⁶ The phase transition from rhombohedral to cubic symmetry at high temperatures is in agreement with the findings for the comparable materials La_{0.6}Sr_{0.4}Co_{0.8}Fe_{0.2}O_{3-δ}¹⁸ and La_{0.6}Ca_{0.4}Co_{0.8}Fe_{0.2}O_{3-δ}.¹⁹ The formation of the cubic structure of the PSFC phase at high temperatures is beneficial for oxygen permeability.^{17,20} Thus, the dual phase CP-PSFC material exhibits a stable co-existence of both the CP and the PSFC phases and a good tolerance against CO₂.

Fig. 2 shows the scanning electron microscopy (SEM), back-scattered SEM (BSEM), and energy-dispersive X-ray spectroscopy (EDXS) images of the dual phase CP-PSFC membrane after sintering at 1200 °C for 5 h in air. SEM (Fig. 2a) indicates that the membrane is dense. In the BSEM (Fig. 2b and c) at different magnifications, the grains of the two phases are well distributed forming a 3-dimensional percolation network with clear grain boundaries, which is beneficial to the oxygen ion and electron transport through the membrane.

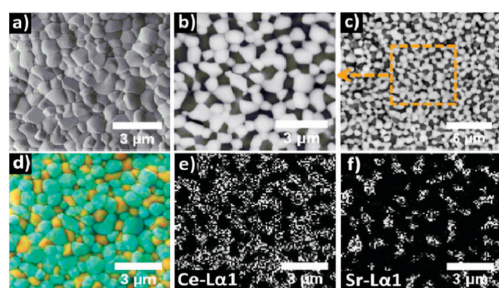


Fig. 2 SEM (a), BSEM (b and c), and EDXS (d–f) images of the dual phase CP-PSFC membrane after sintered at 1200 °C for 5 h in air. In BSEM (b and c) for different magnifications, the dark grains represent PSFC, the light ones CP. Superimpositions of the Pr, Sr, Fe and Co (orange), and Pr and Ce (turquoise) signals have been used in Fig. 2(d). Element distribution of Ce in the CP grains (Fig. 2e) and Sr in the PSFC (Fig. 2f).

The light grains in the BSEM are CP and the dark grains are PSFC since the contribution of the backscattered electrons to the SEM signal intensity is proportional to the atomic number. The grain size of CP in these composite membranes is larger than that of PSFC. The same information about the phase distribution is provided by the EDXS (Fig. 2d–f) of the membrane. Fig. 2d shows the color version EDXS of the membrane where the turquoise color (light in BSEM) is due to overlapping of the Ce and Pr signals, whereas the orange color (dark in BSEM) stems from an average of the Pr, Sr, Fe and Co signals. The EDXS elemental distributions of Ce in the CP grains (Fig. 2e) and of Sr in the PSFC grains (Fig. 2f) indicate the phase separation in the membrane and proof that no intermixing of Ce and Sr between the two phases exists.

The oxygen permeation fluxes through the dual phase CP-PSFC membrane as a function of temperature with pure He and CO₂ as sweep gases are shown in Fig. 3. For both the sweep gases He and CO₂, the oxygen permeation flux increases with increasing temperatures. By increasing the temperatures from 800 to 1000 °C, the oxygen permeation fluxes increase from 0.24 to 1.08 cm³ (STP) min⁻¹ cm⁻² for using He and from 0.11 to 1.01 cm³ (STP) min⁻¹ cm⁻² for using CO₂ as the sweep gas. If pure CO₂ has been used as the sweep gas, the oxygen permeation flux is only slightly lower than in the case when pure He was used as the sweep gas, which is in good agreement with the observations in previous reports.^{13,14,21} The reason for this experimental finding can be attributed to the weaker adsorptive interaction of He in comparison with CO₂ with the membrane surface, as the influence of He on the oxygen exchange reaction is less than that of CO₂.^{12,14,22,23} Furthermore, it is also found that the difference in the oxygen permeation flux between He and CO₂ as sweep gases is larger at lower temperatures and becomes smaller at higher temperatures, which can be ascribed to the decreasing adsorptive interaction with increasing temperatures. In comparison with the Co-free dual phase CP-PSF membrane at 950 and 1000 °C,¹⁶ the oxygen permeation fluxes of the Co-containing dual phase CP-PSFC membrane are increased by approximately a factor of 3, which is a clear indication of an increased concentration of mobile oxygen vacancies by Co-doping, which significantly enhances the oxygen permeability of the PSFC phase.

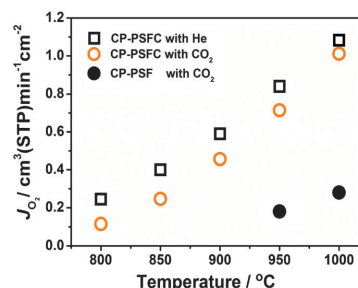


Fig. 3 Oxygen permeation fluxes through the dual phase CP-PSFC and CP-PSF²⁵ membranes as a function of temperature with pure He and CO₂ as sweep gases. Conditions for CP-PSFC: 150 cm³ (STP) min⁻¹ air as the feed gas, 50 cm³ (STP) min⁻¹ He or CO₂ as the sweep gas; membrane thickness: 0.6 mm. Conditions for CP-PSF:¹⁶ 150 cm³ (STP) min⁻¹ air as the feed gas, 30 cm³ (STP) min⁻¹ CO₂ as the sweep gas; membrane thickness: 0.5 mm.

The oxygen permeability of an OTM strongly depends on its composition, the membrane thickness, the coating of the membrane surface (catalytic coating or coating to enlarge the surface, thus enhancing the exchange reaction), and the operation conditions (type of sweep gas, temperature, or the oxygen partial pressure). Table S1 (ESI[†]) contains the oxygen permeation fluxes of several OTMs evaluated with CO₂ as the sweep gas at ca. 950 °C. As shown in Table S1 (ESI[†]), our dual phase CP-PSFC membrane exhibits the highest oxygen permeation flux compared to the other dual phase membranes. It should be noted that the fluxes measured on our dual phase CP-PSFC membrane were obtained for a relatively thick membrane (0.6 mm) without any coating on the membrane surface. It is believed that the oxygen permeability of our CP-PSFC membrane can be further improved by reducing the membrane thickness like a hollow fiber membrane^{23,24} or an asymmetric membrane,²⁵ or by coating for an enlargement of the membrane surface.^{12,13}

Fig. 4 presents the long-term oxygen permeation operation of two dual phase CP-PSFC membranes M1 and M2. For the CP-PSFC membrane M1, when He is used as the sweep gas at 950 °C, the oxygen permeation flux increases slowly during the activation time in the first 10 h. After this activation step, the oxygen permeation flux reaches steady-state with a constant value of 0.84 cm³ (STP) min⁻¹ cm⁻² (inset in Fig. 4). When pure CO₂ was used instead of He as the sweep gas, the oxygen permeation flux only slightly decreased to the lower value of 0.70 cm³ (STP) min⁻¹ cm⁻². This oxygen permeation flux was found to be constant during the whole oxygen permeation operation by using pure CO₂ as the sweep gas at 950 °C for 400 h. When the operation temperature was elevated to 1000 °C, the oxygen permeation flux increased significantly to the higher value of 1.01 cm³ (STP) min⁻¹ cm⁻² and was constant for at least 100 h. Whereas the CP-PSFC membrane M2 shows a phase transition from the rhombohedral to the cubic phase (Fig. S2, ESI[†]) and a fast activation step over 10 h only at the higher temperature of 950 °C, when cooling the CP-PSFC membrane M2 from 950 to 800 °C, a phase transition from the cubic to the orthorhombic phase takes place (Fig. S2, ESI[†]). After this phase transition, a slow activation step takes place over ca. 100 h at the lower

temperature of 800 °C. As a result of (i) the phase transformation, and (ii) the lower permeation temperature, for the CP-PSFC membrane M2 with pure CO₂ as the sweep gas at 800 °C, the oxygen permeation flux decreases slowly from 0.19 to 0.13 cm³ (STP) min⁻¹ cm⁻² in the first 100 h. After this phase transformation and the activation step, the oxygen permeation flux reaches a steady-state for 200 h. For the membranes M1 and M2 after the long-term oxygen permeation operation, no carbonate formation was observed in the XRD patterns (Fig. S3 and S5, ESI[†]). No carbon species enrichment was found at the strontium positions in the EDXS images on the surfaces of the membranes M1 and M2 (Fig. S6 and S7, ESI[†]) and their cross-sections (Fig. S4 and S8, ESI[†]), which excludes SrCO₃ formation. This long-term operations suggest that our dual phase CP-PSFC membrane exhibits an excellent stability in CO₂ and shows a high oxygen permeation performance.

In summary, we have prepared a novel CO₂-stable dual phase 60 wt% Ce_{0.9}Pr_{0.1}O_{2-δ}-40 wt% Pr_{0.6}Sr_{0.4}Fe_{0.5}Co_{0.5}O_{3-δ} (CP-PSFC) membrane with Co-doping of the PSF phase for high oxygen permeability. Cobalt-doping of the PSF phase can enhance the oxygen vacancy concentration in the membrane lattice and stabilize the cubic structure above 800 °C which is beneficial for oxygen permeability. The *in situ* XRD and the long-term operations demonstrate that the CP-PSFC dual phase membrane shows a very good tolerance against CO₂. Moreover, the very high oxygen permeation flux of 0.70 and 1.01 cm³ (STP) min⁻¹ cm⁻² were found to be constant at 950 and 1000 °C during the long-term operation for over at least 400 h. The dual phase CP-PSFC membrane with excellent CO₂ stability and high oxygen permeation performance is a promising membrane material for industrial applications in the oxyfuel process for CO₂ capture.

The EU is thanked for financing the 7th Framework Program of the IP Innovative Catalytic Technologies & Materials for the Next Gas to Liquid Processes (NEXT-GTL). The authors are thankful for the financial support by DFG 147/18-1 and to the Sino-German Center for Promoting Research (GZ 676). The authors thank Prof. Dr Feldhoff for stimulating discussions and F. Steinbach for technical support.

Notes and references

- R. S. Haszeldine, *Science*, 2009, **325**, 1647–1652.
- S. P. S. Badwal and F. T. Ciacchi, *Adv. Mater.*, 2001, **13**, 993–996; Y. Y. Liu, X. Y. Tan and K. Li, *Catal. Rev.: Sci. Eng.*, 2006, **48**, 145–198; J. Sunarso, S. Baumann, J. M. Serra, W. A. Meulenberg, S. Liu, Y. S. Lin and J. C. D. da Costa, *J. Membr. Sci.*, 2008, **320**, 13–41.
- A. Leo, S. Liu and J. C. D. da Costa, *Int. J. Greenhouse Gas Control*, 2009, **3**, 357–367; X. Y. Tan, K. Li, A. Thursfield and I. S. Metcalfe, *Catal. Today*, 2008, **131**, 292–304.
- P. A. Armstrong, D. L. Bennett, E. P. T. Foster and E. E. van Stein, *ITM oxygen for gasification, Proceedings of Gasification Technologies Conference*, Washington, DC, USA, 2004.
- X. F. Zhu, S. M. Sun, Y. Cong and W. S. Yang, *J. Membr. Sci.*, 2009, **345**, 47–52; F. Y. Liang, H. Q. Jiang, T. Schiestel and J. Caro, *Ind. Eng. Chem. Res.*, 2010, **49**, 9377–9384; F. Y. Liang, H. Q. Jiang, H. X. Luo, R. Krieger and J. Caro, *Catal. Today*, 2012, **193**, 95–100.
- H. Q. Jiang, H. H. Wang, F. Y. Liang, S. Werth, T. Schiestel and J. Caro, *Angew. Chem., Int. Ed.*, 2009, **48**, 2983–2986; Y. Y. Wei, W. S. Yang, J. Caro and H. H. Wang, *Chem. Eng. J.*, 2013, **220**, 185–203.
- Z. P. Shao and S. M. Haile, *Nature*, 2004, **431**, 170–173.
- Z. P. Shao, W. S. Yang, Y. Cong, H. Dong, J. H. Tong and G. X. Xiong, *J. Membr. Sci.*, 2000, **172**, 177–188; J. F. Vente, S. McIntosh, W. G. Haije and H. J. M. Bouwmeester, *J. Solid State Electrochem.*, 2006, **10**, 581–588.

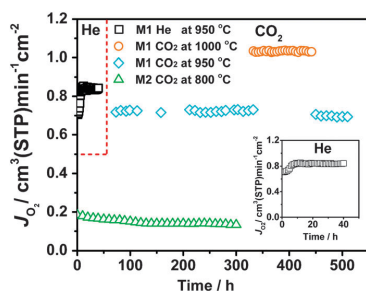


Fig. 4 Long-term oxygen permeation operation of two dual phase CP-PSFC membranes M1 and M2 with pure He or CO₂ as sweep gases at different temperatures. The inset magnifies the oxygen permeation operation with pure He as the sweep gas at 950 °C. Conditions: 150 cm³ min⁻¹ air as the feed gas, 50 cm³ min⁻¹ He or CO₂ as the sweep gas; membrane thickness: 0.6 mm.

- 9 R. Kriegel, R. Kirchseisen and J. Töpfer, *Solid State Ionics*, 2010, **181**, 64–70.
- 10 M. Arnold, H. H. Wang and A. Feldhoff, *J. Membr. Sci.*, 2007, **293**, 44–52; A. Waandich, A. Möbius and M. Müller, *J. Membr. Sci.*, 2009, **337**, 182–187; S. Engels, F. Beggel, M. Modigell and H. Stadler, *J. Membr. Sci.*, 2010, **359**, 93–101.
- 11 B. C. H. Steele, *Curr. Opin. Solid State Mater. Sci.*, 1996, **1**, 684–691.
- 12 X. F. Zhu, H. Y. Liu, Y. Cong and W. S. Yang, *Chem. Commun.*, 2012, **48**, 251–253.
- 13 X. F. Zhu, M. R. Li, H. Liu, T. Y. Zhang, Y. Cong and W. S. Yang, *J. Membr. Sci.*, 2012, **394**, 120–130.
- 14 H. X. Luo, K. Efimov, H. Q. Jiang, A. Feldhoff, H. H. Wang and J. Caro, *Angew. Chem., Int. Ed.*, 2011, **50**, 759–763.
- 15 H. X. Luo, H. Q. Jiang, K. Efimov, F. Y. Liang, H. H. Wang and J. Caro, *Ind. Eng. Chem. Res.*, 2011, **50**, 13508–13517.
- 16 H. X. Luo, H. Q. Jiang, T. Klande, Z. W. Cao, F. Liang, H. H. Wang and J. Caro, *Chem. Mater.*, 2012, **24**, 2148–2154.
- 17 F. Y. Liang, K. Partovi, H. Q. Jiang, H. X. Luo and J. Caro, *J. Mater. Chem. A*, 2013, **1**, 746–751.
- 18 T. Klande, O. Ravkina and A. Feldhoff, *J. Membr. Sci.*, 2013, **437**, 122–130.
- 19 K. Efimov, T. Klande, N. Juditzki and A. Feldhoff, *J. Membr. Sci.*, 2012, **389**, 205–215.
- 20 X. T. Liu, H. L. Zhao, J. Y. Yang, Y. Li, T. Chen, X. G. Lu, W. Z. Ding and F. S. Li, *J. Membr. Sci.*, 2011, **383**, 235–240; X. F. Zhu, H. H. Wang and W. S. Yang, *Chem. Commun.*, 2004, 1130–1131.
- 21 H. X. Luo, H. Q. Jiang, T. Klande, F. Y. Liang, Z. W. Cao, H. H. Wang and J. Caro, *J. Membr. Sci.*, 2012, **423**, 450–458.
- 22 S. M. Fang, C. S. Chen and L. Winnubst, *Solid State Ionics*, 2011, **190**, 46–52; J. E. tenElshof, H. J. M. Bouwmeester and H. Verweij, *Solid State Ionics*, 1996, **89**, 81–92.
- 23 W. Li, T. F. Tian, F. Y. Shi, Y. S. Wang and C. S. Chen, *Ind. Eng. Chem. Res.*, 2009, **48**, 5789–5793.
- 24 W. Li, J. J. Liu and C. S. Chen, *J. Membr. Sci.*, 2009, **340**, 266–271.
- 25 S. Baumann, J. M. Serra, M. P. Lobera, S. Escolastico, F. Schulze-Kueppers and W. A. Meulenberg, *J. Membr. Sci.*, 2011, **377**, 198–205; M. P. Lobera, J. M. Serra, S. P. Foghmoes, M. Sogaard and A. Kaiser, *J. Membr. Sci.*, 2011, **385**, 154–161.

Supporting Information for

A Novel CO₂-Stable Dual Phase Membrane with High Oxygen Permeability

Fangyi Liang, Huixia Luo, Kaveh Partovi, Olga Ravkina, Zhengwen Cao, Yi Liu,
and Jürgen Caro

Published in *Chemical Communications* **2014**, *50*, 2451-2454

Reprinted with permission from *Chemical Communications*.
Copyright (2014) Royal Society of Chemistry.

Cite this: DOI: 10.1039/c0xx00000x

www.rsc.org/xxxxxx

COMMUNICATION

Electronic Supplementary Information (ESI)

Novel CO₂-stable dual phase membrane with high oxygen permeabilityFangyi Liang ^{a*}, Huixia Luo ^b, Kaveh Partovi ^a, Olga Ravkina^a, Zhengwen Cao ^a, Yi Liu ^a, Jürgen Caro ^a^a *Institute of Physical Chemistry and Electrochemistry, Leibniz University of Hannover, Callinstr. 3a
D-30167 Hannover, Germany*^b *Department of Chemistry, Princeton University, Princeton, New Jersey 08544, USA***Electronic Supplementary Information (ESI)****10 Experimental****Synthesis**

The powder samples of the dual-phase material consisting of 60 wt.% Ce_{0.9}Pr_{0.1}O_{2-δ}-40 wt.% Pr_{0.6}Sr_{0.4}Fe_{0.5}Co_{0.5}O_{3-δ} (abbreviated as CP-PSFC) were synthesized via an one-pot sol-gel synthesis method. Aqueous metal nitrate solutions of Ce(NO₃)₃, Pr(NO₃)₃, Sr(NO₃)₂, Fe(NO₃)₃ and Co(NO₃)₂ in their stoichiometric amounts were mixed with ethylene-diamine tetraacetic acid (EDTA) and citric acid in total metal cation : EDTA : citric acid ratio of 1:1:1.5. The pH was kept roughly at 9 by addition of ammonia solution. The precursor was then heated at 120-150 °C under constant stirring for 1 day in air, until a viscous gel was obtained. The gel was pre-calcined at ca. 300 °C to obtain a solid residue. Further calcination of the solid was carried out in oven at 950 °C for 10 h with a heating/cooling rate of 2 °C min⁻¹. The powders were then pressed uniaxially (3 MPa) into disk-shaped pellets in a stainless steel module (18 mm in diameter) and sintered at 1200 °C for 5 h with a heating/cooling rate of 2 °C min⁻¹ under ambient atmosphere and pressure to obtain dense membranes (0.6 mm thick and 16 mm i. d.).

Characterization

The structural properties of the materials were examined by X-ray diffraction (XRD) techniques using a Bruker AXS D8 Advance instrument. Data were collected in a step-scan mode using monochromator-filtered Cu K α radiation at 40 kV and 40 mA, receiving slit of 0.05 mm and count

times of 10 s per step in the 2θ range of 20–80° with intervals of 0.02°. The in-situ XRD measurement between 30 and 1000 °C in an atmosphere of 50 vol% CO₂ / 50 vol% N₂ were conducted in an in-situ cell HTK-1200 N (Anton-Paar) with the heating rate of 12 °C/min and an equilibrium time of 30 min before each measurement. The XRD data were analyzed by TOPAS 4.2 software (Bruker AXS).

5 Scanning Electron Microscopy (SEM), Back-Scattered Electron Microscopy (BSEM) and Energy-Dispersive X-ray Spectroscopy (EDXS) were employed for further examination of the samples using a field emission instrument of the type JEOL JSM-6700-F. In order to investigate the microstructure and the surface properties of the freshly prepared disk membranes, secondary electron (SE) micrographs were obtained at an excitation voltage of 2 kV. The phase composition of the dual-phase membranes and the elemental distribution in the grains were further studied using BSEM and EDXS, respectively, by applying an excitation voltage of 10 kV. The EDX spectra of samples were obtained using an Oxford instrument of the type INCA-300.

Oxygen Permeation

The sintered dual-phase disk membrane was sealed with gold paste (Heraeus, Germany) onto an alumina tube at 950 °C and positioned in an oxygen permeation device depicted in Fig. S1. Synthetic air ($C_{N_2}:C_{O_2} = 80:20$) with a flow rate of 150 cm³ (STP) min⁻¹ was applied on the feed side of the membrane, while He (Linde, 99.999%) and CO₂ (Linde, 99.5%) with a flow rate of 50 cm³ (STP) min⁻¹ were alternatively used as sweep gas. All inlet gas flows were controlled by gas mass flow controllers (Bronkhorst, Germany). The effluent sweep gas mixture was analyzed using an online gas chromatograph (Agilent 6890A). The flow rate of the effluent was determined by a bubble flow meter. The presence of gas leakage could be detected by monitoring the concentration of nitrogen in the effluent.

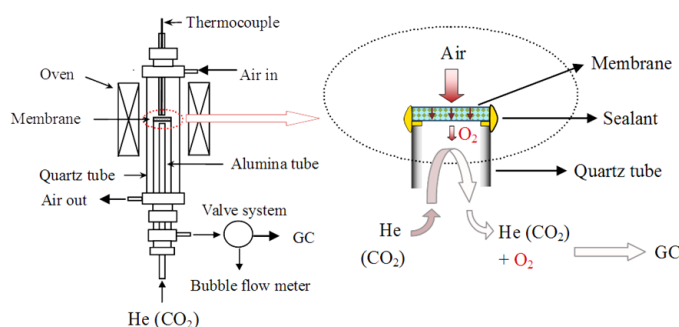


Figure S1. Schematic illustration of the oxygen permeation device.

Table S1. Comparison of the oxygen permeation fluxes of several OTMs with CO₂ as sweep gas at ca. 950 °C.

| Membranes | Catalysts on membrane surface | Thickness / mm | Temperature / °C | $J_{O_2} / \text{cm}^3(\text{STP})\text{min}^{-1}\text{cm}^{-2}$ | Ref. |
|--|--|----------------|------------------|--|-----------|
| Zr _{0.84} Y _{0.16} O _{1.92} -La _{0.8} Sr _{0.2} MnO _{3-δ} | none | 0.16 | 950 | 0.30 | 1 |
| Ce _{0.8} Sm _{0.2} O _{2-δ} -La _{0.8} Sr _{0.2} MnO _{3-δ} | none | 0.3 | 950 | 0.40 | 2 |
| Ce _{0.8} Sm _{0.2} O _{1.9} -SmMn _{0.5} Co _{0.5} O ₃ (SDC+SMC) | both sides coated with SDC+SMC porous layer | 0.5 | 940 | 0.52 | 3 |
| Ce _{0.9} Gd _{0.1} O _{2-δ} -NiFe ₂ O ₄ | air side coated with La _{0.6} Sr _{0.4} CoO ₃ porous layer | 0.5 | 950 | 0.16 | 4 |
| CP-PSF | none | 0.5 | 950 | 0.18 | 5 |
| La _{0.6} Sr _{0.4} Co _{0.8} -Fe _{0.2} O _{3-δ} | none | 1.0 | 900 | 0.1 | 6 |
| CP-PSFC | none | 0.6 | 950 | 0.70 | This work |

- 5 1. W. Li, J. J. Liu and C. S. Chen, *J. Membr. Sci.*, 2009, **340**, 266-271.
2. W. Li, T. F. Tian, F. Y. Shi, Y. S. Wang and C. S. Chen, *Ind. Eng. Chem. Res.*, 2009, **48**, 5789-5793.
3. X. F. Zhu, H. Y. Liu, Y. Cong and W. S. Yang, *Chem. Commun.*, 2012, **48**, 251-253.
4. H. X. Luo, K. Efimov, H. Q. Jiang, A. Feldhoff, H. H. Wang and J. Caro, *Angew. Chem., Int. Ed.*, 2011, **50**, 759-763.
5. H. X. Luo, H. Q. Jiang, T. Klande, Z. W. Cao, F. Liang, H. H. Wang and J. Caro, *Chem. Mater.*, 2012, **24**, 2148-2154.
6. T. Klande, O. Ravkina and A. Feldhoff, *J. Membr. Sci.*, 2013, **437**, 122-130.

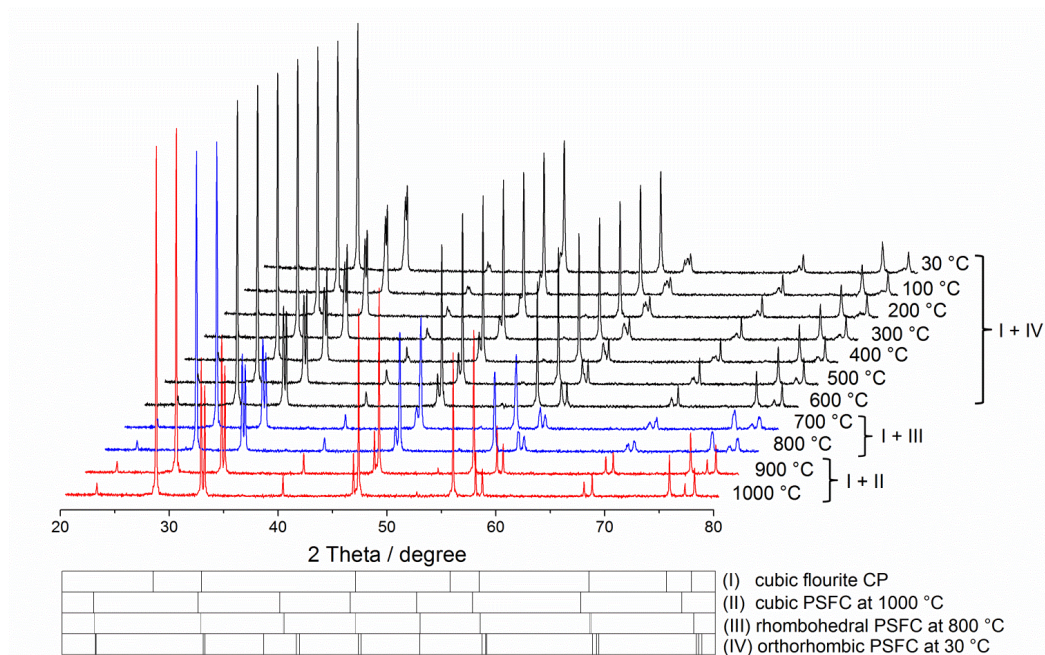


Figure S2. In-situ XRD at given temperatures in an atmosphere of 50 vol% CO₂ / 50 vol% air of the dual phase CP-PSFC powder sintered at 1200 °C in air for 5 h. The calculated Bragg positions for (I) cubic fluorite CP at 1000 °C (s.g., $a=5.503 \text{ \AA}$), (II) cubic PSFC at 1000 °C (s.g., $a=3.930 \text{ \AA}$), (III) rhombohedral PSFC at 800 °C (s.g., $a=5.448 \text{ \AA}$, $c=13.360 \text{ \AA}$), (IV) orthorhombic PSFC at 30 °C (s.g., $a=5.430 \text{ \AA}$, $b=5.450 \text{ \AA}$, $c=7.688 \text{ \AA}$) are given at the bottom of the figures. The total period including equilibration and measurement times was 60 min at a given temperature interval.

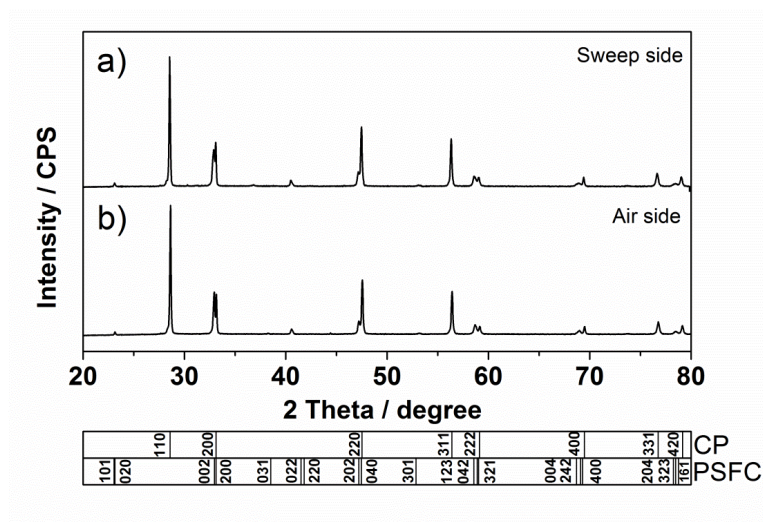


Figure S3. XRD patterns of (a) sweep side and (b) air side of the dual phase CP-PSFC membrane (M1) after Long-term oxygen permeation operation with pure He and CO₂ as sweep gases at 950 °C and 1000 °C for 500 h.

Electronic Supplementary Material (ESI) for Chemical Communications
This journal is © The Royal Society of Chemistry 2014

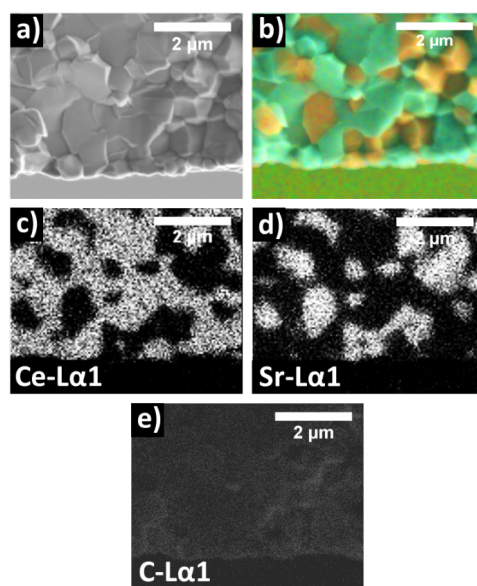


Figure S4 SEM (a) and EDXS (b-e) images of the dual phase CP-PSFC membrane (M1) **cross-section** near the permeate side after long-term oxygen permeation operation with pure He and CO₂ as sweep gases at 950 and 1000 °C for 500 h, as shown in Fig. 4. For the EDXS mapping in Fig. S4 (b), 5 superimpositions of the Pr, Sr, Fe and Co (orange), and Pr and Ce (turquoise) signals have been used. Element distribution of Ce in the CP grains (Fig. S4c), Sr in the PSFC (Fig. S4d), and Carbon (Fig. S4e).

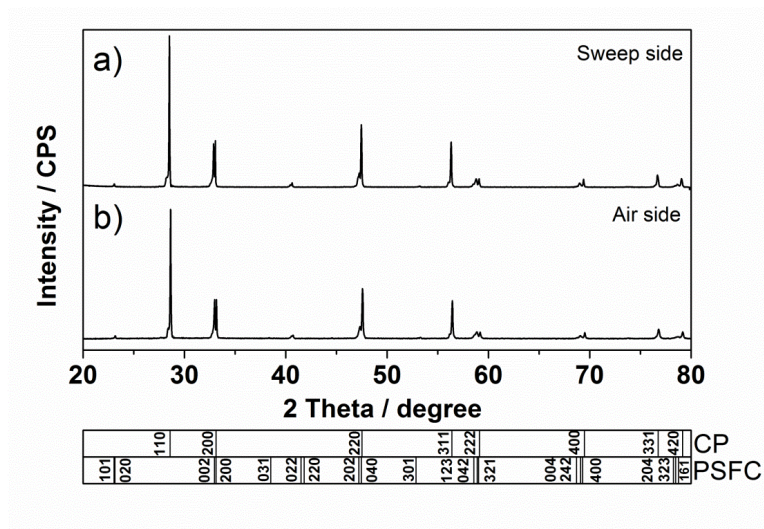


Figure S5. XRD patterns of (a) sweep side and (b) air side of the dual phase CP-PSFC membrane (M2) after Long-term oxygen permeation operation with pure CO₂ as sweep gas at 800 °C for 300 h.

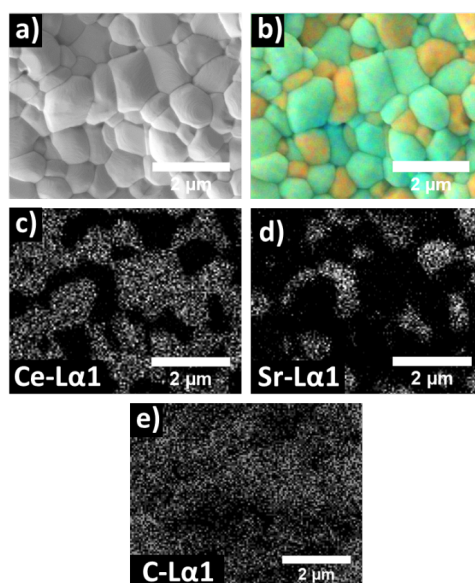


Figure S6. SEM (a) and EDXS (b-e) images of the dual phase CP-PSFC membrane (M2) surface **on the air side** after long-term oxygen permeation operation with pure CO₂ as sweep gas at 800 °C for 5 300 h, as shown in Fig. 4. For the EDXS mapping in Fig. S6 (b), superimpositions of the Pr, Sr, Fe and Co (orange), and Pr and Ce (turquoise) signals have been used. Element distribution of Ce in the CP grains (Fig. S6c), Sr in the PSFC (Fig. S6d), and Carbon (Fig. S6e).

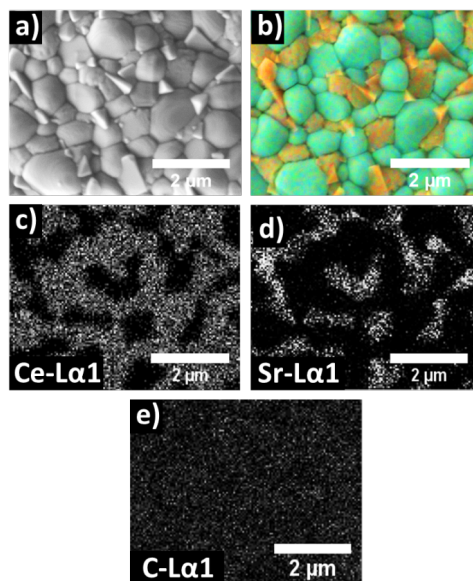


Figure S7. SEM (a) and EDXS (b-e) images of the dual phase CP-PSFC membrane (M2) surface **on the sweep side** after long-term oxygen permeation operation pure CO₂ as sweep gas at 800 °C for 300 h, as shown in Fig. 4. For the EDXS mapping in Fig. S7 (b), superimpositions of the Pr, Sr, Fe and Co 5 (orange), and Pr and Ce (turquoise) signals have been used. Element distribution of Ce in the CP grains (Fig. S7c), Sr in the PSFC (Fig. S7d), and Carbon (Fig. S7e).

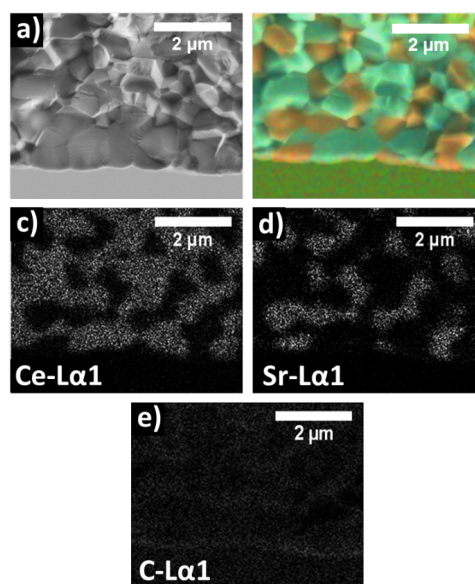


Figure S8. SEM (a) and EDXS (b-e) images of the dual phase CP-PSFC membrane (M2) **cross-section** near the permeate side after long-term oxygen permeation operation with pure CO₂ as sweep gas at 800 °C for 300 h, as shown in Fig. 4. For the EDXS mapping in Fig. S8 (b), superimpositions of the Pr, Sr, Fe and Co (orange), and Pr and Ce (turquoise) signals have been used. Element distribution of Ce in the CP grains (Fig. S8c), Sr in the PSFC (Fig. S8d), and Carbon (Fig. S8e).

Chapter 5

High-Flux Co-Free Dual-Phase Membranes for Oxyfuel Concept

5.1. Summary

Despite high oxygen permeation qualities of Co-containing membranes, whether in form of single-phase perovskites or as dual-phase compositions, a number of disadvantages associated with these materials, imply the necessity of the development of Co-free OTMs for industrial applications. Some of the major issues regarding the incorporation of Co in OTMs were briefly discussed in Section 1.3.1.

The present chapter covers some possible doping strategies to further enhance the oxygen permeation performance of Co-free MIECs, while retaining a reasonable CO₂ resistivity under the practice-relevant conditions.

Section 5.2. investigates the effect of Al-doping at the *B*-site of the perovskite phase, as well as increasing the Sr content of the *A*-site by 10 at.% in the dual-phase composition 40 wt.% Nd_{1-x}Sr_xAl_{0.2}Fe_{0.8}O_{3-δ}- 60 wt.% Ce_{1-y}Nd_yO_{2-δ} (NSAF-CN). Partial substitution of Fe³⁺/Fe⁴⁺ for Al³⁺ at the *B*-site not only increased the oxygen non-stoichiometry-related permeation fluxes, but also resulted in the modification of the perovskite structure. The main purpose of this study was to enhance the oxygen permeation performance of the membrane at the expense of reduced electrical conductivity. The high-temperature DC conductivity measurements confirmed the achievement of this objective.

Another plausible doping strategy involves introduction of Cu in the perovskite phase of a dual-phase MIEC, which is pursued in Section 5.3. For this purpose, the dual-phase material with the composition 40 wt.% Sm_{1-x}Sr_xFeO_{3-δ}- 60 wt.% Ce_{0.8}Sm_{0.2}O_{2-δ} was selected. The phase structure and surface morphology of the membranes were studied by XRD, SEM, BSEM and EDXS techniques. The preliminary results of the material with low Sr content revealed that 20 at.% Cu

could not be fully accommodated at the *B*-site, due to its large ion size. However, it was found that increasing the Sr content could eliminate the segregated CuO particles, by increasing the perovskite unit cell volume. Both membranes exhibited very good oxygen permeation properties under CO₂ sweeping and were highly stable at 1000 and 950 °C for more than 200 h.

5.2. Novel CO₂-Tolerant Al-Containing Membranes for High-Temperature Oxygen Separation

Kaveh Partovi, Michael Bittner, and Jürgen Caro

Published in Journal of Materials Chemistry A **2015**, 3, 24008-24015.

Reprinted from (*J. Mater. Chem. A* **2015**, 3, 24008-24015) with permission from The Royal Society of Chemistry.



Cite this: *J. Mater. Chem. A*, 2015, **3**, 24008

Received 16th June 2015
Accepted 2nd November 2015

DOI: 10.1039/c5ta04405g
www.rsc.org/MaterialsA

Novel CO₂-tolerant Al-containing membranes for high-temperature oxygen separation

Kaveh Partovi,* Michael Bittner and Jürgen Caro

Novel dual-phase oxygen-transporting membranes with compositions 40 wt% Nd_{0.6}Sr_{0.4}Al_{0.2}Fe_{0.8}O_{3-δ}-60 wt% Ce_{0.9}Nd_{0.1}O_{2-δ} (NSAF6428-CN91) and 40 wt% Nd_{0.5}Sr_{0.5}Al_{0.2}Fe_{0.8}O_{3-δ}-60 wt% Ce_{0.8}Nd_{0.2}O_{2-δ} (NSAF5528-CN82) were successfully synthesized *via* a one-pot sol-gel method. The oxygen permeation performance and the structural properties of the membranes could be simultaneously improved owing to Al doping of the perovskite phase. The newly developed dense ceramic membranes (0.6 mm thick) displayed long-term stable oxygen permeation fluxes of 0.31 and 0.51 cm³ min⁻¹ cm⁻² under an air/CO₂ oxygen partial pressure gradient at 950 °C for NSAF6428-CN91 and NSAF5528-CN82, respectively. The NSAF6428-CN91 showed a stable oxygen flux of 0.15 cm³ min⁻¹ cm⁻² at 900 °C for 100 h, without any deterioration of the microstructure under pure CO₂ sweeping.

Introduction

Oxygen-transporting membranes (OTMs) based on mixed ionic-electronic conducting oxides (MIECs) have been extensively studied for a wide variety of applications, such as oxygen separation from air,¹⁻³ as membrane reactors for the conversion of hydrocarbons to value-added products,⁴⁻⁸ or as cathode materials for solid oxide fuel cells.^{9,10} In recent years, OTMs have attracted increasing attention for the application in power plants adopting oxyfuel concept for CO₂ capture, as a cost-efficient replacement for the traditional cryogenic air separation units.¹¹⁻¹³ The oxyfuel concept is based on utilization of high-purity oxygen instead of air for fuel combustion in power plants, thus facilitating carbon capture and storage (CCS) and minimizing the NO_x emissions. In order to control the combustion flame temperature, the combustion gas is partly diluted with the effluent CO₂. Therefore, the candidate MIECs for the oxyfuel concept should meet at least two main requirements: high oxygen permeability and good thermochemical stability against CO₂ and other corrosive gases, such as SO₂, as well as reducing agents such as methane.¹⁴⁻¹⁶ However, the most promising MIECs in terms of oxygen permeability are single phase perovskite-type oxides, mainly Ba_{1-x}Sr_xCo_{1-y}Fe_yO_{3-δ} and Ln_{1-x}Sr_xCo_{1-y}Fe_yO_{3-δ} (Ln = La, Pr, Sm, etc.), containing alkaline earth metals Ba and Sr at the A-site of the perovskite structure ABO₃ and Co at the perovskite's B-site.¹⁷⁻²² The presence of A-site Ba and Sr leads to the degradation of the membrane permeation performance in CO₂-rich environments, due to formation of BaCO₃ and SrCO₃ on the CO₂-exposed outer surface layer of the membrane, thus inhibiting the oxygen surface exchange reaction.²³⁻²⁶

Institute of Physical Chemistry and Electrochemistry, Leibniz University of Hannover, Callinstr. 3a, D-30167 Hannover, Germany. E-mail: kaveh.partovi@pci.uni-hannover.de

The concept of dual-phase composite materials was developed to enhance the thermochemical stability and mechanical properties of the single-phase perovskite-type OTMs. SmMn_{0.5}-Co_{0.5}O₃-Ce_{0.8}Sm_{0.2}O_{1.9},²⁷ La_{0.9}Sr_{0.1}FeO_{3-δ}-Ce_{0.8}Sm_{0.2}O_{2-δ},²⁸ Pr_{0.6}Sr_{0.4}FeO_{3-δ}-Ce_{0.9}Pr_{0.1}O_{2-δ},²⁹ and Pr_{0.6}Sr_{0.4}Co_{0.5}Fe_{0.5}O_{3-δ}-Ce_{0.9}Pr_{0.1}O_{2-δ},³⁰ are some examples of dual-phase compositions based on an ionic conducting fluorite-type phase, mainly doped ceria, and a mixed-conducting phase, such as perovskite oxides. However, despite their improved stability in CO₂-containing environments, dual-phase membranes exhibit lower oxygen permeability compared to single-phase membranes.

Recently, a CO₂-stable reduction-tolerant dual-phase material with the composition 40 wt% Nd_{0.6}Sr_{0.4}FeO_{3-δ}-60 wt% Ce_{0.9}-Nd_{0.1}O_{2-δ} (abbreviated as NSF64-CN91) was developed by our group.³¹ Incorporation of Al at the B-site of the perovskite phase has been previously reported to increase the thermochemical stability of the membranes, also under reducing atmospheres,^{32,33} correlating with reduced chemical and thermal expansion coefficients.^{34,35} In this paper, we report enhanced oxygen permeability and structural improvement of NSF64-CN91 by partial substitution of Fe for Al at the B-site of the perovskite phase. Furthermore, the effect of higher Sr content and increased Nd doping of the fluorite phase on the CO₂ stability and oxygen permeability of the newly developed membranes 40 wt% Nd_{0.6}Sr_{0.4}Al_{0.2}Fe_{0.8}O_{3-δ}-60 wt% Ce_{0.9}Nd_{0.1}O_{2-δ} (NSAF6428-CN91) and 40 wt% Nd_{0.5}Sr_{0.5}Al_{0.2}Fe_{0.8}O_{3-δ}-60 wt% Ce_{0.8}Nd_{0.2}O_{2-δ} (NSAF5528-CN82) are investigated.

Experimental

The dual-phase materials with compositions of 40 wt% Nd_{0.6}-Sr_{0.4}Al_{0.2}Fe_{0.8}O_{3-δ}-60 wt% Ce_{0.9}Nd_{0.1}O_{2-δ} (abbreviated as NSAF6428-CN91) and 40 wt% Nd_{0.5}Sr_{0.5}Al_{0.2}Fe_{0.8}O_{3-δ}-60 wt%

cation. The ionic radii of the 6-fold coordinated B-site species are listed in Table 1.

In the case of NSF, the tilting of the BO_6 octahedra occurs due to the smaller cation size of Nd, resulting in an orthorhombic distortion of the perovskite structure. The trend of increasing orthorhombic distortion with decreasing A-site cation size has been previously reported for LnNiO_3 ($\text{Ln} = \text{La}, \text{Pr}, \text{Nd}, \text{Sm}$) perovskites,⁴¹ which can also be represented as a negative deviation of the Goldschmidt's tolerance factor t from unity:⁴²

$$t = \frac{r_A + r_O}{\sqrt{2}(r_B + r_O)} \quad (1)$$

where r_A , r_B , and r_O refer to the ionic radii of the A-site cation, B-site cation and oxygen, respectively. Thus, partial substitution of the larger Fe cation for the smaller Al cation is expected to have slightly increased the tolerance factor, resulting in a cubic perovskite structure, which facilitates the isotropic bulk diffusion of oxygen ion. Furthermore, a small shift of the NSAF perovskite's main reflection position towards higher diffraction angles compared to that of the NSF perovskite, confirms a slight shrinkage of the perovskite's unit cell, due to partial substitution of Fe for Al. Table 2 lists the calculated unit cell parameters of the sintered dual-phase membranes at room temperature.

Electrical conductivity

Fig. 2 shows temperature-dependent total electrical conductivity of NSF64–CN91, NSAF6428–CN91, and NSAF5528–CN82 compositions measured by a DC four-probe method in ambient air. The total electrical conductivity in mixed ionic–electronic conducting perovskite-type oxides, such as NSF and NSAF, can principally be attributed to the electronic conductivity, which is two orders of magnitude higher than the ionic conductivity. The electronic conduction is mediated by a thermally activated small-polaron hopping mechanism over B–O–B conduction pairs, consisting of overlapped 3d-orbitals of the B-site transition metal cations and the 2p-orbitals of the oxygen ion.^{44,45} As can be seen in Fig. 2, the electronic conductivity of the compositions increases with increasing temperature to a maximum at T_{max} , indicating a semi-conductor behavior. Above this temperature the electronic conductivity decreases with increasing temperature, corresponding to the onset of oxygen release from the lattice. The decrease in electronic conduction above T_{max} results from increasing concentration of oxygen vacancies, as well as decreasing concentration of charge carriers.^{46,47}

Table 1 Ionic radii of the 6-fold coordinated B-site species of the NSAF perovskite phase⁴³

| Cation | Radius (Å) |
|------------------------------------|------------|
| Al^{3+} | 0.535 |
| Fe^{3+} (HS) ^a | 0.645 |
| Fe^{3+} (LS) ^b | 0.55 |
| Fe^{4+} | 0.585 |

^a High spin. ^b Low spin.

Table 2 Calculated lattice parameters of the related phase components after sintering

| Phase component | Crystal symmetry | a (Å) | b (Å) | c (Å) |
|-----------------|-------------------------|---------|---------|---------|
| NSF | Orthorhombic ($Imma$) | 5.492 | 7.766 | 5.497 |
| NSAF6428 | Cubic ($Pm\bar{3}m$) | 3.864 | — | — |
| NSAF5528 | Cubic ($Pm\bar{3}m$) | 3.867 | — | — |
| CN91 | Cubic ($Fm\bar{3}m$) | 5.438 | — | — |
| CN82 | Cubic ($Fm\bar{3}m$) | 5.454 | — | — |

Accordingly, upon introduction of 20 at% Al^{3+} to the B-site of the perovskite phase in NSF64–CN91, lower conductivities are observed for NSAF6428–CN91 as the concentration of mixed-valence $\text{Fe}^{3+}/\text{Fe}^{4+}$ is decreased, which is consistent with previous studies.^{48,49}

Furthermore, increasing the concentration of the acceptor dopant Sr^{2+} at the A-site of the perovskite in NSAF6428–CN91 results in higher concentration of p-type charge carriers.⁵⁰ Consequently, higher conductivities are observed for

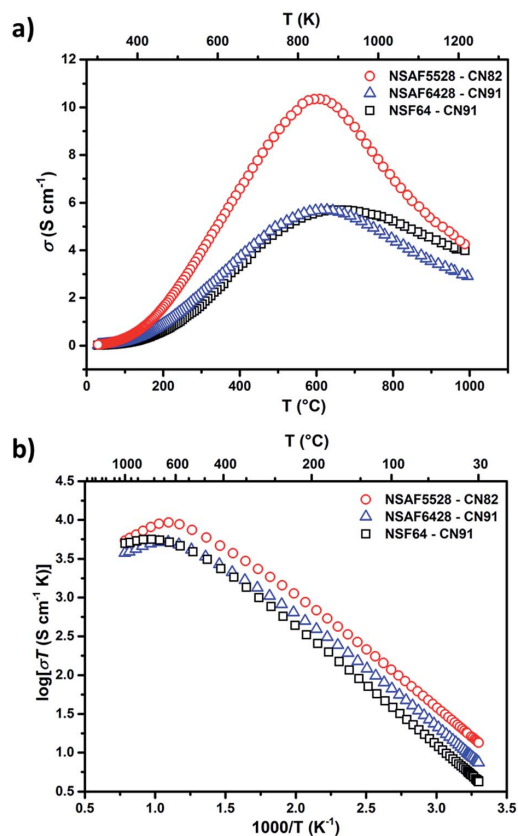


Fig. 2 Electrical conductivities of NSF64–CN91, NSAF6428–CN91, and NSAF5528–CN82 in air: (a) as a function of temperature, (b) represented as Arrhenius plots.

NSAF5528–CN82, compared to NSF64–CN91 and NSAF6428–CN91. However, due to increased loss of oxygen above T_{\max} a faster trend of decreasing conductivity is also observed for NSAF5528–CN82.

Membrane microstructure

The surface microstructure and elemental distribution of the membranes were studied by SEM and EDXS analysis. The SEM, BSEM and EDXS images of the sintered NSAF6428–CN91 and NSAF5528–CN82 are presented in Fig. 3 and 4, respectively. The SEM micrographs of the membrane surface show densely packed grains (Fig. 3a and 4a). The membrane surface was free of cracks and no additional particles could be observed. As can be seen in the BSEM images of the same spots (Fig. 3b and 4b), the grains of the perovskite phase NSAF (dark grains) and the fluorite phase CN (light grains) are uniformly distributed. The percolation network formed by the two phases can be more clearly observed in the EDXS mapping images showing separate Fe-rich (Fig. 3c and 4c) and Ce-rich (Fig. 3d and 4d) phases, corresponding to the perovskite and fluorite grains, respectively.

Oxygen permeation performance

Oxygen permeation performance of the dual-phase membranes NSAF6428–CN91 and NSAF5528–CN82 was studied using pure He and pure CO₂ as sweep gases at temperatures ranging from 800 to 1000 °C. In Fig. 5, temperature-dependent oxygen permeation fluxes of the newly developed NSAF–CN membranes (0.6 mm thick) are compared to those of NSF–CN membrane, previously reported by our group under the same conditions.³¹ As can be seen in Fig. 5, partial substitution of Fe with Al has resulted in higher oxygen fluxes for NSAF6428–CN91 compared to NSF64–CN91 at all measured temperatures and with both He and CO₂ as sweep gases. This finding is in good agreement with

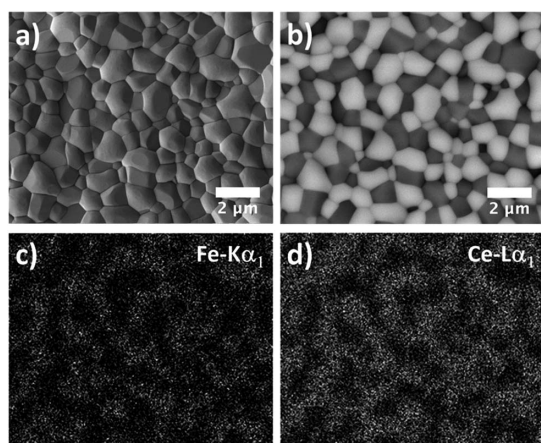


Fig. 3 Microstructure of NSAF6428–CN91 membrane sintered at 1400 °C for 5 h: (a) SEM micrograph, (b) BSEM micrograph, (c & d) elemental distribution of the area shown in panel (a) using EDXS analysis.

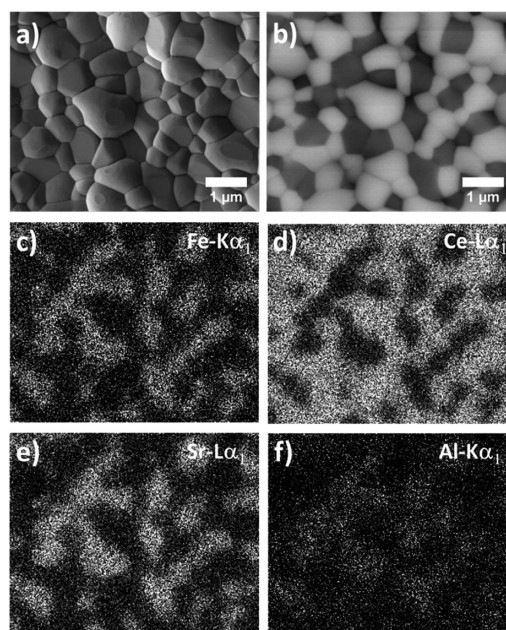


Fig. 4 Microstructure of NSAF5528–CN82 membrane sintered at 1400 °C for 5 h: (a) SEM micrograph, (b) BSEM micrograph, (c–f) elemental distribution of the area shown in panel (a) using EDXS analysis.

previous studies conducted on perovskite membranes, which reported improved oxygen permeability and phase stability by limited Al doping in the Fe-sublattice.^{49,51} At 950 °C, oxygen permeation fluxes of 0.26 and 0.21 cm³ min⁻¹ cm⁻² were reported for NSF64–CN91 with He and CO₂, respectively, whereas the oxygen fluxes of 0.42 and 0.31 cm³ min⁻¹ cm⁻² were measured on the NSAF6428–CN91 membrane at the same temperature and under the same conditions. The enhanced permeation fluxes of NSAF6428–CN91 can be attributed to various effects, such as increased concentration of oxygen vacancies as a result of lower average oxidation state of the B-site cations by partial substitution of Fe³⁺/Fe⁴⁺ for Al³⁺. Moreover, bulk diffusion of the oxygen ion is expected to be facilitated due to the higher symmetry of the cubic structure of the perovskite phase achieved by the introduction of smaller Al cation, as previously discussed. It should be noted, that the observed enhanced oxygen permeability of the Al-doped composition is substantially related to the initially higher oxygen non-stoichiometry, due to the lower average valence state of the Al-doped B-sublattice. According to Martynczuk *et al.*, Al³⁺ predominantly replaces Fe⁴⁺ at the B-sublattice rather than Fe³⁺, which also enhances the effect of oxygen non-stoichiometry.⁵¹ As shown in Fig. 6, the thermogravimetric analysis of the samples reveals that partial substitution of Fe for 20 at% Al does not significantly affect the thermally activated oxygen release from the lattice. Furthermore, increasing the amount of the acceptor dopant Sr²⁺, results in a higher rate of reduction-induced oxygen release for NSAF5528–CN82.

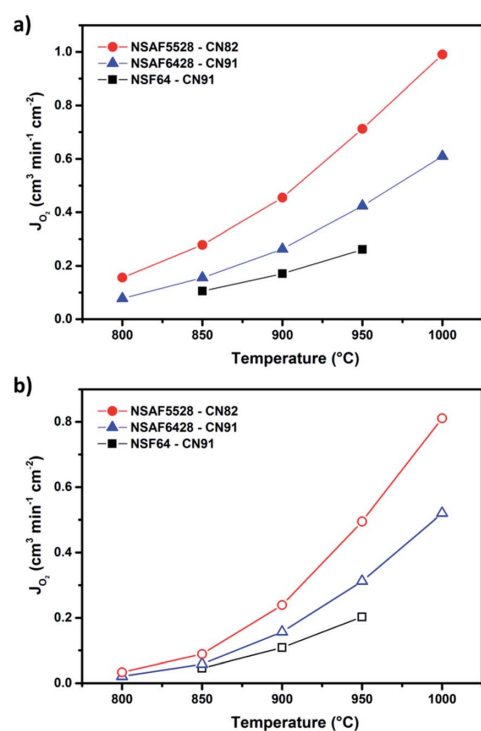


Fig. 5 Temperature-dependent oxygen permeation fluxes of NSAF-CN and NSF-CN³¹ membranes with: (a) He as sweep gas (solid symbols), and (b) CO₂ as sweep gas (open symbols). Feed side: 150 cm³ min⁻¹ synthetic air. Sweep side: 49 cm³ min⁻¹ He (a) or CO₂ (b) + 1 cm³ min⁻¹ Ne as internal standard. Membrane thickness: 0.6 mm.

In general, the overall oxygen permeation flux of a mixed-conducting membrane can be described by Wanger's theory of ambipolar conductivity.⁵² Correspondingly, in a perovskite-type

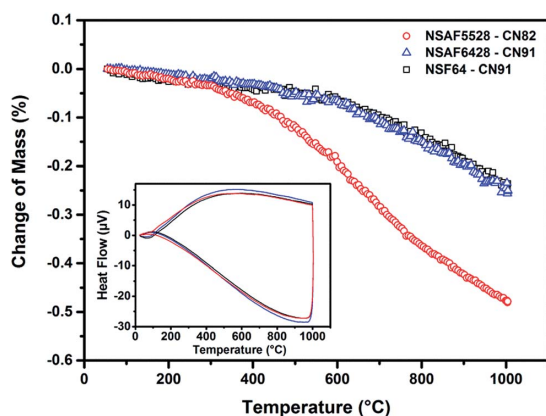


Fig. 6 TGA/DTA results of the dual-phase composites NSF-CN and NSAF-CN in synthetic air, flow of synthetic air: 20 cm³ min⁻¹, heating/cooling rate: 10 °C min⁻¹. Inset: DTA results of the samples.

mixed ionic–electronic conductor, where the ionic conductivity is about two orders of magnitude lower than the electronic conductivity, the oxygen permeation flux is mainly controlled by the ionic conductivity. Therefore, a slight decrease in electrical conductivity has no significant effect on the overall oxygen permeation flux.

In summary, it can be concluded from the electrical conductivity results and the oxygen permeation measurements, that substitution of the B-site Fe for 20 at% Al has enhanced the oxygen permeability of the membrane at the cost of lower conductivity at temperatures above T_{max} , where the maximum electrical conductivity was observed.

Nevertheless, the highest oxygen permeation fluxes were observed for NSAF5528-CN82 with 0.71 and 0.50 cm³ min⁻¹ cm⁻² at 950 °C with He and CO₂, respectively. The optimized oxygen permeability of NSAF5528-CN82 is attributed to increased oxygen non-stoichiometry in both fluorite and perovskite phases, resulted from 10 at% increase of Nd doping of the fluorite-type ceria and 10 at% higher Sr content at the A-site of the perovskite phase. However, increased amount of Sr could strongly compromise the CO₂ tolerance of the composition, as has been reported for single-phase perovskite membranes.^{25,53,54} In order to investigate the effect of increased Sr content on the CO₂ stability of the membranes, long-term oxygen permeation tests were conducted on NSAF6428-CN91 and NSAF5528-CN82 membranes under air/CO₂ oxygen partial pressure gradients. The results of long-term oxygen permeation measurements under air/He and air/CO₂ gradients are shown in Fig. 7. Both membranes show stable oxygen fluxes under air/He oxygen partial pressure gradient at 1000 °C. The permeation fluxes under air/CO₂ oxygen partial pressure gradient display good long-term CO₂ stability at 1000 and 950 °C. An Ellingham diagram of collective data regarding thermodynamic stability of SrCO₃ in varying partial pressures of CO₂,⁵⁵ predicts a decomposition temperature of about 1084 °C (1357 K) under a CO₂ partial pressure of 1 atm. However, this consideration is based on the decomposition of pure SrCO₃ to SrO and CO₂. In case of Sr-containing perovskites, such as NSAF, lower decomposition temperature of SrCO₃ are expected, due to the negative stabilization energy of the perovskite structure,⁵⁶ and a high content of Nd at the A-site, that possesses higher stability against carbonate formation. The observation of stable oxygen fluxes at 1000 and 950 °C for CO₂-swept membranes is in accordance with the above statements. However, at 900 °C the NSAF6428-CN91 membrane with 10 at% lower content of Sr displays higher stability of oxygen fluxes in CO₂, compared to NSAF5528-CN82. For the NSAF6428-CN91 membrane stable oxygen fluxes of approx 0.15 cm³ min⁻¹ cm⁻² were maintained for 100 h, whereas oxygen permeation fluxes of the NSAF5528-CN82 membrane gradually decreased from 0.24 to 0.19 cm³ min⁻¹ cm⁻² in a 130 h course.

The phase composition of the membranes' feed and the sweep sides was studied using XRD. As can be seen in Fig. 8, the phase structures of both membranes were maintained after long-term permeation tests under air/CO₂ oxygen partial pressure gradients. The XRD analysis of the spent membranes

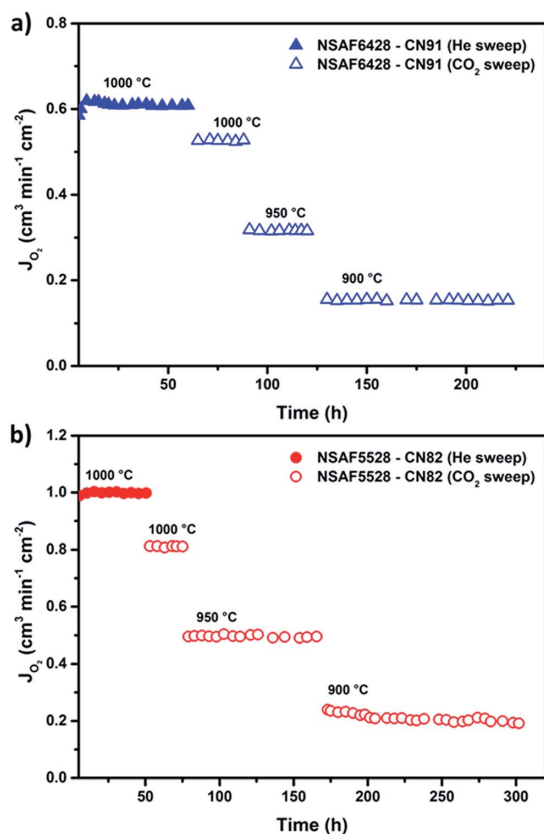


Fig. 7 Long-term oxygen permeation fluxes of: (a) NSAF6428–CN91, and (b) NSAF5528–CN82 membranes. Feed side: $150 \text{ cm}^3 \text{ min}^{-1}$ synthetic air. Sweep side: $49 \text{ cm}^3 \text{ min}^{-1}$ He (solid symbols) or CO_2 (open symbols) + $1 \text{ cm}^3 \text{ min}^{-1}$ Ne as internal standard. Membrane thickness: 0.6 mm. (XRD and SEM of the membranes after permeation shown in Fig. 8 and 9).

revealed no evidence of any carbonate formation or other additional phases on the membranes surface, despite CO_2 exposures of $>100 \text{ h}$ for each membrane.

Subsequently, the microstructure of the spent membranes was analyzed using SEM. Fig. 9 shows the SEM micrographs of the feed and the sweep sides of the spent membranes. The microstructure of feed sides of both membranes was found to be unchanged and free of cracks or additional phases (Fig. 9a and c), which is in accordance with the XRD measurements shown in Fig. 8. On the CO_2 -swept sides of both membranes (Fig. 9b and d), some superficial etching of the grains of the perovskite phase could be observed. In case of NSAF5528–CN82, the etching patterns were more significant, which is principally related to the formation of SrCO_3 at the lower temperature of $900 \text{ }^\circ\text{C}$ for a dwelling time of 130 h. Accordingly, the higher CO_2 reactivity of the NSAF5528–CN82 membrane material due to its higher Sr content explains the slight decrease in oxygen permeation flux of this membrane, shown in Fig. 7b. However, the SEM analysis of the cross-section of the spent NSAF5528–

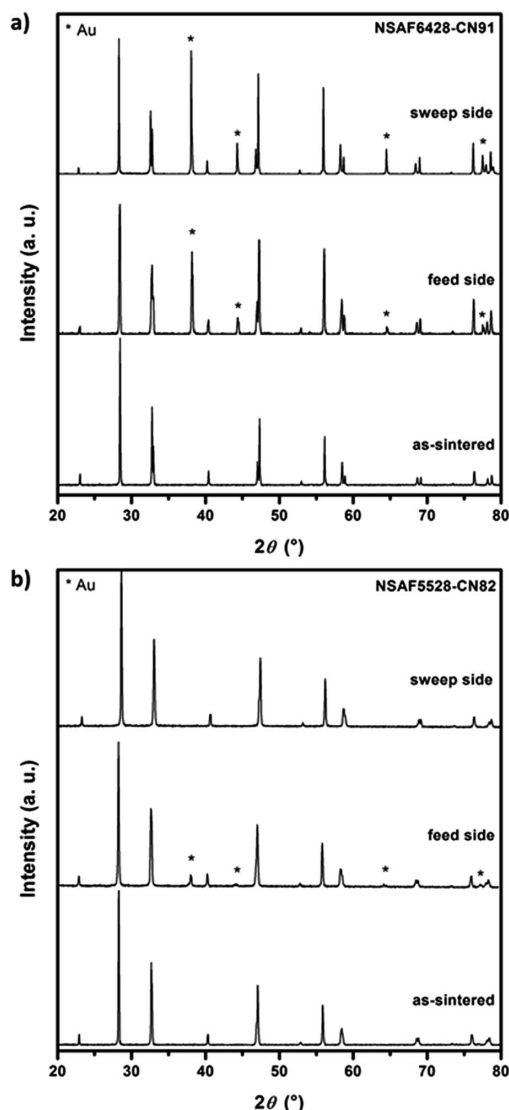


Fig. 8 Room temperature XRD patterns of: (a) NSAF6428–CN91, and (b) NSAF5528–CN82 membranes, as-sintered (bottom), the feed side (middle), and the sweep side (top) of the spent membrane after long-term permeation measurements (shown in Fig. 7). The reflection positions of gold originating from the sealing paste are marked with asterisk (*). (SEM images shown in Fig. 9).

CN82 membrane, shown in Fig. 10, confirmed that the etching of the perovskite grains was limited to the surface layer of the membrane's CO_2 -swept side and the integrity of the grains in the bulk was completely maintained. Consequently, the oxygen permeation flux is expected to reach a steady state, after the carbonate formation reaction ($\text{Sr}^{2+} + \text{CO}_3^{2-} \rightleftharpoons \text{SrCO}_3$) is limited by a relative depletion of Sr from the surface layer of the perovskite grains.

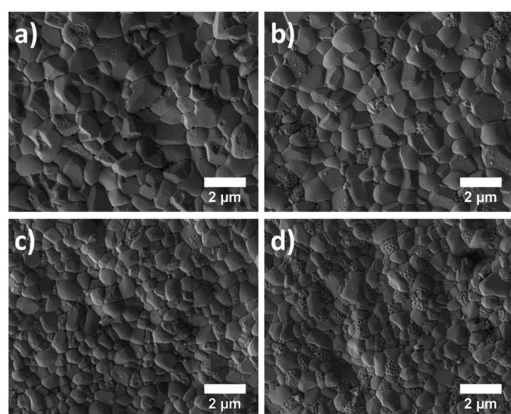


Fig. 9 SEM micrographs of the surface of the spent membranes after the permeation tests (shown in Fig. 7): (a) feed side of NSAF6428-CN91, (b) sweep side of NSAF6428-CN91, (c) feed side of NSAF5528-CN82, (d) sweep side of NSAF5528-CN82. (XRD patterns are shown in Fig. 8).

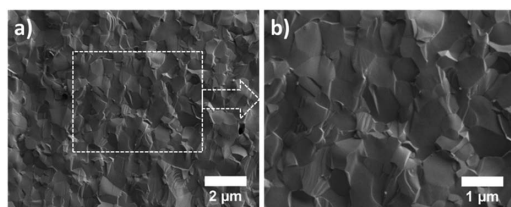


Fig. 10 SEM micrographs of NSAF5528-CN82 membrane cross-section after long-term permeation measurements under air/CO₂ oxygen partial pressure gradient (shown in Fig. 7): (a) packed grains close to the sweep side of the membrane, (b) magnification of area shown in (a).

Conclusions

The newly developed membranes NSAF6428-CN91 and NSAF5528-CN82 exhibited higher oxygen permeation fluxes compared to a similar composition containing only Fe at the B-site of the perovskite phase. Partial substitution of Fe³⁺/Fe⁴⁺ for smaller Al³⁺ resulted in a higher oxygen vacancy concentration, due to the lower oxidation state of the B-site cations, and changed the crystal symmetry of the perovskite from orthorhombic to cubic at room temperature, thus facilitating isotropic bulk diffusion of the oxygen ions in the lattice.

Simultaneous increase in the perovskite's Sr content and the Nd doping of the fluorite phase resulted in higher oxygen permeation fluxes, due to increased oxygen non-stoichiometry. Both membranes showed very good long-term stability at 950 and 1000 °C, with pure CO₂ as the sweeping gas. At 900 °C, NSAF6428-CN91 showed a stable oxygen flux for 100 h under air/CO₂ oxygen partial pressure gradient, whereas NSAF5528-CN82 with 10 at% more Sr content exhibited a slight decrease in the permeation flux over 130 h. The SEM analysis of the surface

of the membranes revealed no deterioration of the microstructure, apart from some minor etching patterns on the surface of the perovskite grains. In summary, the newly developed membranes showed high oxygen permeability and good CO₂ tolerance, for application in CO₂-rich environments, such as air separation units for CO₂ capture by oxyfuel concept.

Acknowledgements

The authors greatly acknowledge the financial support by DFG (Ca 147/18-1) and the Sino-German Centre for Research Promotion (GZ676 and GZ911). Prof. Dr C. H. Rüschler is gratefully acknowledged for the TGA/DTA measurements. Frank Steinbach is thanked for technical support.

Notes and references

- H. J. M. Bouwmeester and A. J. Burggraaf, in *Fundamentals of Inorganic Membrane Science and Technology*, ed. A. J. Burggraaf and L. Cot, Elsevier Science B. V., Amsterdam, The Netherlands, 1996, ch. 10, pp. 435–528.
- U. Balachandran, B. Ma, P. S. Maiya, R. L. Mieville, J. T. Dusek, J. J. Picciolo, J. Guan, S. E. Dorris and M. Liu, *Solid State Ionics*, 1998, **108**, 363.
- F. Y. Liang and J. Caro, in *Membrane Engineering for the Treatment of Gases*, ed. E. Drioli and G. Barbieri, Royal Society of Chemistry, 2011, vol. 2, pp. 192–221.
- J. E. ten Elshof, H. J. M. Bouwmeester and H. Verweij, *Appl. Catal., A*, 1995, **130**, 195.
- J. Caro, K. J. Caspary, C. Hamel, B. Hoting, P. Koelsch, B. Langanke, K. Nassauer, T. Schiestel, A. Schmidt, R. Schomaecker, A. Seidel-Morgenstern, E. Tsotsas, I. Voigt, H. H. Wang, R. Warsitz, S. Werth and A. Wolf, *Ind. Eng. Chem. Res.*, 2007, **46**, 2286.
- H. Q. Jiang, Z. W. Cao, S. Schirrmeister, T. Schiestel and J. Caro, *Angew. Chem., Int. Ed.*, 2010, **49**, 5656.
- X. F. Zhu, Q. Li, Y. He, Y. Cong and W. Yang, *J. Membr. Sci.*, 2010, **360**, 454.
- H. H. Wang, C. Tablet, T. Schiestel, S. Werth and J. Caro, *Catal. Commun.*, 2006, **7**, 907.
- Z. P. Shao and S. M. Haile, *Nature*, 2004, **431**, 170.
- K. Huang, J. Wan and J. B. Goodenough, *J. Mater. Sci.*, 2001, **36**, 1093.
- X. Tan, K. Li, A. Thursfield and I. S. Metcalfe, *Catal. Today*, 2008, **131**, 292.
- Q. Zeng, Y. B. Zuo, C. G. Fan and C. S. Chen, *J. Membr. Sci.*, 2009, **335**, 140.
- N. MacDowell, N. Florin, A. Buchard, J. Hallett, A. Galindo, G. Jackson, C. S. Adjiman, C. K. Williams, N. Shah and P. Fennell, *Energy Environ. Sci.*, 2010, **3**, 1645.
- P. Markewitz, W. Kuckshinrichs, W. Leitner, J. Linssen, P. Zapp, R. Bongartz, A. Schreiber and T. E. Müller, *Energy Environ. Sci.*, 2012, **5**, 7281.
- R. S. Haszeldine, *Science*, 2009, **325**, 1647.
- M. Schulz, R. Kriegel and A. Kämpfer, *J. Membr. Sci.*, 2011, **378**, 10.

- 17 Y. Teraoka, H. M. Zhang and N. Yamazoe, *Chem. Lett.*, 1985, 1367.
- 18 J. F. Vente, S. McIntosh, W. G. Haije and H. J. M. Bouwmeester, *J. Solid State Electrochem.*, 2006, **10**, 581.
- 19 Z. P. Shao, W. S. Yang, Y. Cong, H. Dong, J. H. Tong and G. X. Xiong, *J. Membr. Sci.*, 2000, **172**, 177.
- 20 S. Baumann, J. M. Serra, M. P. Lobera, S. Escolástico, F. Schulze-Küppers and W. A. Meulenber, *J. Membr. Sci.*, 2011, **377**, 198.
- 21 J. M. Serra, V. B. Vert, M. Betz, V. A. C. Haanappel, W. A. Meulenber and F. Tietz, *J. Electrochem. Soc.*, 2008, **155**, B207.
- 22 K. Partovi, B. Geppert, F. Y. Liang, C. H. Rüscher and J. Caro, *Chem. Mater.*, 2015, **27**, 2911.
- 23 X. Tan, N. Liu, B. Meng, J. Sunarso, K. Zhang and S. Liu, *J. Membr. Sci.*, 2012, **389**, 216.
- 24 A. Waidich, A. Mobius and M. Müller, *J. Membr. Sci.*, 2009, **337**, 182.
- 25 M. Arnold, H. H. Wang and A. Feldhoff, *J. Membr. Sci.*, 2007, **293**, 44.
- 26 O. Czuprat, M. Arnold, S. Schirrmeister, T. Schiestel and J. Caro, *J. Membr. Sci.*, 2010, **364**, 132.
- 27 X. F. Zhu, H. Liu, Y. Cong and W. Yang, *Chem. Commun.*, 2012, **48**, 251.
- 28 Z. Wang, W. Sun, Z. Zhu, T. Liu and W. Liu, *ACS Appl. Mater. Interfaces*, 2013, **5**, 11038.
- 29 H. X. Luo, H. Q. Jiang, T. Klande, Z. W. Cao, F. Y. Liang, H. H. Wang and J. Caro, *Chem. Mater.*, 2012, **24**, 2148.
- 30 F. Y. Liang, H. X. Luo, K. Partovi, O. Ravkina, Z. W. Cao, L. Yi and J. Caro, *Chem. Commun.*, 2014, **50**, 2451.
- 31 H. X. Luo, T. Klande, Z. W. Cao, F. Y. Liang, H. H. Wang and J. Caro, *J. Mater. Chem. A*, 2014, **2**, 7780.
- 32 Z. Wu, W. Jin and N. Xu, *J. Membr. Sci.*, 2006, **279**, 320.
- 33 X. Zhu, Q. Li, Y. Cong and W. Yang, *Catal. Commun.*, 2008, **10**, 309.
- 34 X. Dong, Z. Xu, X. Chang, C. Zhang and W. Jin, *J. Am. Ceram. Soc.*, 2007, **90**, 3923.
- 35 A. L. Shaula, V. V. Kharton, N. P. Vyshatko, E. V. Tsipis, M. V. Patrakeev, F. M. B. Marques and J. R. Frade, *J. Eur. Ceram. Soc.*, 2005, **25**, 489.
- 36 F. Y. Liang, K. Partovi, H. Q. Jiang, H. X. Luo and J. Caro, *J. Mater. Chem. A*, 2013, **1**, 746.
- 37 A. Feldhoff, M. Arnold, J. Martynczuk, T. M. Gesing and H. Wang, *Solid State Sci.*, 2008, **10**, 689.
- 38 M. Arnold, H. Wang, J. Martynczuk and A. Feldhoff, *J. Am. Ceram. Soc.*, 2007, **90**, 3651.
- 39 X. Zhu, H. Wang and W. Yang, *J. Membr. Sci.*, 2008, **309**, 120.
- 40 K. Partovi, F. Y. Liang, O. Ravkina and J. Caro, *ACS Appl. Mater. Interfaces*, 2014, **6**, 10274.
- 41 J. L. Garcia-Munoz and J. Rodriguez-Carvajal, *Phys. Rev. B: Condens. Matter Mater. Phys.*, 1992, **46**, 4414.
- 42 V. M. Goldschmidt, *Skr. Nor. Viedenk-Akad., Kl. I: Mater.-Naturvidensk. Kl.*, 1926, 8.
- 43 R. D. Shannon, *Acta Crystallogr., Sect. A: Cryst. Phys., Diffraction Theor. Gen. Crystallogr.*, 1976, **32**, 751.
- 44 J. W. Stevenson, T. R. Armstrong, R. D. Carneim, L. R. Pederson and W. J. Weber, *J. Electrochem. Soc.*, 1996, **143**, 2722.
- 45 L. W. Tai, M. M. Nasrallah, H. U. Anderson, D. M. Sparlin and S. R. Sehlin, *Solid State Ionics*, 1995, **76**, 259.
- 46 S. Sekido, H. Tachibana, Y. Yamamura and T. Kambara, *Solid State Ionics*, 1990, **37**, 253.
- 47 J. E. ten Elshof, H. J. M. Bouwmeester and H. Verweij, *Solid State Ionics*, 1995, **81**, 97.
- 48 J. Holc, D. Kuscer, M. Hrovat, S. Bernik and D. Kolar, *Solid State Ionics*, 1997, **95**, 259.
- 49 V. V. Kharton, A. L. Shaula, F. M. M. Snijkers, J. F. C. Coymans, J. J. Luyten, A. A. Yaremchenko, A. A. Valente, E. V. Tsipis, J. R. Frade, F. M. B. Marques and J. Rocha, *J. Membr. Sci.*, 2005, **252**, 215.
- 50 L. W. Tai, M. M. Nasrallah, H. U. Anderson, D. M. Sparlin and S. R. Sehlin, *Solid State Ionics*, 1995, **76**, 273.
- 51 J. Martynczuk, F. Y. Liang, M. Arnold, V. Sepelak and A. Feldhoff, *Chem. Mater.*, 2009, **21**, 1568.
- 52 C. Wagner, *Prog. Solid State Chem.*, 1975, **10**, 3.
- 53 T. Klande, O. Ravkina and A. Feldhoff, *J. Membr. Sci.*, 2013, **437**, 122.
- 54 O. Ravkina, T. Klande and A. Feldhoff, *J. Membr. Sci.*, 2015, **480**, 31.
- 55 K. Efimov, T. Klande, N. Juditzki and A. Feldhoff, *J. Membr. Sci.*, 2012, **389**, 205.
- 56 H. Yokokawa, N. Sakai, T. Kawada and M. Dokiya, *Solid State Ionics*, 1992, **52**, 43.

5.3. Enhanced Oxygen Permeability of Novel Cu-Containing CO₂-Tolerant Dual-Phase Membranes

Kaveh Partovi, Claus H. Rüscher, Frank Steinbach, and Jürgen Caro

Submitted for publication in Journal of Membrane Science **2015**.

Enhanced Oxygen Permeability of Novel Cu-Containing CO₂-Tolerant Dual-Phase Membranes

Kaveh Partovi,^{a,*} Claus H. Rüscher,^b Frank Steinbach,^a and Jürgen Caro^a

^a Institute of Physical Chemistry and Electrochemistry, Leibniz University of Hannover, Callinstr. 3a D-30167 Hannover, Germany

^b Institute of Mineralogy, Leibniz University of Hannover, Callinstr. 3a D-30167 Hannover, Germany

Abstract

Dense dual-phase membranes 40% Sm_{0.5}Sr_{0.5}Cu_{0.2}Fe_{0.8}O_{3-δ}–60% Ce_{0.8}Sm_{0.2}O_{2-δ} (SmSrCF5528-CSO) and 40% Sm_{0.3}Sr_{0.7}Cu_{0.2}Fe_{0.8}O_{3-δ}–60% Ce_{0.8}Sm_{0.2}O_{2-δ} (SmSrCF3728-CSO) were prepared *via* the citric acid/EDTA complexing sol-gel process. The phase composition and the microstructure of the membranes were characterized by XRD, SEM and EDXS analysis. The newly developed cobalt-free membranes SmSrCF5528-CSO and SmSrCF3728-CSO (0.6 mm thick) exhibited high oxygen fluxes of 1.12 and 1.15 cm³ min⁻¹ cm⁻², respectively, at 1000 °C with pure CO₂ as the sweep gas. The long-term CO₂ stability of each membrane was studied in the temperature range of 900-1000 °C for more than 200 h on stream. The SmSrCF5528-CSO membrane displayed very good stability at all temperatures. The oxygen permeation fluxes of the Sr-rich membrane SmSrCF3728-CSO were stable at 1000 and 950 °C.

Keywords: Oxygen-transporting ceramics, dual-phase membranes, CO₂-tolerant oxygen permeation, mixed conductor, Cu-doped perovskite

* kaveh.partovi@pci.uni-hannover.de

Introduction

During the past few decades, significant progress has been accomplished in the development and establishment of clean and sustainable energy generation technologies, such as solar energy, wind power and hydropower. However, current projections reveal that with an increasing global energy demand, the power generation remains to be fossil fuel-dependent for the upcoming decades [1]. While a variety of approaches for CO₂ mitigation, such as conversion of CO₂ to value-added products or CO₂ valorization are under intensive study [2], carbon capture and storage (CCS) is considered as a readily applicable technology for immediate reduction of anthropogenic CO₂ emissions from the main point sources, such as fossil fuel power plants [3]. The oxyfuel concept for CCS is based on the fuel combustion in high-purity oxygen instead of air, thus facilitating the CO₂ capture and compression from the CO₂-rich flue gas. In order to avoid excessively high flame temperatures in the oxyfuel route, the oxygen concentration is partly diluted by a stream of CO₂ recirculated from the flue gas to the combustion chamber [1]. However, the conventional cryogenic air separation unit (ASU) is accounted for a major efficiency loss in the power plants with oxyfuel CO₂ capture. Accordingly, less energy-intensive alternatives, such as utilization of oxygen-transporting membranes (OTM) based on mixed ionic-electronic conducting ceramics (MIEC) has gained considerable attention as a promising substitute for the cryogenic distillation ASU [4,5].

High oxygen permeability and good structural stability in the presence of high concentrations of CO₂ are among the fundamental requirements for a viable integration of MIEC-based OTMs in the oxyfuel route [6]. OTMs with the highest oxygen permeabilities are based on perovskite-type oxides with the general formula ABO_3 , that contain high concentrations of Sr and Ba at their *A*-site, *e.g.* (Ba,Sr)(Fe,Co)O_{3- δ} [7-9]. Under the operation conditions of the oxyfuel process, the *A*-site alkaline-earth cations Ba and Sr react with gaseous CO₂ to form an oxygen-impermeable carbonate phase on the membrane surface, resulting in degradation of the membrane's performance [10,11]. Although partial substitution of the *A*-site alkaline-earth cations (Sr²⁺ and Ba²⁺) with rare earth elements, such as La³⁺ and Pr³⁺, improves the CO₂ stability of the perovskite, it also compromises the permeability of the membrane, mainly due to decreased oxygen non-stoichiometry [7,12-14].

Development of dual-phase membranes, generally consisting of a mixed-conducting perovskite phase and an ionic-conducting fluorite-type oxide (mainly doped ceria), has resulted in improved

thermochemical stability [15,16]. Some examples of dual-phase membranes include $\text{Ce}_{0.9}\text{Pr}_{0.1}\text{O}_{2-\delta}\text{-Pr}_{0.6}\text{Sr}_{0.4}\text{FeO}_{3-\delta}$ [17], $\text{Ce}_{0.9}\text{Gd}_{0.1}\text{O}_{2-\delta}\text{-NiFe}_2\text{O}_4$ [18], $\text{Ce}_{0.85}\text{Sm}_{0.15}\text{O}_{1.925}\text{-Sm}_{0.6}\text{Sr}_{0.4}\text{Al}_{0.3}\text{Fe}_{0.7}\text{O}_3$ [19], $\text{Ce}_{0.8}\text{Sm}_{0.2}\text{O}_{1.9}\text{-Sm}_{0.6}\text{Ca}_{0.4}\text{FeO}_{3-\delta}$ [20]. However, for large-scale application of dual-phase OTMs in the oxyfuel power plants, the permeation performance of these materials still needs to be enhanced. Although incorporation of cobalt into the *B*-site of the perovskite structure can remarkably increase the oxygen permeability of the membranes [20,21], due to various issues associated with cobalt such as its high cost, toxicity and low thermochemical stability, many studies focus on the development of cobalt-free OTMs [20,22]. An enhanced oxygen permeation flux of single-phase perovskites by partial substitution of the *B*-site cation with Cu has been previously reported [23,24]. Teraoka *et al.* reported the highest oxygen permeability for the Cu-substituted perovskite in the system $\text{La}_{0.6}\text{Sr}_{0.4}\text{Co}_{0.8}\text{B}'_{0.2}\text{O}_{3-\delta}$ ($\text{B}' = \text{Fe}, \text{Co}, \text{Ni}, \text{Cu}$) [25]. Ling *et al.* studied Cu-doped perovskite $\text{Sm}_{0.5}\text{Sr}_{0.5}\text{Fe}_{0.8}\text{Cu}_{0.2}\text{O}_{3-\delta}$ for applications as cathode material for solid state fuel cells (SOFC) [26]. In the present study, the oxygen permeation performance, CO_2 stability and microstructure of two novel dual-phase membranes 40 wt.% $\text{Sm}_{0.5}\text{Sr}_{0.5}\text{Cu}_{0.2}\text{Fe}_{0.8}\text{O}_{3-\delta}$ –60 wt.% $\text{Ce}_{0.8}\text{Sm}_{0.2}\text{O}_{2-\delta}$ (SmSrCF5528-CSO) and 40 wt.% $\text{Sm}_{0.3}\text{Sr}_{0.7}\text{Cu}_{0.2}\text{Fe}_{0.8}\text{O}_{3-\delta}$ –60 wt.% $\text{Ce}_{0.8}\text{Sm}_{0.2}\text{O}_{2-\delta}$ (SmSrCF3728-CSO) have been investigated.

Experimental

Powder samples of the dual-phase compositions 40 wt.% $\text{Sm}_{0.5}\text{Sr}_{0.5}\text{Cu}_{0.2}\text{Fe}_{0.8}\text{O}_{3-\delta}$ –60 wt.% $\text{Ce}_{0.8}\text{Sm}_{0.2}\text{O}_{2-\delta}$ (abbreviated as SmSrCF5528-CSO) and 40 wt.% $\text{Sm}_{0.3}\text{Sr}_{0.7}\text{Cu}_{0.2}\text{Fe}_{0.8}\text{O}_{3-\delta}$ –60 wt.% $\text{Ce}_{0.8}\text{Sm}_{0.2}\text{O}_{2-\delta}$ (abbreviated as SmSrCF3728-CSO) were synthesized by a one-pot sol-gel citric acid/EDTA complexing method. The aqueous precursor solution was prepared by mixing stoichiometric amounts of nitrate solutions of the related cations with ethylenediamine tetraacetic acid (EDTA) and citric acid (CA), to obtain a total metal cation/EDTA/CA ratio of 1:1:1.5. The pH value of the precursor solution was adjusted ~9 by addition of ammonia solution. The powder samples were obtained after evaporation and calcination steps, described in detail elsewhere [27]. The dual-phase membranes were prepared by uniaxially pressing the ground powder samples under a pressure of ~120 MPa into green disks using a stainless steel module (18 mm in diameter), followed by a sintering process at 1225 °C for 5 h with heating/cooling rates of 2 °C min^{-1} in ambient air. The sintered gas-tight membranes were 0.6 mm thick and 16 mm in diameter.

The phase structures of the powder samples as well as the as-sintered membranes were studied by X-ray diffraction (XRD) at room temperature. The XRD patterns were collected on a Bruker-AXS D8 Advance diffractometer equipped with a Cu-K α radiation source operating in a step-scan mode in the 2θ range of 20-80° at intervals of 0.02°.

Scanning electron microscopy (SEM) and back-scattered electron microscopy (BSEM) were utilized to investigate the microstructures and the phase compositions of the membranes. The SEM and BSEM imaging was carried out on a JEOL JSM 6700-F field-emission electron microscope at excitation voltages of 2 kV and 20 kV, respectively. Energy-dispersive X-ray spectroscopy (EDXS) was performed using an Oxford Instruments INCA A-300 spectrometer at the excitation voltage of 20 kV.

Thermogravimetric and differential thermal analysis (TGA/DTA) was performed on the ground powder samples with varying Sr contents after calcination at 950 °C using a Setaram Setsys Evolution 1750 thermoanalyzer in the temperature range of 30 to 1000 °C with heating/cooling rates of 10 °C min⁻¹ using synthetic air at a flow rate of 20 cm³ min⁻¹ as the purge gas.

Oxygen permeation measurements were conducted in a high-temperature permeation cell, which was placed in the center of a vertical tubular oven. The 0.6-mm-thick membranes were sealed onto an alumina tube using gold cermet (conduction paste C5754, Heraeus, Hanau, Germany), resulting in an effective membrane area of ~0.6 cm². Oxygen permeation fluxes were measured in the temperature range of 800-1000 °C. The temperature was carefully monitored using a K-type thermocouple placed close to the membrane's surface. The detailed description of the experimental setup is provided in previous publications [14,27]. Synthetic air, consisting of 20 vol.% O₂ and 80 vol.% N₂, at a flow rate of 150 cm³ min⁻¹ was used as the feed gas. The permeation side of the membrane was swept with He (Linde, 99.996%) or CO₂ (Linde, 99.5%) at a flow of 49 cm³ min⁻¹ and Ne (Linde, 99.995%) at a flow of 1 cm³ min⁻¹, as the internal standard gas to calculate the total flow rate of the effluent. The total flow rate of the effluent gas mixture could also be separately measured using a soap-film flow meter. All the inlet gas flow rates were regulated by mass flow controllers (MFC, Bronkhorst, Ruurlo, The Netherlands). An online-coupled gas chromatograph (GC) of the type Agilent 6890A equipped with a Carboxen-1000 column (Supelco) was applied for the quantitative analysis of the effluent's composition. Negligible amounts of oxygen leakage (<1% O₂ leakage) could be detected by monitoring the N₂ concentration in the effluent and were ultimately subtracted from the total O₂ permeation flux.

segregated CuO particles, due to increased volume of the perovskite unit cell (as shown in **Figure 2a**). A similar trend of stabilization of the perovskite structure by increasing the Sr content has been previously reported for $\text{La}_{1-x}\text{Sr}_x\text{CuO}_{3-\delta}$ [28].

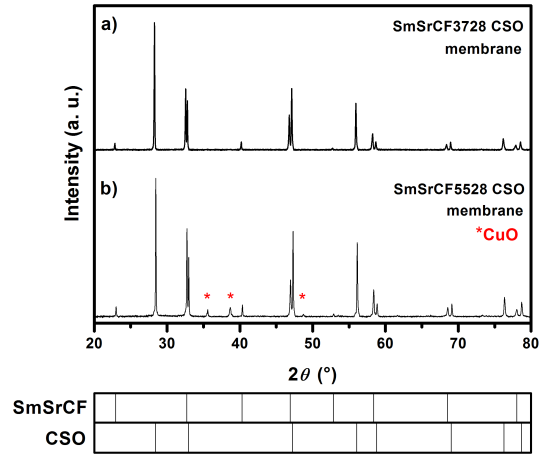


Figure 2. Room-temperature XRD patterns of the dual-phase membranes after sintering at 1225 °C for 5 h: a) SmSrCF3728-CSO, b) SmSrCF5538-CSO. The diffraction reflections corresponding to the segregated CuO phase are marked with asterisks (*).

Table 1. Ionic radii of the *A*-site (12-coordinated) and the *B*-site species (6-coordinated) of the SmSrCF perovskite phase [29].

| Cation | Radius (pm) |
|------------------------|-------------|
| Sm^{3+} | 124 |
| Sr^{2+} | 144 |
| Cu^{2+} | 73.0 |
| Cu^{3+} | 54.0 |
| Fe^{3+} (HS)* | 64.5 |
| Fe^{3+} (LS)# | 55.0 |
| Fe^{4+} | 58.5 |

* high spin

low spin

Microstructure and elemental analysis

The SEM micrographs of the membranes are provided in **Figure 3**. The surface of the sintered SmSrCF5528-CSO membrane consisted of densely packed grains. However, formation of additional particles could also be clearly observed on the membrane's surface. The EDXS analysis (**Figures 3c-f**) revealed that the additional particles shown in **Figure 3b**, were segregated CuO particles on the surface of the SmSrCF5528-CSO membrane, which were previously detected by XRD measurements. Moreover, construction of a percolation network consisting of the two main phases, *i.e.* the mixed conducting perovskite phase and the ionic conducting doped ceria phase, is evident.

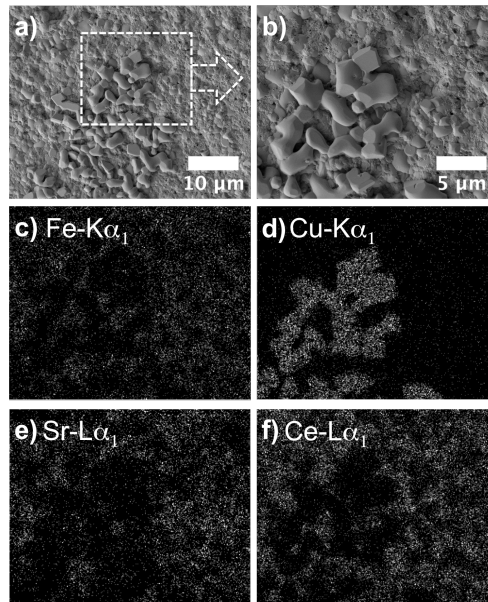


Figure 3. Microstructure of the SmSrCF5528-CSO membrane sintered at 1225 °C for 5 h: a) SEM micrograph, b) Magnification of the marked area shown in panel (a), c-f) Elemental distribution of the area shown in panel (b) using EDXS analysis.

Figure 4 shows the microstructure and the EDXS analysis of the SmSrCF3728-CSO membrane surface. As expected from the XRD measurements, increasing the Sr content at the *A*-site of the perovskite phase SmSrCF from 50 at.% to 70 at.% resulted in elimination of the segregated CuO phase, which was previously observed on the surface of the membrane with lower Sr content. Formation of two separate phases is clearly distinguishable in the BSEM micrograph of the

SmSrCF3728-CSO membrane's surface, where lighter grains relating to the ionic conducting doped ceria phase and dark grains of the perovskite phase build a percolation network. Furthermore, the EDXS elemental analysis, presented in **Figures 4d & 4e** indicates a homogeneous distribution of Ce and Sr within the grains of the corresponding ceria and perovskite phases, respectively. However, as shown in Figure 4f, Cu was found to be diffused in both phases, with a slightly higher concentration in the perovskite-related grains. The diffusion of Cu in the fluorite-type doped ceria could also have positively affected the overall permeability of the dual-phase membrane, as was recently reported by Fang *et al.* [30].

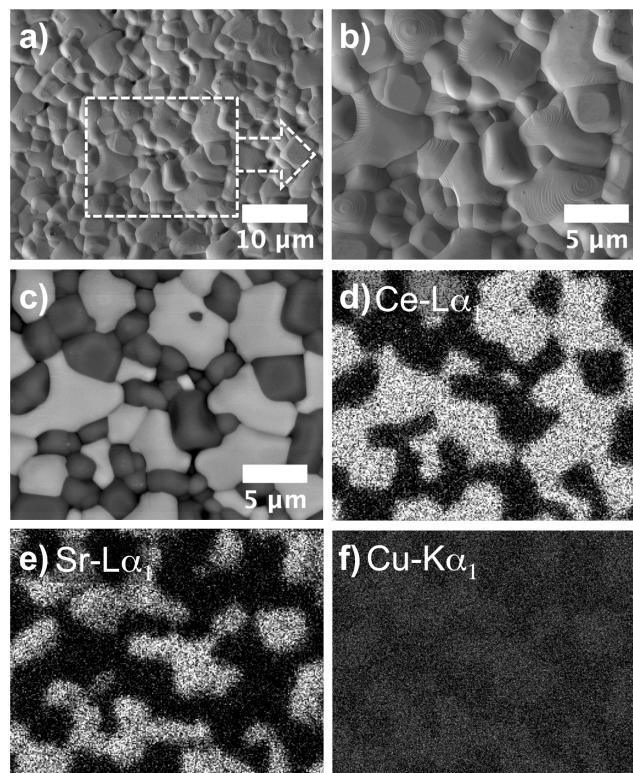


Figure 4. Microstructure of the SmSrCF3728-CSO membrane sintered at 1225 °C for 5 h: a) SEM micrograph, b) Magnification of the marked area shown in panel (a), c) BSEM image of the area shown in panel (b), d-f) Elemental distribution of the area shown in panel (b) using EDXS analysis.

Thermoanalysis

The results of the thermoanalysis performed on powder samples of the dual-phase compositions SmSrCF5528-CSO and SmSrCF3728-CSO in synthetic air are presented in **Figure 5**, where the samples undergo a reversible reduction in mass, due to partial loss of lattice oxygen upon heating. The TGA shows no weight loss for the samples up to about 400 °C with synthetic air as the purge gas. Above 400 °C, due to simultaneous thermal reduction of the *B*-site cations and release of lattice oxygen, a negative change of mass is observed. Although the onset temperature for oxygen release does not significantly change with varying Sr contents, the rate and the magnitude of weight loss upon heating is noticeably higher for the SmSrCF3728-CSO sample with increased content of Sr, compared to that of SmSrCF5528-CSO. A similar trend of increasing weight loss for perovskites with higher concentrations of acceptor-dopant Sr²⁺ has been previously reported in other studies [31,32]. Furthermore, the DTA results revealed no phase transition in the temperature range of 30-1000 °C, as shown in the inset of **Figure 5**.

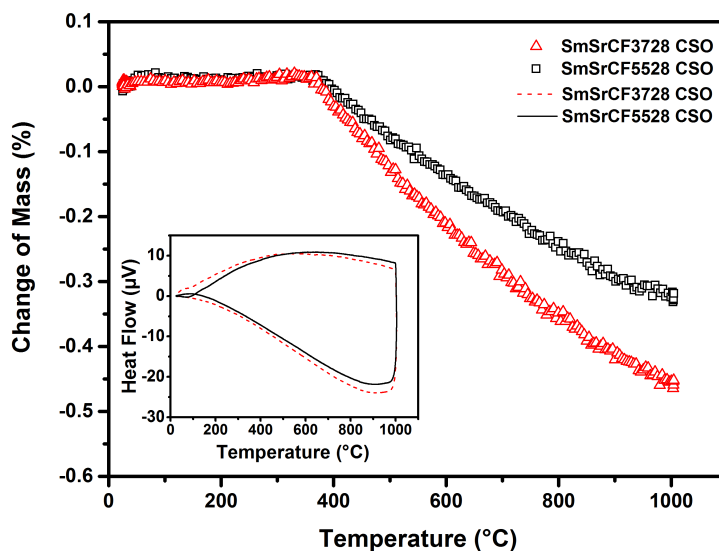


Figure 5. TGA results of powder samples of the dual-phase compositions SmSrCF5528-CSO (black squares) and SmSrCF3728-CSO (red triangles) in synthetic air. The inset shows differential thermal analysis of the samples as a function of temperature. Flow of synthetic air: 20 cm³ min⁻¹, heating rate: 10 °C min⁻¹.

Oxygen permeation performance

The oxygen permeation properties of the dual-phase membranes were studied using pure He and pure CO₂ as the sweeping gases. The results of the temperature-dependent oxygen permeation measurements and the corresponding Arrhenius plots are shown in **Figure 6**. The SmSrCF3728-CSO membrane with the higher Sr content exhibited the highest permeation fluxes reaching up to 1.35 and 1.04 cm³ min⁻¹ cm⁻² at 1000 °C and 950 °C, respectively, with He as the sweep gas. As previously observed for the TGA results, the increasing amount of divalent Sr as a substitute for trivalent Sm, leads to higher concentrations of oxygen vacancies [31]. It should be noted that increasing the unit cell volume of the perovskite, due to higher concentration of *A*-site Sr is also expected to facilitate the oxygen migration through the lattice. Under the same conditions, the oxygen permeation fluxes of the SmSrCF5528-CSO membrane with 1.27 and 1.01 cm³ min⁻¹ cm⁻² at 1000 °C and 950 °C, respectively, were found to be relatively lower than those of the SmSrCF3728-CSO membrane.

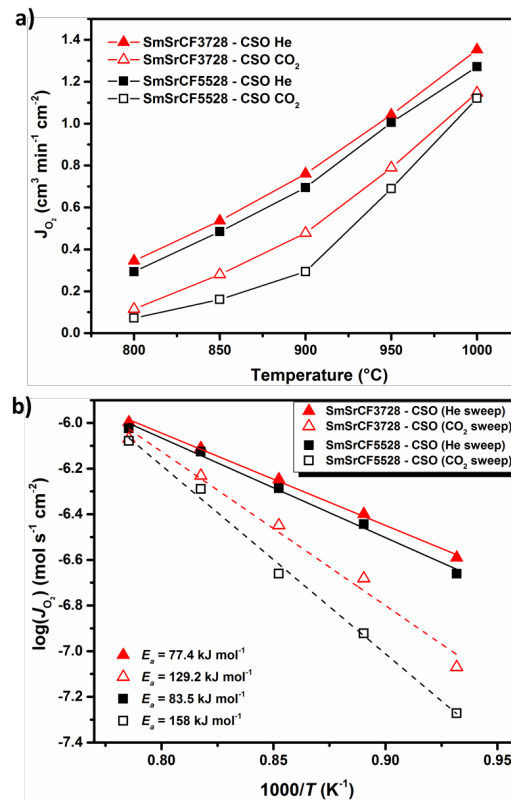


Figure 6. Temperature-dependent oxygen permeation fluxes measured on the SmSrCF-CSO dual-phase membranes with various Sr contents using He (close symbols) and CO₂ (open symbols) as sweep gases. b) Arrhenius plots of the oxygen permeation fluxes with calculated apparent activation energies. Feed side: 150 cm³ min⁻¹ synthetic air; Sweep side: 49 cm³ min⁻¹ He or CO₂ + 1 cm³ min⁻¹ Ne as internal standard; Membrane thickness: 0.6 mm.

By switching the sweep gas to CO₂, the permeation fluxes of both membranes slightly decreased. At 1000 °C, oxygen fluxes of 1.15 and 1.12 cm³ min⁻¹ cm⁻² were measured for the SmSrCF3728-CSO and SmSrCF5528-CSO membranes, respectively. Furthermore, the apparent activation energies, E_a , for each membrane with He and CO₂ sweeping were calculated using the Arrhenius plots shown in **Figure 6b**. The lowest activation energy of 77.4 kJ mol⁻¹ was calculated for He-swept SmSrCF3728-CSO, which is in accordance with the faster course of thermally activated oxygen release from this sample compared to that of SmSrCF5528-CSO observed from the TGA results.

Long-term stability of the dual-phase membranes under practice-relevant conditions was studied using He and CO₂ as the sweep gases. The oxygen permeation performances of the membranes are presented in **Figure 7**. Both membranes showed good stability at 1000 °C under He-sweeping. A short stabilization stage was observed for both membranes, after the sweep gas was switched to CO₂ at 1000 °C. By reducing the temperature to 950 °C, the SmSrCF5528-CSO membrane displayed a stable oxygen flux of about 0.67 cm³ min⁻¹ cm⁻² for more than 120 h, whereas for the SmSrCF3728-CSO membrane a relatively long stabilization stage of about 20 h was observed, during which the oxygen flux gradually decreased from 0.77 to 0.70 cm³ min⁻¹ cm⁻² to reach a steady state. The appearance of a prolonged stabilization stage with decreasing permeation fluxes is related to the reactivity of Sr with gaseous CO₂ to form SrCO₃ on the outer surface layer of the CO₂-swept membrane, thus inhibiting the oxygen surface exchange reaction. Accordingly, the higher Sr content at the *A*-site of the perovskite increases the CO₂ susceptibility of the membrane. The Ellingham diagram regarding the temperature-dependent stability of SrCO₃ reveals increasing thermodynamic stabilities with decreasing temperatures under a constant CO₂ partial pressure [33]. Consequently, at 900 °C both membranes undergo stages of decreasing permeation fluxes. The SmSrCF5528-CSO membrane shows a slight decrease in oxygen flux from 0.29 to 0.25 cm³ min⁻¹ cm⁻² in the first 50 h at 900 °C, after which a steady state is maintained for at least 40 h. The extent and rate of the observed decrease in oxygen fluxes is more significant for the oxygen fluxes on the SmSrCF3728-CSO membrane, which change from 0.46 to 0.38 cm³ min⁻¹ cm⁻² after 50 h.

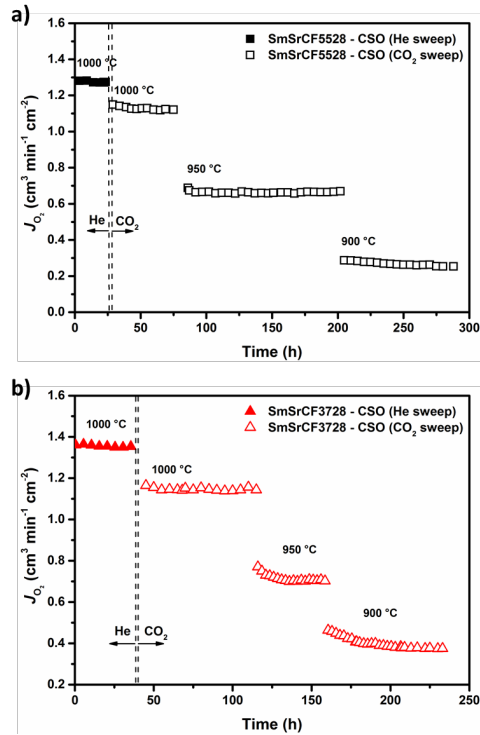


Figure 7. Long-term oxygen permeation fluxes of: a) SmSrCF5528-CSO, and b) SmSrCF3728-CSO membranes. Feed side: 150 cm³ min⁻¹ synthetic air. Sweep side: 49 cm³ min⁻¹ He (solid symbols) or CO₂ (open symbols) + 1 cm³ min⁻¹ Ne as internal standard. Membrane thickness: 0.6 mm.

The microstructures of the sweep sides of the spent dual-phase membranes were studied using SEM. For this purpose, the previously discussed membranes with O₂ permeation fluxes shown in **Figure 7** (designated as M1) and two additional membranes after 100 h CO₂ exposure at 950 °C (designated as M2) are compared in **Figure 8**. As can be seen, basically all membranes maintained their structural integrity and no deterioration of the membrane's density could be observed after long-term CO₂ exposure. In addition, the EDXS analysis of the sweep sides of the membranes confirmed that the phase composition was preserved. However, as expected from the oxygen permeation results of the SmSrCF5528-CSO and SmSrCF3728-CSO membranes, the microstructure of the latter composition with higher Sr content is clearly more heavily affected by the CO₂ exposure, than that of SmSrCF5528-CSO with less Sr content. As previously mentioned,

the formation of alkaline-earth carbonates, such as BaCO_3 and SrCO_3 , is thermodynamically preferred at lower temperatures, which results in a completely intact microstructure of the CO_2 -swept side of the membranes at $950\text{ }^\circ\text{C}$ (M2 in **Figure 8**), even for the Sr-rich composition SmSrCF3728-CSO. However, as shown in **Figure 9**, further investigation of the spent SmSrCF3728-CSO membrane using SEM and EDXS analysis indicated that a layer of CuO was formed on the feed side of the membrane after the long-term oxygen permeation measurements, resulting in the depletion of Cu from the adjacent lower grains, which could possibly be a result of cationic counter-diffusion of Cu to the oxygen-rich side during the operation. Furthermore, the observation of a steady state of oxygen permeation flux is inconsistent with the gradual formation of CuO during the permeation operation. The conditions and quality of CuO formation during and after the permeation measurements and its effect on the permeation performance require further investigation by means of other characterization methods such as in-situ XRD, which can be the subject of a separate study.

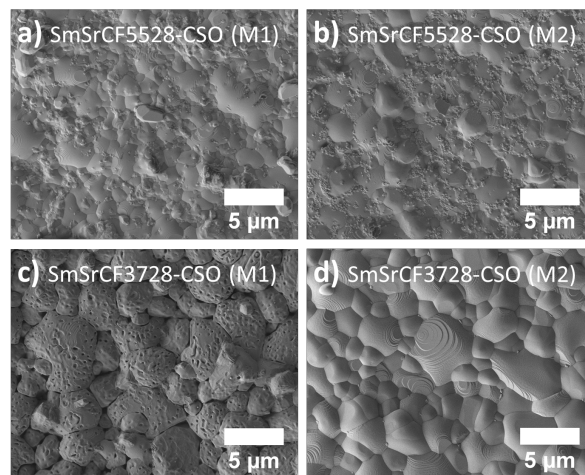


Figure 8. SEM micrographs of the sweep side of the spent dual phase membranes: a & b) SmSrCF5528-CSO, c & d) SmSrCF3728-CSO. M1: Membranes with O_2 permeation results shown in **Figure 7**. M2: separately measured membranes, swept with CO_2 at $950\text{ }^\circ\text{C}$ for 100 h under the same experimental conditions as M1 membranes.

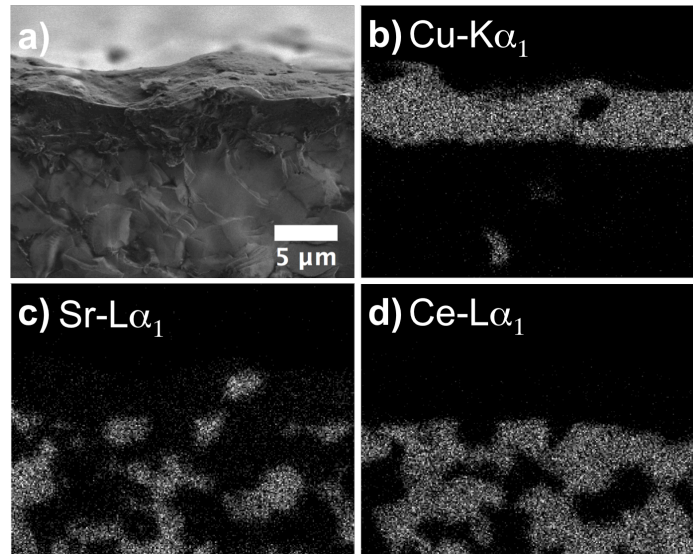


Figure 9. Microstructure of the SmSrCF3728-CSO (M1) membrane's cross-section after long-term oxygen permeation measurements: a) SEM micrograph, b-d) Elemental distribution of the area shown in panel (a) using EDXS analysis.

Conclusion

Dual-phase compositions 40% $\text{Sm}_{0.5}\text{Sr}_{0.5}\text{Cu}_{0.2}\text{Fe}_{0.8}\text{O}_{3-\delta}$ –60% $\text{Ce}_{0.8}\text{Sm}_{0.2}\text{O}_{2-\delta}$ (SmSrCF5528-CSO) and 40% $\text{Sm}_{0.3}\text{Sr}_{0.7}\text{Cu}_{0.2}\text{Fe}_{0.8}\text{O}_{3-\delta}$ – 60% $\text{Ce}_{0.8}\text{Sm}_{0.2}\text{O}_{2-\delta}$ (SmSrCF3728-CSO) were synthesized *via* a conventional one-pot sol-gel synthesis route. The XRD analysis of the powder samples verified that the composite materials consisted of a perovskite phase (SmSrCF) and a fluorite phase (CSO), without any impurities. However, the XRD results of the sintered membranes revealed the formation of an additional CuO phase on the surface of the SmSrCF5528-CSO membrane with lower Sr content, which was also confirmed by SEM and EDXS analysis. Increasing the Sr content of the perovskite resulted in incorporation of the Cu into the perovskite structure, due to the larger unit cell of the perovskite phase SmSrCF3728 of the composite material.

High oxygen permeation fluxes of 1.15 and 1.12 $\text{cm}^3 \text{min}^{-1} \text{cm}^{-2}$ were measured at 1000 °C on the 0.6-mm-thick SmSrCF3728-CSO and SmSrCF5528-CSO membranes, respectively, which was also in good accordance with the TGA results confirming higher oxygen release from the

composition with higher Sr content. Both membranes exhibited good long-term CO₂ stability at 1000 °C. At 950 °C, the SmSrCF5528-CSO membrane maintained a stable oxygen permeation flux of about 0.67 cm³ min⁻¹ cm⁻² for more than 120 h, whereas the membrane with increased Sr content reached a steady state of 0.70 cm³ min⁻¹ cm⁻² after 20 h. A constant oxygen flux of about 0.25 cm³ min⁻¹ cm⁻² was measured on the SmSrCF5528-CSO membrane after 40 h at 900 °C.

In conclusion, the newly developed SmSrCF-CSO membranes exhibited very good oxygen permeation properties under pure CO₂ sweeping. The high CO₂ tolerance of the membranes recommends them as promising candidates for applications in oxyfuel processes for CO₂ capture and high-temperature catalytic membrane reactors.

Acknowledgment

The authors gratefully acknowledge the financial support by DFG Ca 147/18-1 and the Sino-German Centre for Research Promotion (Nos. GZ676 and GZ911).

References

- [1] P. Markewitz, W. Kuckshinrichs, W. Leitner, J. Linssen, P. Zapp, R. Bongartz, A. Schreiber, T. E. Müller, Worldwide innovations in the development of carbon capture technologies and the utilization of CO₂, *Energy Environ. Sci.* 5 (2012) 7281-7305.
- [2] J. Albo, M. Alvarez-Guerra, P. Castaño, A. Irabien, Towards the Electrochemical Conversion of Carbon Dioxide into Methanol, *Green Chem.* 17 (2015) 2304-2324.
- [3] D. P. Schrag, Preparing to capture carbon, *Science* 315 (2007) 812-813.
- [4] M. Kanniche, R. Gros-Bonnivard, P. Jaud, J. Valle-Marcos, J.-M. Amann, C. Bouallou, Pre-combustion, post-combustion and oxy-combustion in thermal power plant for CO₂ capture, *Appl. Therm. Eng.* 30 (2010) 53-62.
- [5] M. Schulz, R. Kriegel, A. Kämpfer, Assessment of CO₂ stability and oxygen flux of oxygen permeable membranes. *J. Membr. Sci.* 378 (2011) 10-17.
- [6] Y. Chen, Q. Liao, Y. Y. Wei, Z. Li, H. H. Wang, A CO₂-stable K₂NiF₄-type oxide (Nd_{0.9}La_{0.1})₂(Ni_{0.74}Cu_{0.21}Al_{0.05})O_{4+δ} for oxygen separation, *Ind. Eng. Chem. Res.* 52 (2013) 8571-8578.

- [7] Y. Teraoka, H.-M. Zhang, S. Furukawa, N. Yamazoe, Oxygen permeation through perovskite-type oxides, *Chem. Lett.* (1985) 1743-1746.
- [8] J. Sunarso, S. Baumann, J. M. Serra, W. A. Meulenber, S. Liu, Y. S. Lin, J. C. D. da Costa, Mixed ionic-electronic conducting (MIEC) ceramic-based membranes for oxygen separation, *J. Membr. Sci.* 320 (2008) 13–41.
- [9] O. Czuprat, M. Arnold, S. Schirmeister, T. Schiestel, J. Caro, Influence of CO₂ on the oxygen permeation performance of perovskite-type BaCo_xFe_yZr_zO_{3-δ} hollow fibre Membranes, *J. Membr. Sci.* 364 (2010) 132-137.
- [10] Z. P. Shao, W. S. Yang, Y. Cong, H. Dong, J. H. Tong, G. X. Xiong, Investigation of the permeation behavior and stability of a Ba_{0.5}Sr_{0.5}Co_{0.8}Fe_{0.2}O_{3-δ} oxygen membrane, *J. Membr. Sci.* 172 (2000) 177-188.
- [11] M. Arnold, H. H. Wang, A. Feldhoff, Influence of CO₂ on the oxygen permeation performance and the microstructure of perovskite-type (Ba_{0.5}Sr_{0.5})(Co_{0.8}Fe_{0.2})O_{3-δ}, *J. Membr. Sci.* 293 (2007) 44-52.
- [12] A. Waindich, A. Mobius, M. Müller, Corrosion of Ba_{1-x}Sr_xCo_{1-y}Fe_yO_{3-δ} and La_{0.3}Ba_{0.7}Co_{0.2}Fe_{0.8}O_{3-δ} materials for oxygen separating membranes under oxycoal conditions, *J. Membr. Sci.* 337 (2009) 182–187.
- [13] T. Klande, O. Ravkina, A. Feldhoff, Effect of A-site lanthanum doping on the CO₂ tolerance of SrCo_{0.8}Fe_{0.2}O_{3-δ} oxygen-transporting membranes *J. Membr. Sci.* 437 (2013) 122-130.
- [14] K. Partovi, F. Y. Liang, O. Ravkina, J. Caro, High-flux oxygen-transporting membrane Pr_{0.6}Sr_{0.4}Co_{0.5}Fe_{0.5}O_{3-δ}: CO₂ stability and microstructure, *ACS Appl. Mater. Interfaces* 6 (2014) 10274-10282.
- [15] V. V. Kharton, A. V. Kovalevsky, A. P. Viskup, F. M. Figueiredo, A. A. Yaremchenko, E. N. Naumovich, F. M. B. Marques, Oxygen permeability of Ce_{0.8}Gd_{0.2}O_{2-δ}-La_{0.7}Sr_{0.3}MnO_{3-δ}, *J. Electrochem. Soc.* 147 (2000) 2814-2821.
- [16] X. F. Zhu, W. S. Yang, Ionic conductor-mixed conductor based composite membrane for oxygen separation and POM reaction, *AIChE J.* 54 (2008) 665-672.
- [17] H. X. Luo, H. Q. Jiang, T. Klande, Z. W. Cao, F. Y. Liang, H. H. Wang, J. Caro, Novel cobalt-free, noble metal-free oxygen-permeable 40 Pr_{0.6}Sr_{0.4}FeO_{3-δ}-60Ce_{0.9}Pr_{0.1}O_{2-δ} dual-phase membrane, *Chem. Mater.* 24 (2012) 2148-2154.

- [18] H. X. Luo, K. Efimov, H. Q. Jiang, A. Feldhoff, H. H. Wang, J. Caro, CO₂-stable and cobalt-free dual-phase membrane for oxygen separation, *Angew. Chem. Int. Ed.* 50 (2011) 759-763.
- [19] X. F. Zhu, Y. Liu, Y. Cong, W. S. Yang, Ce_{0.85}Sm_{0.15}O_{1.925}-Sm_{0.6}Sr_{0.4}Al_{0.3}Fe_{0.7}O₃ dual-phase membrane: One-pot synthesis and stability in a CO₂ atmosphere, *Solid State Ionics* 253 (2012) 57-63.
- [20] H. Li, X. F. Zhu, Y. Liu, W. Wang, W. S. Yang, Comparative investigation of dual-phase membranes containing cobalt and iron-based mixed conducting perovskite for oxygen permeation, *J. Membr. Sci.* 462 (2014) 170-177.
- [21] F. Y. Liang, H. X. Luo, K. Partovi, O. Ravkina, Z. W. Cao, Y. Liu, J. Caro, A novel CO₂-stable dual phase membrane with high oxygen permeability, *Chem. Commun.* 50 (2014) 2451-2454.
- [22] H. J. M. Bouwmeester, Dense ceramic membranes for methane conversion, *Catal. Today* 82 (2003) 141-150.
- [23] Y. Teraoka, T. Nobunaga, N. Yamazoe, Effect of cation substitution on the oxygen semipermeability of perovskite-type oxides, *Chem. Lett.* (1988) 503-506.
- [24] V. V. Kharton, V. N. Tikhonovich, L. Shuangbao, E. N. Naumovich, A. V. Kovalevsky, A. P. Viskup, I. A. Bashmakov, A. A. Yaremchenko, Ceramic microstructure and oxygen permeability of SrCo(Fe, M)O_{3-δ} (M = Cu or Cr) perovskite membranes, *J. Electrochem. Soc.* 145 (1998) 1363-1373.
- [25] Y. Teraoka, T. Nobunaga, K. Okamoto, N. Miura, N. Yamazoe, Influence of constituent metal cations in substituted LaCoO₃ on mixed conductivity and oxygen permeability, *Solid State Ionics* 48 (1991) 207-212.
- [26] Y. Ling, L. Zhao, B. Lin, Y. Dong, X. Zhang, G. Meng, X. Liu, Investigation of cobalt-free cathode material Sm_{0.5}Sr_{0.5}Fe_{0.8}Cu_{0.2}O_{3-δ} for intermediate temperature solid oxide fuel cell, *Int. J. Hydrogen Energy* 35 (2010) 6905-6910.
- [27] F. Y. Liang, K. Partovi, H. Q. Jiang, H. X. Luo, J. Caro, B-site La-doped BaFe_{0.95-x}La_xZr_{0.05}O_{3-δ} perovskite-type membranes for oxygen separation *J. Mater. Chem. A* 1 (2013) 746-751.
- [28] H. C. Yu, K. Z. Fung, Role of Sr addition on the structure stability and electrical conductivity of Sr-doped lanthanum copper oxide perovskites, *J. Mater. Res.* 3 (2004) 943-949.

- [29] R. D. Shannon, Revised effective ionic radii and systematic studies of interatomic distances in halides and chalcogenides, *Acta Crystallogr., Sect. A: Cryst. Phys., Diffr., Theor. Gen. Crystallogr.* 32 (1976) 751-767.
- [30] W. Fang, F. Y. Liang, Z. W. Cao, F. Steinbach, A. Feldhoff, A Mixed Ionic and Electronic Conducting Dual-Phase Membrane with High Oxygen Permeability, *Angew. Chem. Int. Ed.* 54 (2015) 4847-4850.
- [31] L. W. Tai, M. M. Nasrallah, H. U. Anderson, D. M. Sparlin, S. R. Sehlin, Structure and electrical properties of $\text{La}_{1-x}\text{Sr}_x\text{Co}_{1-y}\text{Fe}_y\text{O}_3$. Part 2. The system $\text{La}_{1-x}\text{Sr}_x\text{Co}_{0.2}\text{Fe}_{0.8}\text{O}_3$, *Solid State Ionics*, 76 (1995) 273-283.
- [32] J. W. Stevenson, T. R. Armstrong, R. D. Carneim, L. R. Pederson, W. J. Weber, Electrochemical properties of mixed conducting perovskites $\text{La}_{1-x}\text{M}_x\text{Co}_{1-y}\text{Fe}_y\text{O}_{3-\delta}$ (M = Sr, Ba, Ca), *J. Electrochem. Soc.* 143 (1996) 2722-2729.
- [33] K. Efimov, T. Klande, N. Juditzki, A. Feldhoff, Ca-containing CO_2 -tolerant perovskite materials for oxygen separation, *J. Membr. Sci.* 389 (2012) 205-215.

Appendix

Publications Included in the Thesis

1. Partovi, K.;* Liang, F. Y.; Ravkina, O.; Caro, J. High-Flux Oxygen-Transporting Membrane $\text{Pr}_{0.6}\text{Sr}_{0.4}\text{Co}_{0.5}\text{Fe}_{0.5}\text{O}_{3-\delta}$: CO_2 Stability and Microstructure. *ACS Appl. Mater. Interfaces* **2014**, *6*, 10274-10282.
2. Partovi, K.;* Geppert, B.; Liang, F. Y.; Rüscher, C. H.; Caro, J. Effect of the B-Site Composition on the Oxygen Permeability and the CO_2 Stability of $\text{Pr}_{0.6}\text{Sr}_{0.4}\text{Co}_x\text{Fe}_{1-x}\text{O}_{3-\delta}$ ($0.0 \leq x \leq 1.0$) Membranes. *Chem. Mater.* **2015**, *27*, 2911-2919.
3. Liang, F. Y.;* Luo, H. X.; Partovi, K.; Ravkina, O.; Cao, Z. W.; Liu, Y.; Caro, J. A Novel CO_2 -Stable Dual Phase Membrane with High Oxygen Permeability. *Chem. Commun.* **2014**, *50*, 2451-2454.
4. Partovi, K.;* Bittner, M.; Caro, J. Novel CO_2 -Tolerant Al-Containing Membranes for High-Temperature Oxygen Separation. *J. Mater. Chem.* **2015**, *3*, 24008-24015.
5. Partovi, K.;* Rüscher, C. H.; Steinbach, F.; Caro, J. Enhanced Oxygen Permeability of Novel Cu-Containing CO_2 -Tolerant Dual-Phase Membranes. *J. Membr. Sci.* (in revision).

Publication Not Included in the Thesis

Liang, F. Y.; Partovi, K.; Jiang, H. Q.; Luo, H. X.; Caro, J. B-Site La-Doped $\text{BaFe}_{0.95-x}\text{La}_x\text{Zr}_{0.05}\text{O}_{3-\delta}$ Perovskite-Type Membranes for Oxygen Separation. *J. Membr. Sci.* **2013**, *1*, 746-751.

Curriculum Vitae



Personal Data:

Name: Kaveh Partovi Amarloei

Date of birth: 02.11.1981

Place of birth: Tehran, Iran

Nationality: Iranian

Marital status: single

Higher Education:

Since 03.2012 Scientific research staff at the group of Prof. Dr. Jürgen Caro,
Institute of Physical Chemistry and Electrochemistry,
Leibniz Universität Hannover, Germany

09.2009-01.2012 M.Sc. Material and Nanochemistry
Master thesis at the group of Prof. Dr. Jürgen Caro
Title of the Thesis:
*“Development of Lanthanum-Doped
(Ba_{1-x}La_x)(Fe_{0.95-y}La_yZr_{0.05})O_{3-δ} Perovskite-Type Membranes
for Oxygen Separation and Dehydroaromatization of Methane”*
at Leibniz Universität Hannover, Germany

2002-2008 B.Sc. Applied Chemistry at K.N.Toosi University of
Technology, Tehran, Iran

Erklärung zu dieser Dissertation

Hiermit erkläre ich, dass ich die vorliegende Dissertation selbständig verfasst und die benutzten Hilfsmittel und Quellen sowie die zu Hilfeleistungen herangezogene Institutionen vollständig angegeben habe. Die Dissertation wurde nicht schon als Masterarbeit, Diplomarbeit oder andere Prüfungsarbeit verwendet.

Hannover, den 27.04.2015

Kaveh Partovi Amarloei, M.Sc.